in vivo Analysis of Plant Mechanics Using Atomic Force Microscopy and Modelling

Ross Carter

A thesis submitted for the degree of Doctor of Philosophy

Department of Animal and Plant Sciences
University of Sheffield

November 2015

Contents

List of Figures

Acknowledgements

First and foremost I would like to thank my supervisors, Andrew Fleming and Jamie Hobbs. Without their continued guidance and endless patience this work would not have been possible. I would also like to thank Nick Monk who, despite not being my official supervisor, offered valued support with the modelling side of the project.

I would like to acknowledge the hard work of my collaborators in this work. Hoe Han Goh was of great help during the early stages of this work, guiding the experiments on the hypocotyl, Ania Kasprewska offered her AUX/LAX gene expression data to help with the conception of the auxin transport model and Sam Amsbury helped with growing plants and collecting the stomata data.

Thanks to my friends and colleagues in Physics and APS: Rik, Jake, Ana, Amy, Nusrat, Nic, Becca, Paul, Stephen, Tom, Chloe, Jen, Christoph, Bobby, Julia, Jamie, Amin and anyone else I've missed.

I gratefully acknowledge the funding provided by the BBSRC case studentship in collaboration with Advanced Technologies Cambridge.

Finally I would like to dedicate this thesis to my parents and sister who have supported me unwaveringly throughout my studies.

Abstract

Morphogenesis in plants occurs as a combined outcome of hormone pattern formation and mechanical changes involving cell growth and division. In this work a method was developed for measuring mechanical properties of plant cells at sub-cellular resolution using the atomic force microscope.

Initial work focussed on the measurement of the mechanical properties of a number of wild type and transgenic *Arabidopsis* hypocotyls. Mutants in expansin expression were measured and were hypothesised to have cell walls of reduced stiffness. Due to the variation in results, or the wrong hypothesis, trends that fitted with the hypotheses were not seen. A series of experiments were performed to investigate this variance and standardise future measurements. An investigation into the effect of angle of indentation and depth of indentation were carried out.

Following on from this work focussed on the stomata. A series of experiments were carried out to quantify the mechanical properties of these cells, comparing them to the properties of the cells surrounding them. Multivariate correlation analysis was performed to test hypotheses that these measurements correlated with other geometrical parameters, such as how open the stomate is and how large it is and significant correlations between these were found.

A model of auxin pattern formation in the leaf margin was developed that incorporated knowledge of a family of auxin importers thought to have an important role in morphogenesis. These results show that auxin importers may have a role in stabilis-

ing the patterning of hormones and influence the timing and positioning of hormone peaks. This model highlighted the fact that the idea of a cell's sensitivity to auxin is important and may have an affect when considering how auxin effects the growth of cells.

Chapter 1

General Introduction

1.1 Introduction

Growth is an intrinsic part of any biological organism, be it plant, animal, or bacteria. Although there is a large amount of genetic and biochemical data related to plant growth, the actual process is a mechanical one based on the laws of classical physics and it remains a major challenge to relate these genetic and biochemical processes to that of mechanical growth. Our understanding of the physical processes underpinning growth in biological systems remains remarkably limited. Plants offer an excellent system to study these processes for a number of reasons. Plant growth and development is largely a process of cell growth and division in which neighbouring cells remain fixed together. This is in contrast to many aspects of animal development where cell migration adds a layer of complexity to understanding the mechanics of growth. In addition, plant cells are characterised by a semi-rigid encasing cell wall which can be easily visualised and which form geometric patterns. This raises the possibility of modelling these patterns and inferring stress/strain relationships using mathematical approaches.

A large amount of data is held on both the chemical and physical properties of plant cells. However experiments on physical properties have largely focused on bulk samples

that have been heavily processed and relating the properties of this processed tissue to that of living cells *in vivo* remains problematic.

In recent years advances in metrology in the physical sciences have led to novel methods being used to probe the structure of living biological material. The atomic force microscope (AFM) has evolved from a high resolution imaging tool into an instrument that can measure mechanical properties to sub-micron resolution. Characterisation of the mechanical properties of plants at the sub-cellular level remains key to understanding the dynamic processes that underpin plant growth. Accompanying this there has been a resurgence in the application of theoretical modelling techniques to biological systems and their use in informing and testing experimental approaches.

In this chapter I will give a brief overview of the mechanical and structural processes involved in plant growth, the history of AFM and its use in biology, and past and current approaches to modelling both plant growth and molecular dynamics. I will then go on to give an outline of the research carried out and the aims and objectives of this thesis.

1.2 The Mechanics of Plant Growth

Plant cells are eukaryotic cells which differ from animal cells in that they have a cell wall and a vacuole. The vacuole is a membrane bound organelle which contains water and other organic and inorganic compounds [1].

Plant cells grow in size through the combined effect of increased water uptake and cell wall loosening [2]. This water uptake is achieved by the transport of active ions into the vacuole which leads, via osmosis, to a flow of water into the cell. Therefore physical cell growth is essentially a mechanical process in which an internal, turgor, pressure is contained by a surrounding wall under tension [3]. Cell wall mechanical properties will thus have a large effect on how cells grow, both in terms of rate of growth and,

via the potential for anisotropy in the cell wall, the preferred orientation of growth. The main difference between plant cells and the cells of animal, fungi and bacteria is the composition or presence of the cell wall and the different composition/properties of these walls greatly influences the biology of the systems. Animal cells contain no cell wall but, in multi-cellular organisms, have an extracellular matrix within which the cells are embedded. Bacteria have a cell wall made of peptidoglycan and fungi have a cell wall made of chitin [4].

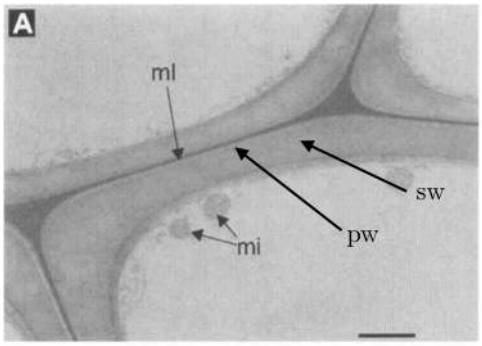

Figure 1.1: Electron micrograph of a cross section of *Arabidopsis* cells showing the different layers that make up the cell wall. ml, middle lamella. pw, primary wall. sw, secondary wall. mi, mitochondria. Scale bar = 1.5 μm (taken from [5]).

The plant cell wall is a composite structure made of up to three layers (Fig. 1.1). The middle lamella is primarily made up of pectin, a structural polysaccharide, and is located between adjacent cells and acts to bind them together. The primary cell wall forms as plant cells are growing and contains, among other carbohydrates, cellulose, hemicellulose and pectin (Fig. 1.2). Cellulose microfibrils form the major structural component of the primary cell wall and are cross-linked with hemicellulose to form a network which is embedded within a pectin matrix [6]. When the cell has finished growing the secondary cell wall is formed. The secondary cell wall has additional components that act to alter the mechanical properties such as lignin, a complex polymer, which fills the spaces in the wall between the previously mentioned components. Lignin gives plant cell walls additional mechanical strength. Due to the anisotropy imposed by the cellulose microfibrils, a single measure of mechanical property for cell walls is not sufficient for description of the mechanics [7]. Epidermal cells also have a

layer of cuticular wax on their outer surface to reduce water loss and offer protection from other environmental stresses [8].

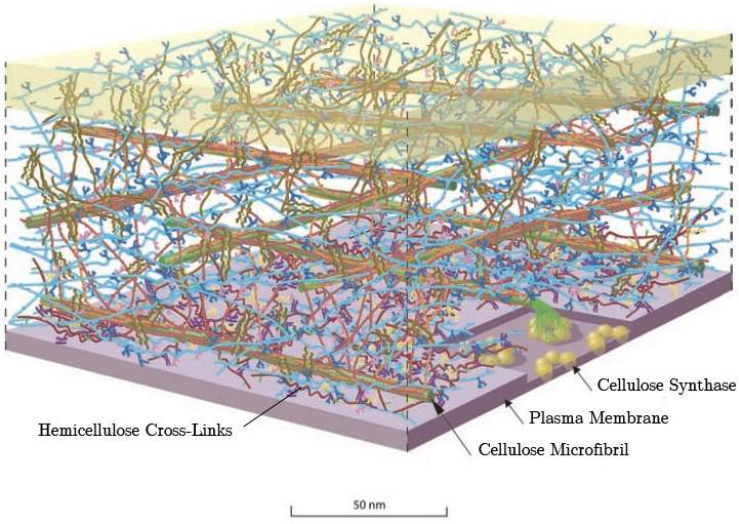

Figure 1.2: A scale schematic of the primary plant cell wall showing the various polymers that make up the wall. Cellulose microfibrils are linked together by hemicellulose cross-links, these cross-links are hydrogen bonded to the microfibrils. Not shown is the pectin matrix in which the cellulose-hemicellulose network is embedded. (taken from [6]).

Turgor pressure is caused by the osmotic flow of water from outside of the cell into the vacuole [3]. This pressure acts to push the plasma membrane against the cell wall. Osmosis causes a flow of water between areas separated by a membrane from areas with low solute concentration to areas of high concentration. Plant cells are surrounded by a lipid bilayer membrane which allows water to pass but limits the passage of solutes. This turgor pressure keeps the cell wall under tension and is responsible for the rigidity of plant cells. Depending on the concentration of solute in the water surrounding the plant cell it may be in one of three states. In a hypertonic solution the water in the cell passes through the membrane and out of the cell in a process known as plasmolysis. In an isotonic solution no osmotic gradient is maintained and the cell is remains flaccid. In a hypotonic solution, water passes into the cell and the cell is turgid and the walls are plasticly deformed as viscoelastic creep occurs, contributing to cell growth. For a plant to remain healthy, all cells should be turgid. As turgor is non-directional, further control is required to generate non-spherical cell shapes, such as containment in an extra-cellular matrix such as the cellulose microfibril network [9]. Changes in turgor

pressure are responsible for dynamic processes in plants [10] including the opening and closing of stomata (pores on the leaf surface), the rapid closing of the venus flytrap, and the movement of sunflower flower buds to track the sun in a process known as heliotropism [11].

Equations to describe the growth of plant cells were developed by Lockhart [12]. He combined the two processes known to occur in plant growth (the extension of the cell wall, and the influx of water to occupy the extra volume) into a single equation describing the longitudinal (i.e. one dimensional) growth of a cylindrical cell;

$$\frac{1}{l}\frac{dl}{dt} = \begin{cases} \dfrac{2K_w r\phi}{2K_w + r^2\phi}(\Delta\Pi - P_E) & \text{if } P > P_E \\ 0 & \text{if } P < P_E \end{cases}$$

Where $\frac{1}{l}\frac{dl}{dt}$ is the proportional rate of length increase, ϕ is the wall extensibility, a measure of how deformable the wall material is, K_w is the water permeability of the cell membrane, r is the radius of the cylindrical cell, P_E is a threshold pressure, above which irreversible expansion of the cell wall occurs. $\Delta\Pi$ is the difference between the osmotic pressures within the cell and of the solution in which the cell is immersed. By isolating plant tissue from an external water supply and measuring the corresponding decrease in turgor pressure over time it is possible to estimate the threshold pressure and wall extensibility using this equation [13].

At a chemical level, growth in plants is controlled by signalling hormones. A major group of growth hormones related to many, and possibly even all areas of plant growth and development are auxins. Auxins have many different effects such as inducing cell elongation and division and, on a larger scale, act as a signalling molecule necessary for the initiation of organ development and coordination of growth [14].

Mechanical forces have been shown to act as transducing signals in plant development and morphogenesis [7]. Plant cells are thought to constantly rebuild their cell walls to provide strength in the direction of greatest tensile force [15]. Cortical microtubules

(CMTs) on the inside of the cell control the direction of cellulose microfibril orientation and thus the anisotropy of cellulose within the cell wall [16]. By imaging the dynamics of the CMTs one can indirectly get an idea of the rebuilding occurring in the cell walls. This anisotropy of cellulose in the cell walls is vital in directing growth during morphogenesis of cells and organs. It has been shown that if the microfibril development and orientation in the cell wall is disrupted using the inhibitor oryzalin, the cells form into a 'froth' similar to that of soap bubbles, inducing growth at the organ level to form spherical structures [17].

This modulation of cell wall properties is the key mechanism of controlling when and where growth occurs. For example the cell wall loosening protein expansin [18] is thought to work by loosening the bonds between hemicellulose and cellulose microfibrils in the cell wall and causing wall stress relaxation and irreversible cell wall extension, leading to cell growth and enlargement.

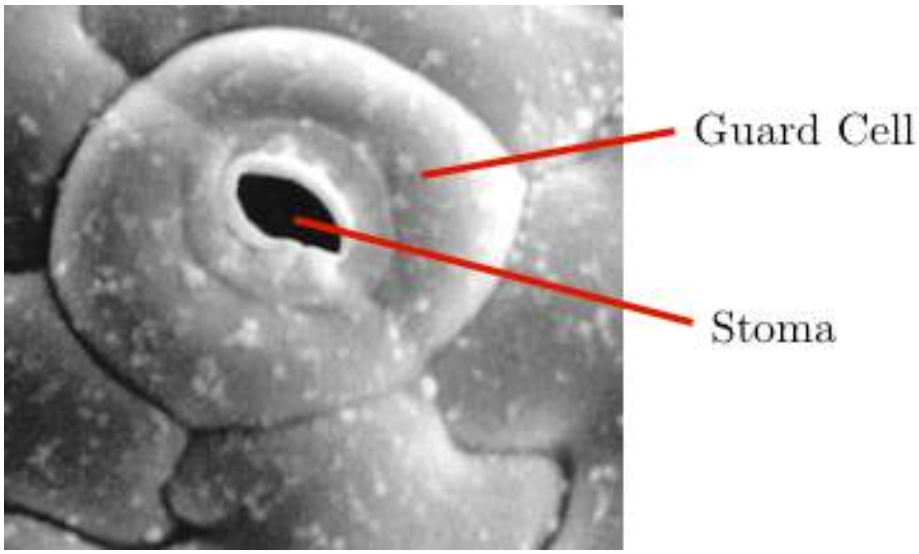

Figure 1.3: An electron micrograph of a stomate showing the two guard cells and the stoma, the pore through which gas and water are exchanged with the atmosphere (taken from [19])

One example of a dynamic mechanical process in plants is provided by stomata. Stomata (Fig. 1.3) are the pores formed by two specialised cells (the guard cells) on the surface of aerial organs of most higher plants. They open and close to regulate gas exchange and transpiration and are essential for photosynthesis as they allow carbon

dioxide into the plant and transpired water out [20]. The opening and closing mechanism is performed by the dynamic change of turgor pressure within the guard cells and how guard cells function must depend on the mechanical properties of these specific cells in the leaf, but surprisingly little is known about the structure/function of guard cell walls. The availability of tools to manipulate guard cell properties, in the form of genetic mutants and pharmacological chemicals makes them an ideal choice to investigate the manipulation and measurement of plant cell mechanics.

1.3 Methods of Measuring Cell Mechanics

There are many techniques for the measurement of physical parameters at the cellular and sub-cellular level. Some of the following techniques can be performed by an Atomic Force Microscope, which will be the main focus of this project. As the plant cell consists of a wall with an internal pressure, methods tend to focus on measuring either the wall properties or the turgor properties. The resolutions obtained can be split into either cellular, in which a property of the entire cell is measured, or sub cellular, by which properties can be measured locally over the cell [21].

Figure 1.4A Shows the basic working principles of the Atomic Force Microscope (AFM). The AFM can act as both a high resolution imaging tool and a force sensor, sensitive to pico-newton forces. The working principles and applications of AFM are described in section 1.4. Similar to AFM, Fig. 1.4 D shows the measurement of local properties using a micro indentation apparatus. A glass stylus is connected to a beam with measured bending stiffness and the sample resistance to deformation can be measured. The deflection of the stylus is measured by the reflection of a laser beam from the top of the stylus. Due to the length of the stylus, the supporting beam is out of focus of the imaging optics and the sample can be viewed clearly from the top. This allows the deformation to be observed visually and cellular dynamics can be viewed directly. This technique has been used successfully on pollen tubes [22]. As cells in the pollen

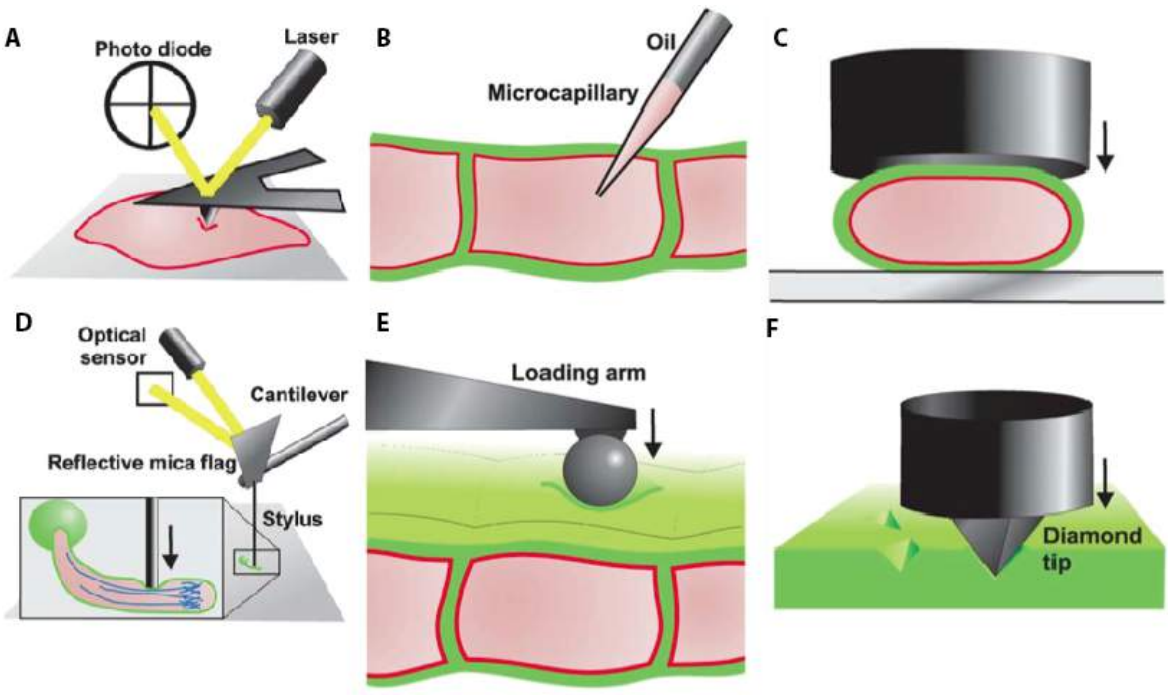

Figure 1.4: Various methods of measuring plant cell mechanics. (**A**) Atomic Force Microscopy. (**B**) Pressure Probe. (**C**) Single Cell Compression. (**D**) Micro Indentation. (**E**) Ball Tonometer. (**F**) Nano-Indentation. (taken from [21])

tube grow quickly, the position of the stylus with respect to the sample changes and this can be monitored optically. A method of determining the bulk stiffness of a cell is by the single cell compression method (Fig. 1.4C). A single cell is compressed between two plates and the mechanical and turgor properties of the whole cell can be calculated by monitoring the cell's reaction using a theoretical model of contact mechanics [23, 24]. A method currently garnering favour, which can be carried out with the AFM, is nano-indentation(Figure 1.4F). In this approach a tip is used to locally indent the surface of the sample. By measuring the force applied and the indentation depth the physical properties of the sample can be calculated. This method is useful as it allows for the characterisation of surface properties with high resolution giving a picture of variation across the surface of a sample.

Viscoelastic properties of the cell wall can be measured in bulk by devices such as a rheometer [25], which reports properties of materials which cannot be described by one measure of viscosity, such as the plant cell wall. A rheometer reports results in the form of a so called relaxation spectrum, a graph of how a material responds to

applied loads at different frequencies of loading. This allows rapid and long term material response to be measured and quantified. This approach was used to measure visco-elastic mechanical phenotypes of transgenic potatoes that differ in hemi-cellulose structure [26]. It must be noted, however, that the cell wall can actively respond to stresses and strains it detects [27], and remodel itself accordingly, so this must be taken into account when interpreting results.

As mentioned in section 1.2, mechanical properties of plant cells are anisotropic, i.e. they have some directionality to them. The anisotropy in plant cell walls comes around due to the arrangement and directionality of the cell wall components, such as the cellulose microfibrils. *in vivo* measurements of anisotropy have been performed on bulk inorganic materials, such as metals [28]. In these experiments, an non-axisymmetric indenter is used at differing angles between the indenter and the crystal structure. Measurements on biological tissue are trickier to characterise due to the inherent disordered nature of the constituent materials when compared to the crystal structure of metals. One method of measuring the anisotropic material properties of plant tissue is by multi-axial tensile stress experiments [29], where the response to loads applied under different sample orientations is compared. Anisotropy in the measurement of mechanical properties will not be considered in the experiments described in this research as the AFM results provide no such data.

Turgor pressure has been measured by various indirect techniques. One such method is Incipient Plasmolysis, where the osmotic potential of a surrounding medium is varied until the cell is neither flaccid nor turgid and the internal and external potentials are balanced. This measure of potential can then be used to inform an estimate of the turgor [30]. The ball tonometer (Fig. 1.4E) uses the cell's ability to bear a spherical load and relates the load induced deformation of the cell to the internal turgor pressure [31]. This method is only really useful for cells with a thin wall and can only be used on surface cells. Pressure is quantified by calibrating the contact area between the spherical probe and the underlying cell and is normally assessed

optically.

One direct method of measuring turgor pressure is by using a pressure probe (Fig. 1.4B) (reviewed in [32]). This method was initially used to measure the turgor pressure in algal cells [33]. In early experiments a microcapiliary was filled with a liquid (usually water or oil) and an air bubble was trapped near the top. By piercing the cell, liquid traveled up the microcapiliary and compressed the air bubble. By using Boyle's law the pressure was determined. This air bubble technique is no longer used. Modern pressure probe techniques use electronic pressure transducers, first used in the late seventies [34]. Electronic pressure transducers work by measuring the force applied by the gas or liquid over a certain area. Measurement of the force is usually performed by measuring the deformation of a capacitative or piezoelectric diaphragm. By using the pressure probe it is possible to observe both plastic and elastic deformations during cell enlargement [35]. They added and removed cell solution to internode cells of *Chara* and tracked the changes in cell length. By performing the experiments at low temperatures, where growth stopped and deformation was elastic, and at normal temperatures where both elastic deformation and plastic growth occurred, they were able to separate the effects and observe purely plastic growth. By varying turgor they noticed rapid changes in cell growth rates. They concluded that growth rate was not controlled purely by polymer extension but involved biochemical reactions that are caused by changes in turgor.

The AFM can perform many of these methods (Fig. 1.4 C,D,E,F) as well as acting as an imaging device. This versatility makes it the instrument of choice for unlocking the mechanical properties of plant cells.

1.4 The Application of Atomic Force Microscopy (AFM) Techniques in Biology

The AFM was invented in 1986 by G. Binnig and C. F. Quate [36]. It belongs to a family of microscopes know as 'Scanning Probe Microscopes' (SPM). These microscopes differ in function but all work on the same principle. A probe is scanned across a sample and some kind of interaction between the probe and the sample is measured. An SPM overcomes the diffraction limit of optical microscopes to allow imaging of a much higher resolution. The AFM was born out of the need for an SPM device that could be used to measure forces and topography on non-conducting samples.

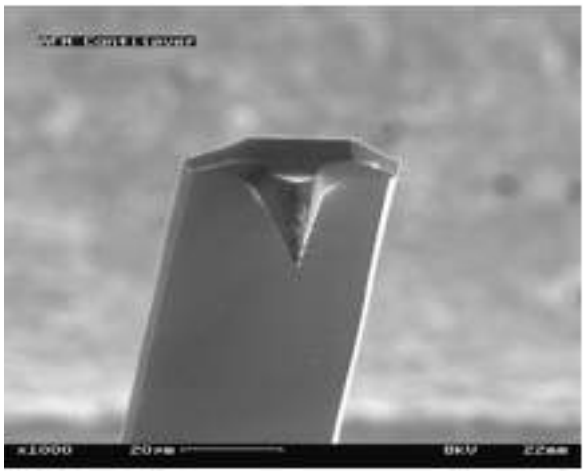

Figure 1.5: An AFM probe. The sharp tip is located on the end of a cantilever. The cantilever is around 40 μm wide and the tip has a nominal radius of 2 nm

An AFM uses a small probe with a sharp tip, usually made from silicon, to probe the interactions with the surface (see Fig. 1.5). Depending on the construction of the AFM, either the sample is scanned relative to the tip or the tip is scanned relative to the sample. This movement, in most situations, is achieved by piezo-electric actuators [37]. As the tip interacts with the surface, the interactions are measured and used to build up a picture of the topography (Fig. 1.6). These interactions include van-der-vaals forces, electrostatic repulsion and capillary forces. The interactions are altered by moving the tip, or the sample, in the z direction by way of a piezo-electric actuator. To measure the deflection of the cantilever most AFMs use a focused laser spot reflected

off the rear of the cantilever and onto a split photodiode. The voltage output from the photodiode can then be used to calculate the deflection of the cantilever once the photodiode has been calibrated.

There are many modes of operation for imaging using AFM, which vary in the driving of the cantilever and the method of the feedback. I will describe two of the most widely used. Contact mode is a static imaging mode [38] in that the cantilever is not driven in any way. The tip is dragged across the sample and the deflection coming from the interaction with the sample surface is used as the feedback signal. As the tip is prone to noise and drift a low stiffness cantilever is used to increase the deflection signal. The force between the tip and the sample is kept constant by maintaining a constant deflection of the cantilever. The piezo movement required to keep the deflection constant is used to build up a height image of the sample.

Intermittent-contact or Tapping mode is a dynamic mode of operation [39]. A cantilever is oscillated near it's resonant frequency and is positioned so, during a small portion of its motion, it is in contact with the sample. The amplitude of the oscillation is used as a feedback signal and changes depending on the height of the sample. The piezo movement required to return the oscillation frequency to its set point is used to build up a height image of the sample. This mode of operation has an added bonus of being able to detect the phase difference between the drive and detected signals. From this phase signal it is possible to infer adhesive, and viscoelastic properties [40]. Larger phase differences result from energy being transferred from the resonating tip to the sample, and more viscous samples will increase this phase difference.

When imaging in air, the meniscus force may dominate the force interaction between the sample and the cantilever [41]. To negate this force it is possible to image under liquids. Imaging under liquids is also preferable when using a biological sample, as conditions as close as possible to *in vivo* conditions will give the most useful results.

Another use of the AFM is for performing force-spectroscopy measurements. An AFM

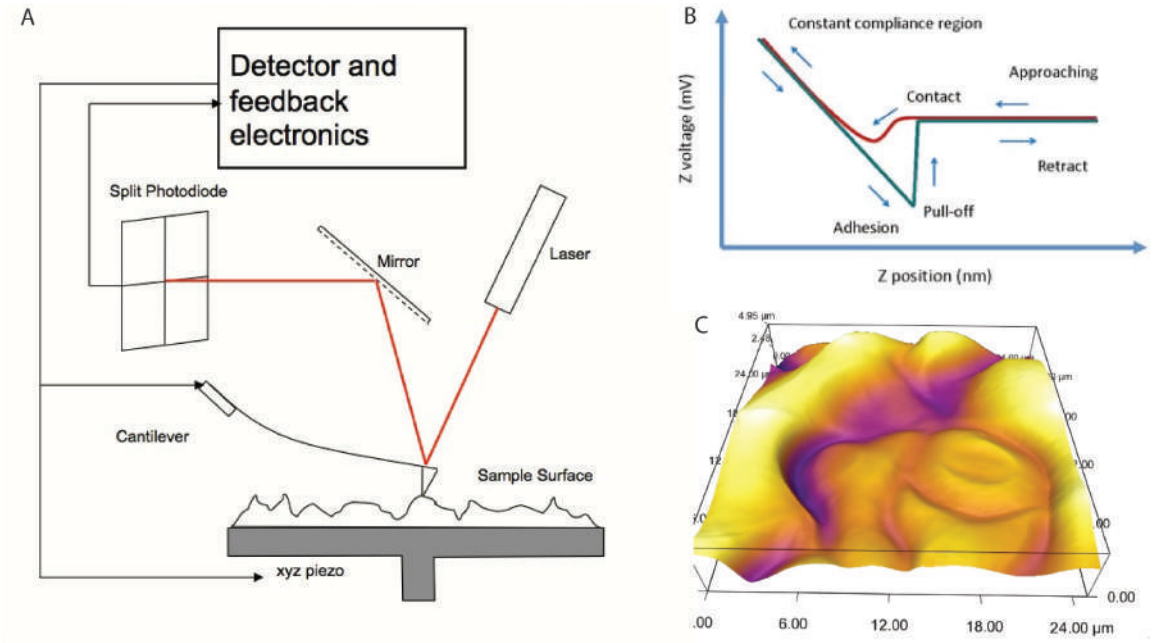

Figure 1.6: (**A**) Simplified AFM setup. The cantilever tracks the sample surface and deflects when it touches the surface. A laser reflected off the back of the cantilever monitors the deflection of the cantilever by way of a split photodiode onto which the laser is reflected. The voltages returned to the detector and feedback electronics are recorded and used in the feedback methods to move the cantilever and track the surface accurately. (**B**) Force curve. (**C**) AFM height image of the surface of the abaxial side of an *Arabidopsis* leaf showing a stomata and surrounding epidermal cells.

cantilever can be considered as a spring that obeys Hooke's Law, that is it's displacement is directly proportional to the force applied to the tip through the spring constant. The spring constant can be measured in a number of ways, the most popular being the 'Thermal Method' [42]. The cantilever is allowed to fluctuate in response to thermal noise. Treating the cantilever as a simple harmonic oscillator allows us to estimate the value of the resonant frequency, and in turn, the spring constant. The Hamiltonian for a simple harmonic oscillator is:

$$H = \frac{p^2}{2m} + \frac{1}{2}m\omega_0^2 q^2 \tag{1.4.1}$$

Where p is the momentum of the oscillator, m is the mass of the oscillator, ω_0 is the angular frequency of oscillations and q is the displacement from equilibrium of the oscillator. By the equipartition theorem [43] the average of each of the quadratic terms in the hamiltonian is equal to $1/2\ k_B T$ and therefore the harmonic term is:

$$< \frac{1}{2} m\omega_0^2 q^2 >= \frac{1}{2} k_B T \tag{1.4.2}$$

Where k_B is Boltzmanns constant and T is the temperature. For simple harmonic motion of a spring $\omega_0^2 = k/m$, which gives a direct relation between the spring constant and the average of the square of the displacements i.e.,

$$k = \frac{k_b T}{< q^2 >} \tag{1.4.3}$$

If fluctuations and displacements are measured in the time domain at a sampling frequency higher than the resonant frequency of the cantilever (to avoid averaging out the fluctuations) an estimation of the spring constant can be found. To look at the contributions to displacement that are only due to thermal fluctuations we look at the data in the frequency domain by performing a 'Fast Fourier Transform'. This data takes the form of 'power spectral density' and has a Lorentzian line shape (Figure 1.7). Since the area under a power spectrum is equal to the mean square of the fluctuations in the time-data series [44], $< q^2 >= P$, the estimate of the spring constant becomes $k = \frac{k_b T}{P}$.

For force spectroscopy measurements the tip is moved perpendicular to the surface until it comes into contact and indents the sample. Due to the fact that the main method of deflection detection is the use of a laser spot reflected off the back of the cantilever, the photodiode's response to deflection needs to be calibrated every time the laser spot is moved. This is performed by acquiring a graph of vertical displacement against deflection on an incompressible sample (glass, mica, etc.) and assuming a 1 to 1 relationship between vertical displacement and deflection of the cantilever. Due to hydration forces between the tip and sample it may be beneficial to perform measurements under liquid. This essentially negates the attractive meniscus force. The deflection signal can then be used to form a displacement vs. deflection curve,

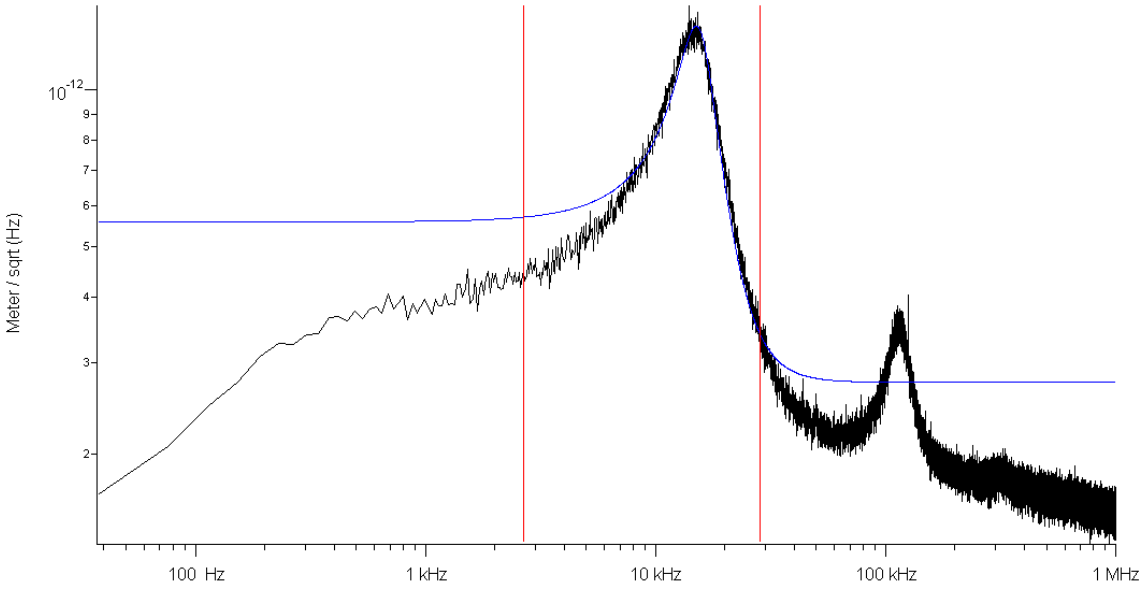

Figure 1.7: A plot of the thermal fluctuations of a cantilever. The first peak corresponds to the first resonant frequency, here around 15 kHz

a graph of vertical displacement of the piezo controlling the height of the cantilever against the deflection of the tip contacting the sample (Fig. 1.8). By multiplying the deflection of the cantilever by its spring constant the indenting force can be acquired. Acquiring a number of force curves over the surface of a sample in a grid pattern, in a process known as 'Force Mapping', gives a picture of variation of these properties over the surface of the sample.

By analysing the contact portion of the force curve, many properties of the sample can be determined such as stiffness, elasticity, and adhesion [45]. The term 'stiffness' is essentially the effective spring constant of the sample, the force required to displace or indent a sample by a certain distance (measured in Nm^{-1}) and is obtained by the gradient of the contact section of the force curve. This measure is extrinsic, i.e. it depends on the measurement parameters, such as the indenter geometry. To attain intrinsic properties of the sample, such as Young's modulus, models of indentation need to be used, the most popular being the Hertz model. The Hertz model describes the simple case of elastic deformation of two homogenous smooth bodies touching under load [46]. Two important assumptions from the Hertz model are that the indenter

must have parabolic shape and that the sample is assumed to be extremely thick when compared to the indentation depth [47]. When selecting a model of indentation, one needs to be aware of the limitations and be sure the assumptions are valid for the experiment.

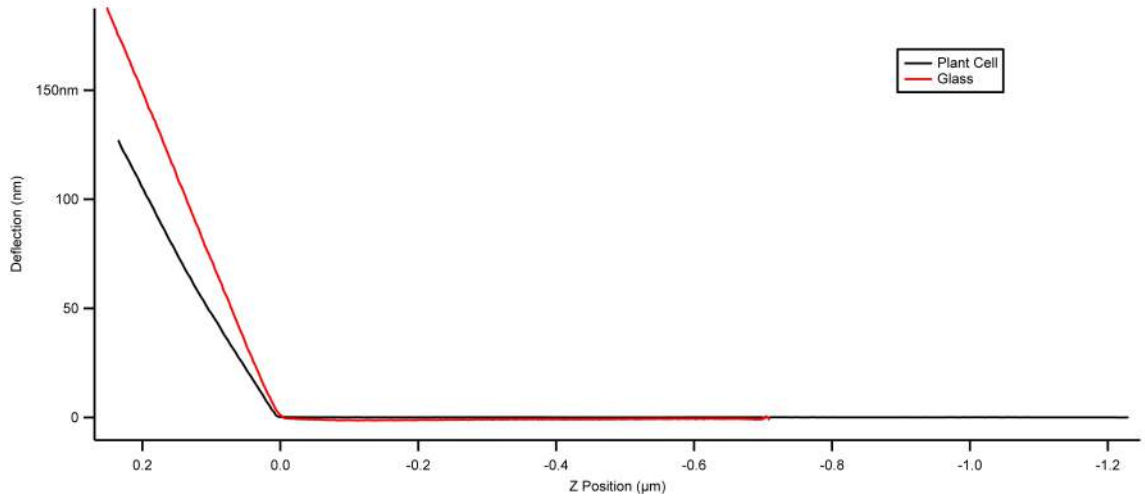

Figure 1.8: Deflection vs. Z Position curves for glass and plant cell wall. The differences in gradient of the two curves relates to the differences in indentation of the sample. The ratio of the gradients of the two curves, along with the stiffness of the cantilever, can be used to calculate the effective spring constant of the sample (Equation 2.3.2).

AFM use in biology has been garnering favour since the mid 90's where surfaces of hard samples were routinely imaged to atomic resolution. Soft samples, however, remain challenging for a number of reasons. The first soft samples to be imaged were crystals of amino acids and crystalline polymers [48]. DNA was imaged in 1992 [49] and around that time imaging of live cells became possible [50], but measurements were not trivial due to the softness, mobility and motility of the samples.

Plant AFM grew to popularity around the mid nineties [51]. One of the first papers published looked at the cell wall properties of water chestnut, apple, and carrot cells [52]. The tissue of these plants had been heavily processed by means of ball milling which ruptures cells and leaves the cell contents to be washed away. The cell wall fragments were not fixed to the surface and imaging was performed in air which, due to the moistness of the sample led to the cantilever being pulled to the surface and problems with laser deflection. As the cell wall fragments are polysaccharide networks,

they hold water and as they dried out the sample became rougher which limited the imaging time to around 1h. At later time points images cannot be obtained due to the roughness of the dried film. Images show aligned fibrous structure which are assumed to be cellulose microfibrils. They were also able to see laminated structure in freeze-thawed samples with different layers showing different microfibril orientation. They give a measure of microfibril thickness of around 2.5nm, which agreed with estimations from earlier electron microscopy analysis [53].

Analysis of samples that have been heavily processed can give useful information about dimensions and properties of structural constituents, but to obtain the properties of living plants, measurements need to be performed *in vivo*. Recent work on measuring mechanical properties *in vivo* has been performed on the shoot apical meristem of *Arabidopsis* [54]. AFM force measurements were carried out on the cells that make up the shoot apical meristem and these cells were also imaged in Tapping Mode. The authors concluded that there is a complex spatialization of mechanical properties in the meristem at subcellular, cellular, and supracellular scales. Using previous work that characterised the growth rates of cells in the meristem [55] they correlated growth rates with differing mechanical properties, showing that fast growing cells were generally less stiff than slowly growing cells. This agrees with the generally accepted model that plant cells loosen their walls and increase the volume of water within the cell, to grow. Although these experiments were performed *in vivo*, the meristems were still excised from the plant. Fluorescence experiments showed the cells were still functioning, but it is questionable whether or not they were functioning as they would be were they connected to the rest of the plant. This is one of the main limitations of using the AFM in biology. There needs to be a tradeoff between having access to the part of the sample being measured and the realism of the results obtained. Nevertheless this experiment brought to light some interesting results and showed that the AFM can be used in the examination of living plant tissue.

More recently, research carried out by Braybrook *et al* [56, 57] looked at how the me-

chanical properties of the shoot apical meristem (SAM) in *Arabidopsis* change during organogenesis. They used atomic force microscopy to measure the cell wall rigidity of the SAM prior to organ initiation and noticed a decrease in measured values. They correlated this change to a build up of auxin in the same area and showed using various mutants that this change in stiffness is due to the auxin causing local de-methyl-esterification and breaking of the hemi-cellulose cross-links between cellulose fibrils. This de-methyl-esterification causes cell wall softening and tissue outgrowth, leading to functional organ formation.

1.5 Modelling Approaches in Plant Development

Computer modelling is an invaluable tool in scientific research, particularly in the area of imaging and interpreting the change of biological form. The fact that computer models can be used heuristically to inform experimentation means that the area of 'Computational Morphodynamics' has become a powerful methodology within plant biology. The main aim in this area of research is to integrate spatial, mechanical, and molecular aspects of morphogenesis with multicellular computational models in an iterative fashion [58]. Depending on how the researcher wishes to use the results of modelling and what experimental data the researcher incorporates, the level of complexity of these computational models can vary drastically.

There are three main types of model used in plant research: chemical, geometrical, and mechanical [59]. The level of model used has a direct influence on the question that the model can address. As it is impossible to model all the processes a plant undergoes, a choice needs to be made as to which processes will be modelled. A non-exhaustive list of model approaches, increasing in complexity, follows.

Plants, or parts of plants, can be modelled as continuous mechanical entities. There are numerous models that describe plants as entities that act in response to mechanical stresses and strains which in turn act on biological mechanisms. Experiments on the

action of auxins and expansins prove the existence of mechanotransduction mechanisms and the plants ability to respond to external stresses and strains [60]. This mechanical description of plant tissue has given insight into the geometry and formation of plant organs, including the phylotactic patterns that emerge in apical structures [61].

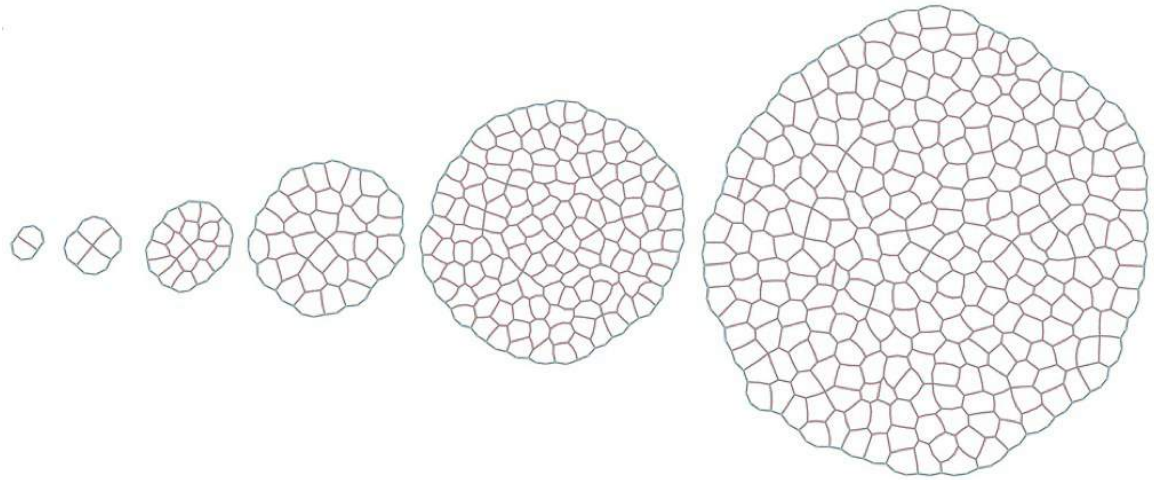

Figure 1.9: An example of a leaf simulated in VirtualLeaf [62]. Cells grow at a constant rate and divide when the reach twice their original size.

A plant also can be considered as a structure formed by the iterative addition of repeating structures. L-Systems generate plant structure using iterative rules for different parts of the plant [63]. This representation is able to reproduce a wide array of natural looking plants but is not particularly realistic in its formalism. The coupling of this type of system to the action of gene regulatory networks can give a more realistic view of patterns of development [64].

A plant is, in essence, a collection of cells. Treating cells as discrete interacting building blocks can help us understand how patterns can be formed and maintained [65]. More than any of the other formalisms, cell based models are linked to computational methods as they, more often than not, require complex, object orientated simulations. Many models fall into this category but of special interest here are models of leaf development. Virtual Leaf [62] is an open source modelling framework based around rules of cell expansion and cell division. Basic leaves are grown by expressing rates and rules for cell expansion and division (Fig. 1.9). Through the arbitrary change of me-

chanical properties virtual leaves can be made to look like real leaves (Fig. 1.10). By incorporating measured mechanical properties from, for example, AFM experiments, we can see if the interplay between these properties alone is enough to drive formation of leaf shape during morphogenesis.

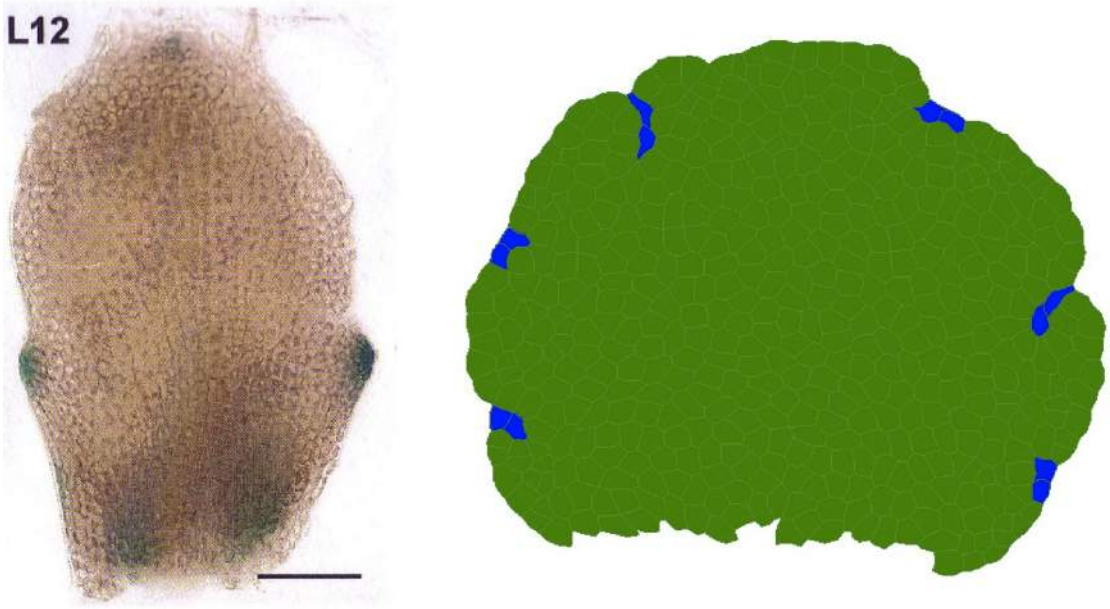

Figure 1.10: On the left is a real leaf showing areas of high auxin concentration in blue. Auxin is thought to have an effect on the mechanical properties of cells. On the right is a leaf simulated in VirtualLeaf. The cells coloured blue have altered mechanical properties which give it a more realistic shape compared to figure 1.9

Models of morphogenesis garnered favour with the work of Alan Turing [66]. His interest was in the area of fibonacci phylotaxis, the existence of fibonacci sequences in plant structures. He pioneered methods of using reaction diffusion equations in the area of pattern formation that are still used to this day. Models of this type are sometimes referred to as 'Turing Models'. Expanding models of this type to include effects such as active transport and production and decay of morphogens informed by experiment can lead to models that recreate patterns that closely resemble pattens formed by nature. The choice of morphogens for modelling of pattern formation in plants relates to those closely linked to organ development and initiation. Auxins are a group of hormones related to many areas of plant development and can be interpreted as morphogens. Auxin has many different effects on plants such as inducing cell elongation and division and at a larger scale, acting as a signalling molecule necessary

for the initiation of organ development and coordination of growth [14]. Models of auxin dynamics are therefore important to understanding the localisation of growth events. Modellers use the experimentally defined distribution of auxin reporters to inform the choice of mathematical algorithms used when designing models.

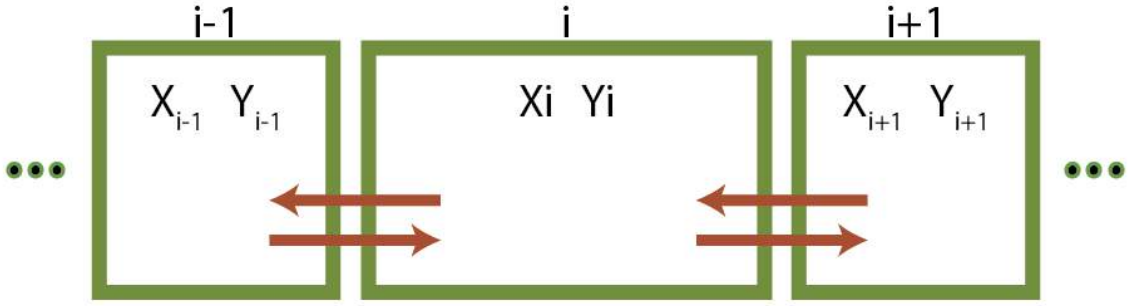

Figure 1.11: Cellular representation used in Turing type models. The current biological cell is i and cells surrounding are $i-1$ and $i+1$. X and Y are concentrations of the two morphogens and the arrows represent diffusion and transport between cells.

Cellular Turing models model concentrations of morphogens in discrete cells (Fig. 1.11). The concentration variations in time can be described by a series of differential equations, for example:

$$\left.\begin{aligned} \frac{dX_i}{dt} &= f(X_i, Y_i) + U(X_{i-1}, X_i, X_{i+1}) \\ \frac{dY_i}{dt} &= g(X_i, Y_i) + V(Y_{i-1}, Y_i, Y_{i+1}) \end{aligned}\right\} \qquad (i = 1, \ldots, N) \qquad (1.5.1)$$

Where X_i and Y_i are concentrations of morphogens X and Y in cell i, f and g are functions describing the local production and turnover of the morphogens, and U and V are functions describing the transport of morphogens between neighbouring cells by processes such as diffusion or active transport. For a system of N cells containing M morphogens there will be NxM differential equations. Using this formulation, and relating concentrations of morphogens to measurable phenotypes, such as colour or size, one can hope to gain an understanding of the processes that govern these effects.

Research carried out in 2008 [67] used a Turing model to investigate the effects that morphogen distribution has on root hair initiation. The authors modelled the genetic

regulatory network both within and between cells incorporating existing genetic and biochemical data to investigate the sufficiency of existing models of network interactions and how modelling assumptions can lead to phenotypes matching both wild type and mutant data. Results showed that for patterning to form around the root an interplay between two gene transcription regulators at the root epidermis was required. Their model proposes a mechanism based on lateral inhibition with feedback as opposed to the assumed model relying on local activation (Figure 1.12).

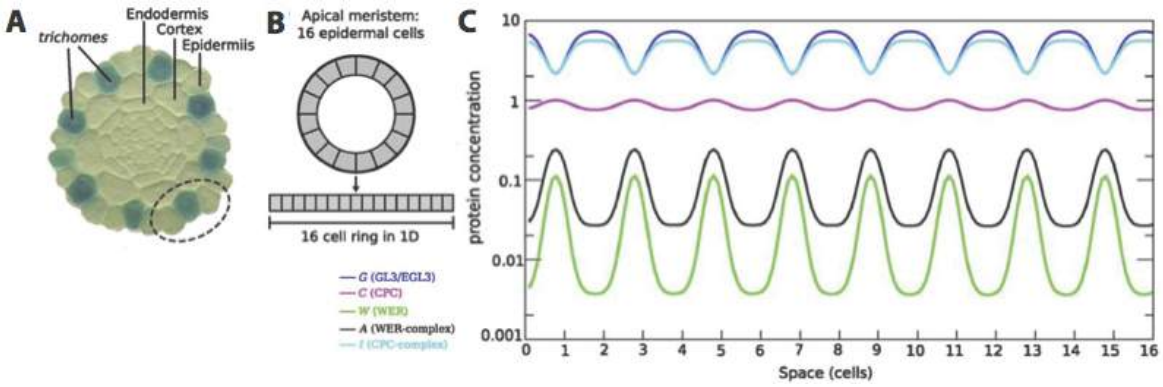

Figure 1.12: (**A**) A Cross section of an Arabidopsis root, The cells that are stained blue will become root hairs. (**B**) The model takes the epidermal ring of cells and straightens them into a line. The left and right hand cells are considered next to each other for the purposes of the model.(**C**) Protein concentrations at the end of the simulation. From a homogenous state, an alternating pattern of high and low concentrations emerges due to a Turing instability. [68]

Linking these protein concentrations to phenotypes, such as root hair position in this model, gives some indication of the underlying mechanisms involved in these processes, a direct link cannot be assumed as there may be many interlinking processes involved. Methods such as this are a good start and can lead to more informed experimental design, leading to more data which can be fed back into the model to improve or test it.

1.6 Research Outline

1.6.1 Aims and Objectives

The aims of this research were to develop and establish an AFM technique for the *in vivo* analysis of plant cell mechanical properties and to apply it to certain cell types and tissues to try and understand the relation between mechanics and growth. Alongside this experimental work a computational model would be developed to try and link hormone transport in the leaf and its relation to growth by incorporating gene expression data of certain hormone transporters.

1.6.2 Thesis Outline

This thesis begins with a general introduction, putting the research into context. I will then describe AFM experiments performed on the hypocotyl of *Arabidopsis thaliana* and issues that were encountered during this work. Following on from that I will describe AFM experiments performed on the stomata of *Arabidopsis* to try and gain a deeper understanding as to how the mechanical properties of these cells play a role in their function. Afterwards I will describe work carried out to develop and test a model of hormone transport in the leaf margin and how this relates to leaf shape formation.

Chapter 2

Establishing an AFM Technique for the *In Vivo* Analysis of Plant Tissue

2.1 Introduction

Morphogenesis in plants occurs through a carefully controlled combination of cell enlargement and cell division. For cells to enlarge there must be a change in the mechanical properties of the cell wall to allow expansion under the increase of water volume within the cell (see section 1.2). Acquiring an accurate measure of these cell wall mechanical properties will allow us to gain a deeper understanding of the physical processes involved in plant growth and morphogenesis.

Published experimental work regarding AFM measurements on *in vivo* plant tissue is fairly limited but does exist.

Research performed by Braybrook *et al* [56, 57] looked into the role the pectin matrix has during cell growth and organogenesis. Their work focused on the shoot apical meristem and looked into changes that occur in the pectin matrix during the forma-

tion and outgrowth of leaf primordia. They correlated a local reduction in measured values of wall stiffness (Youngs Modulus) on the meristem with areas where incipient primordia were expected to form. Average values for leaf primordia were also measured. The meristem modulus value averages to around 0.6 MPa, measured at the top of the dome. Areas where primordia were expected to form (predicted using phylotactic patterning) reported a reduced modulus, down to a value of around 0.3 MPa. Primordia were also shown to increase in stiffness as they matured into leaves, with Primordia 1 (P1 corresponding to the leaf just emerging from the meristem), having a stiffness nearly as high as the meristem by the time the leaf has undergone the 5th plastochron (the time the 5th leaf emerges from the apical meristem).

Through novel use of pectin and auxin mutants, Braybrook *et al* were able to put the variation in stiffnesses down to an accumulation of auxin and the local de-methyl-esterification of pectin in that area. As noted in an accompanying review article [69], this change in pectin chemistry appears to have a greater role in morphogenesis and organ initiation in the shoot apical meristem than generally assumed.

In research performed by Routier-Kierzkowska *et al* [70], researchers developed a machine they termed a cellular force microscope in-house to measure plant tissue mechanics. The working principles of this microscope are similar to the processes behind force mapping with an AFM but the probe they use, and with it the forces they apply to their samples, are much larger. Whereas research performed in this thesis used off the shelf AFM probes with a nominal tip radius of 2 nm, Routier-Kierzkowska *et al* used hemispherical indenters with a radius of 1 μm or 3 μm. The researchers investigated the mechanical properties of epidermal peels of onion and cultured BY2 tobacco cells in media. With the epidermal peels they were able to measure the apparent stiffness values (the gradient of the force-indentation curves at maximum indentation) of the cells in varying states of plasmolysis, before and after releasing turgor pressure by puncturing the cells. They also showed, using finite element models, that the indentation depths and indenter geometry they were using were small enough not to induce

changes in turgor pressure and to avoid irreversible changes to the cell wall.

Results reported in these two papers highlight one of the main problems with the interpretation of AFM force measurements, the comparability of measured material properties. Braybrook *et al* report their stiffness values as a Young's modulus. Young's modulus is an intrinsic material property which is a measure of how a material behaves under strain. In this case they use a Hertzian model of contact mechanics to extract their modulus values from force indentation curves. Depending on algorithms used to detect the contact point and the goodness of fit of models to their experimental data, these values can vary drastically. Compounded by the fact that other researchers use different models of contact mechanics to derive Young's modulus values and that these values are not comparable to other methods of measuring cell mechanics (See section 1.3), reporting such values can be misleading. Routier-Kierzkowska *et al* report their stiffness values simply as the gradients of their force-indentation curves. By reporting stiffness values in this way, they get over the fact that models of indentation mechanics involve lots of assumptions, but they essentially make their values of material properties extrinsic and incomparable to other researchers work. This problem of incompatibility between experiments is one that occurs again and again in research of this nature, and leads to complications in the work reported in this thesis.

In this chapter I will describe work undertaken to develop a method suitable for determining the local mechanical properties of plant tissue which has undergone as little preparation as possible, so as to get an understanding of the way these tissues behave *in vivo*.

Experiments were carried out on the hypocotyl of *Arabidopsis thaliana* due to the fact that this tissue is easily accessible and the cells that make up the tissue do not undergo division [71]. In addition, *Arabidopsis* has a wealth of genetic resources which enable the manipulation of the system. In this investigation we aimed to exploit an available transgenic line in which a cell wall protein, expansin, could be inducibly expressed. A body of evidence indicates that expansins influence cell wall extensibility, providing

a tool to manipulate cell wall mechanics [72, 73]. The ability to modulate cell wall extensibility would provide a basis for testing the validity of the AFM measurements derived from the experimental set up described in this chapter.

The hypocotyl is part of the germinating seedling. It's function is to push the developing shoot tip, including the shoot apical meristem and the cotyledons (primordial leaves), above the surface of the soil. The hypocotyl is formed within the seed of the plant and expands only through cell elongation and not cell division, thus decreasing potential complications in tissue analysis as we expect growth to occur primarily by the modulation of cell wall characteristics.

We aimed to characterise a mutant developed to be inducible in expansin over-expression and to see if expansin induction had an effect on the mechanical properties of the young hypocotyl.

We used four different *Arabidopsis* lines, wild type plants from the columbia background (col-0); two independent transgenic lines of a dexamethasone (dex) inducible expansin overexpressor (lines L9 and L10 containing the construct pOpON::CsEXPA1) [74] and an available line with dex inducible cyclinD3 over-expression as a control (CycD3) [75]. Cyclin D3 over-expression has been shown to promote cell division in plants, thus this line was used as a control to ensure that any effects observed with the inducible expansin transgenic lines were due to expansin expression and not simply due to their transgenic nature.

The expectation was that there would be no significant difference in measurements between the col0 (with and with out dex induction), the inducible expansin lines (L9, L10) or the CycD3 lines without dex induction. Induction with dex leads to expansin over expression in the L9 and L10 lines and this was expected to cause a reduction in measured stiffness compared to the wild type. The CycD3 line after induction with dex was also expected to show no significant difference when compared to the wild type plants.

During experimentation a number of questions arose, specifically problems with the morphology of the tissue, the effect of the depth of the indentation and the angle of indentation on the measured material properties. The depth of indentation may affect the results as the plant cell wall is a non-homogenous material made up from different layers (Fig. 1.2). The further the indentation the more layers will be affecting the interaction between the tip and the sample and this may complicate data interpretation. This led to experiments being carried out to determine the effects of varying these parameters and arriving at suitable values for future experimentation. These optimisation experiments were carried out on epidermal cells from intact *Arabidopsis* leaves and are also described here.

2.2 Methods

2.2.1 Sample Preparation

Arabidopsis seeds (col-0 background and relevant transgenic lines) were first surface sterilised in 1ml of a solution of 20% (v/v) bleach (economy bleach, SLS) with 0.05% (v/v) tween-20 for 10 mins and rinsed 3 times with autoclaved water to remove contaminants. Seeds were then stratified at 4 °C in a fridge for 4 days to break dormancy in 300 μl of autoclaved water. Seeds were plated on square petri dishes (12 cm x 12 cm) containing half concentration Murashige and Skoog growth media (1/2 MS) (Sigma-Aldrich) [76] with 1% (w/v) sucrose and 0.8% (w/v) plant agar (Duchefa Biochemie). Plates were sealed with micropore tape (3M) to keep out contaminants.

For experiments on the hypocotyl, seeds were germinated and grown in the dark at 22 °C/20 °C 16h day/night cycle for 4, 6, and 8 days. Plates were wrapped in foil to keep out the light and oriented vertically in the growth chamber to allow for hypocotyl extension. Entire seedlings were then transplanted to glass slides (75mm x 25mm) (ThermoFisher Scientific) for measurements. The hypocotyls were held to the glass

slides using a 1% (w/v) agarose (Duchefa Biochemie) solution and kept under a drop of autoclaved water.

For experiments on the leaves, seedlings were grown for 21 days at 22 °C/20 °C 16h day/night cycle on horizontal plates. Leaf two or three was chosen as these leaves were the flattest and were large enough to allow access by the AFM probe (Fig. 2.1). Leaves were excised, attached to glass slides (75 mm x 25 mm) (ThermoFisher Scientific) using an epoxy dental silicone (Provil Novo Light, Heraeus) and kept under a drop of autoclaved water (Fig. 2.2).

The tissue is kept under a drop of water to prevent drying and a loss of turgor pressure. The act of excising the leaf tissue and immersing it in water is would be expected to increase the turgor pressure of the cells within the leaf. This increase in turgor pressure is not expected to effect the AFM measurements, as the force applied by the AFM is minimal and indentation is only within the top 100 nm of tissue. A similar experimental setup is used by Braybrook *et al* [69], where they excise the shoot apical meristem and perform AFM measurements under water.

2.2.2 AFM procedure

The AFM used in this study was an Asylum Research MFP3D mounted on an inverted optical microscope (Olympus IX71). Sharp silicon nitride levers (SNL, Bruker) of nominal stiffness 0.35 Nm^{-1} and nominal resonant frequency 65 kHz were used for this study.

Before performing force indentation measurements the AFM needs to be calibrated. First a reference force curve was acquired, under liquid, on an incompressible surface, in this case a glass microscope slide. This allows the software to relate the deflection of the cantilever to a change in voltage from the detection photodiode. This measurement gives an InvOLS (inverted optical lever sensitivity) value which relates the deflection of the cantilever (in nanometres) to the voltage measurement on the photodiode (in

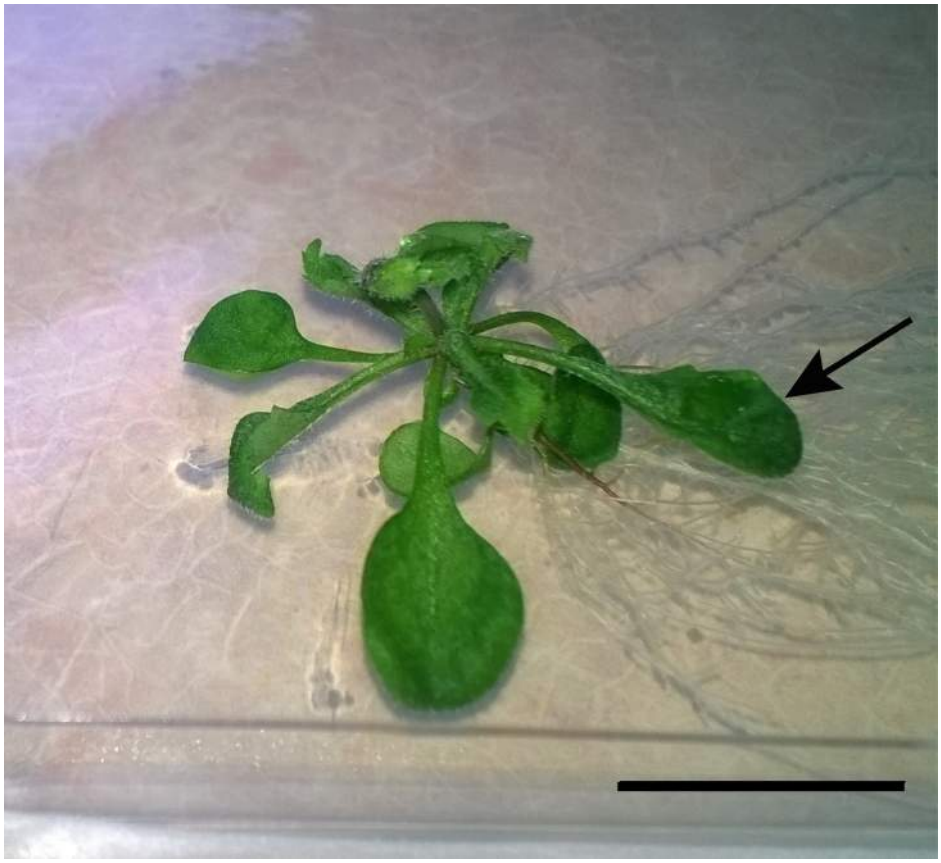

Figure 2.1: An *Arabidopsis* plant grown on 1/2 MS growth media. The arrow shows leaf 3 which was the leaf chosen for experimenation. Scale bar = 2 cm

Figure 2.2: A leaf excised from an *Arabidopsis* plant. Dental silicone is spread onto the glass microscope slide and the leaf is carefully pressed into it. Scale bar = 1 cm

volts) and is usually measured in nanometres per volt (nm/V). To relate the deflection of the cantilever to a force applied to the sample surface the spring constant, or the stiffness, of the cantilever needs to be measured. By performing a thermal tune this value can be estimated (see section 1.4 for a detailed description). Once both these values are known, measurement can begin.

Samples were prepared as in section 2.2. Microscope slides with the samples attached were placed under the scanning head of the AFM and autoclaved water was applied. The AFM was engaged to the sample surface in contact mode with a set-point of 1V (corresponding to a force of around 30 nN). Images of around 25-30 μm square were taken at a line rate of 1Hz to find an area of interest. Once an area of interest had been located a 10 point x10 point force map with a trigger deflection of 100 nm and a curve acquisition rate of 1 Hz was acquired. The trigger point sets the maximum deflection of the AFM cantilever. Once this value is reached, the AFM stops indenting and the cantilever retracts. The AFM used here has a maximum cantilever travel range of 12 μm in the vertical. 1 Hz at the maximum z range of 12 μm corresponds to a tip velocity of 24 μm s^{-1}. This value was chosen to minimise the force mapping time to keep tissue as viable as possible.

2.2.3 Morphological limitations

A major limitation in performing AFM on live plant tissue is its geometry. For AFM to be viable, the sample must be sufficiently flat and small enough to physically fit under the AFM head, and secure enough so it remains stationary during measurements. All AFMs have a maximum z range, that all features within a scan must remain in. For most commercial, general use AFMs this range is between 10-15 μm. The AFM used in this study has a z range of 12 μm. The topographical variation in plant tissue samples, especially the leaves, limits the maximum horizontal scan size to around 30 μm in the case of leaf tissue. Any larger than this and the scan would include features

out of the 12 μm vertical range of the scanner (Fig. 2.3). This makes selection and preparation of the samples of great importance. In the case of the hypocotyl, as long as the sample was flat, scanning along the top of the hypocotyl was relatively simple. In the case of leaves, the flattest leaf on the plant was chosen, which tended to be leaf 3 or 4 as older leaves start to curl at their edges and younger leaves are too small to access reliably.

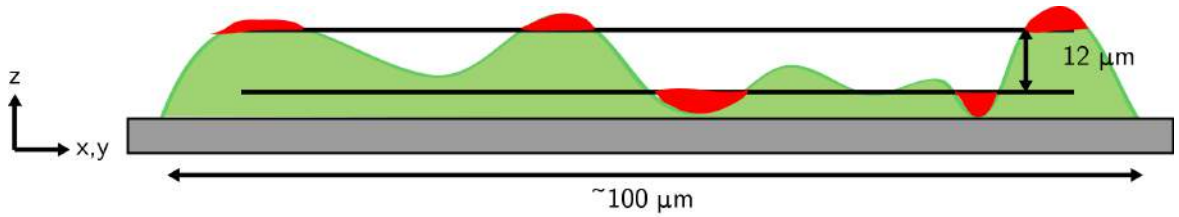

Figure 2.3: For a scan to be successful, the entirety of the surface must be within 12 μm in the z direction, within the horizontal lined area. The AFM will fail to track the surface if the sample is above or below this range (red areas)

2.3 Results and Discussion

2.3.1 Hypocotyl

As the top of the hypocotyl was relatively flat, large areas could be scanned in contact mode without the issues mentioned in section 2.2.3 arising (Figure 2.4).

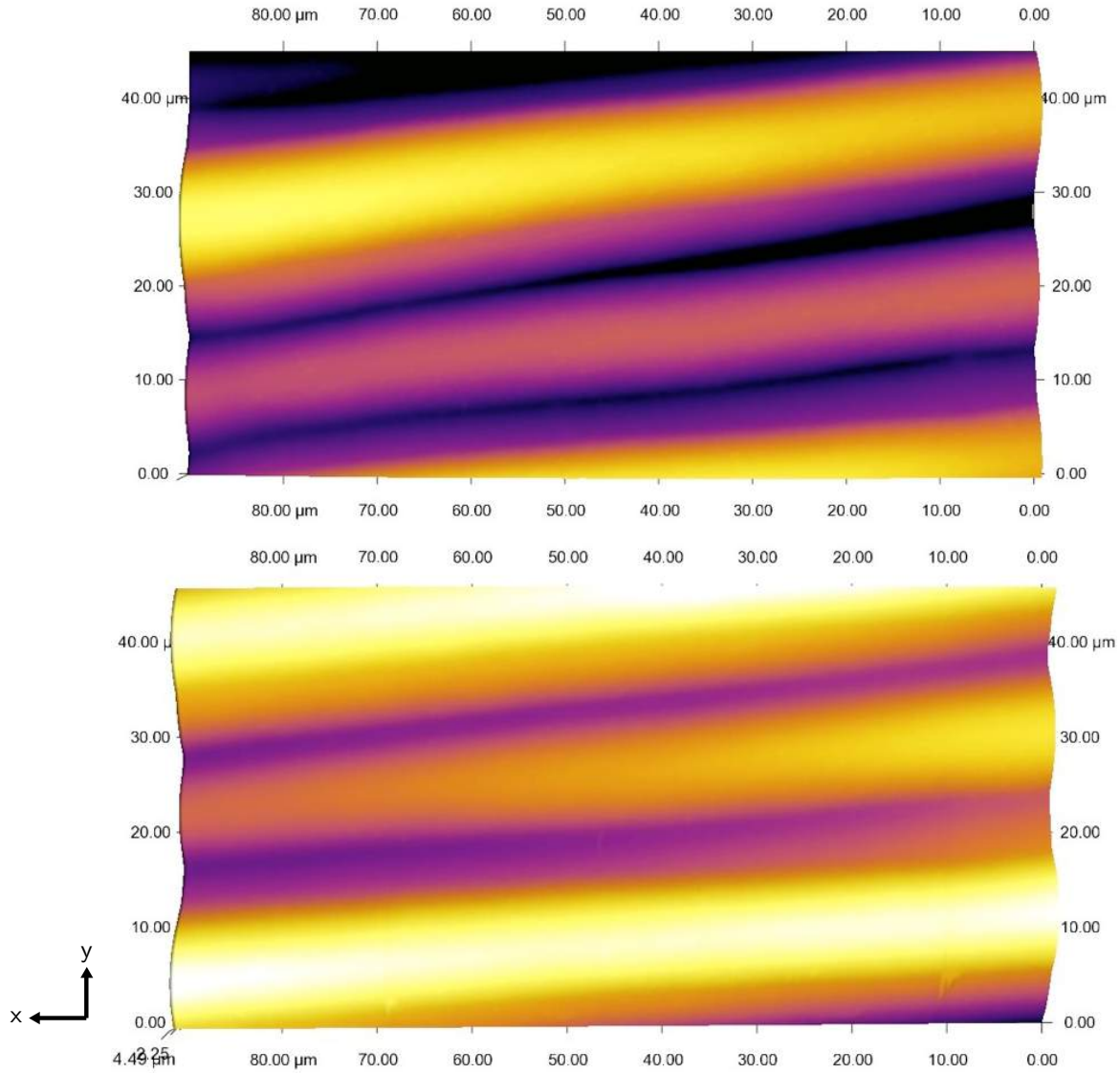

Figure 2.4: Two typical AFM contact mode height images of the hypocotyl of wild type *Arabidopsis* plants. The x, y and z axes are spatial axes with the x scale being 90 μm, the y scale being 45 μm. The colour scale indicates the height (z) running from black at the lowest points to white at the highest. Black = 0 μm, White = 4.5 μm.

The shape of the contact section of the force curves gives an indication of the type of interaction occurring. If the contact section is straight (as in figure 2.5) then it implies

that the surface area of contact between the tip and the sample is not changing during measurement and that the sample is being deflected or pushed down as apposed to being indented. If the contact area were changing, we would expect a higher order power law relationship between force and z movement. Figure 2.5 shows some representative force curves acquired on glass and on the hypocotyl, most curves acquired were of this form. The curve taken on glass is used as a reference. The curve taken on the hypocotyl shows a mainly linear relationship between force and z movement with a slight curve near the contact point, showing that a small amount of indentation occurred before the sample was displaced downwards.

Due to the unusual form of these curves, and the fact that an accurate value of indenter geometry would be hard to obtain, it was decided to report an apparent stiffness value.

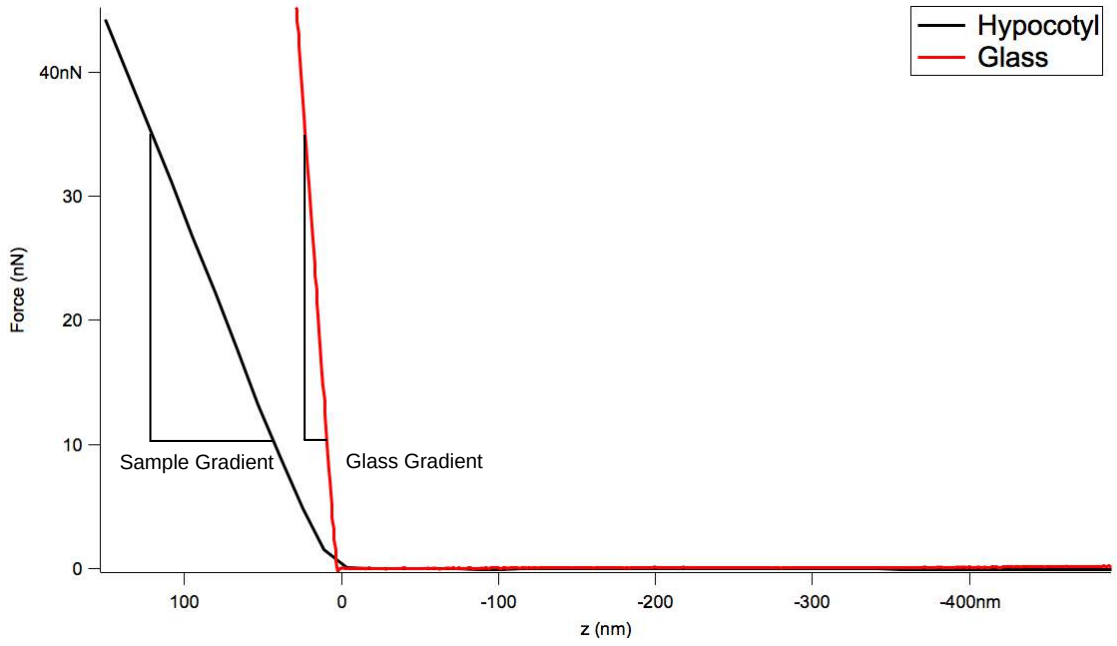

Figure 2.5: Representative force curves from the first experiment on the hypocotyl. The red curve is the reference curve taken on glass for calibration purposes. The black curve is the curve taken on the hypocotyl. The shape of the curve indicates the type of interaction (indentation/displacement) occurring between the tip and sample and the gradient is proportional to the stiffness (Hooke's Law).

Stiffness values were calculated by assuming the ratio of the gradients of the contact section of the force curves between glass and the sample were equal to the ratio between

the stiffness of the cantilever and the sample. The gradients of the force curve relate the force applied to the sample to the indentation of the probe tip. Gradients of the force curves were calculated by fitting a straight line to the entire contact section. The AFM software fits a line to the force curves and returns an InvOLS value (Inverted optical lever sensitivity), which is the reciprocal of the gradient. Knowing the stiffness of the cantilever and the InvOLS values of curves taken on the sample and on glass, we can calculate the sample stiffness as:

$$\frac{k_{sample}}{k_{cantilever}} = \frac{Grad_{sample}}{Grad_{glass}} = \frac{InvOLS_{glass}}{InvOLS_{sample}} \tag{2.3.1}$$

$$k_{sample} = k_{cantilever}\frac{InvOLS_{glass}}{InvOLS_{sample}} \tag{2.3.2}$$

Where $k_{cantilever}$ is the stiffness of the cantilever, measured as in section 1.4, k_{sample} is the calculated stiffness of the sample, InvOLS$_{glass}$ is the inverse of the gradient of the reference force curve and InvOLS$_{sample}$ is the inverse of the gradient of the force curve measured on the sample. These calculations make the assumption that the surface being indented behaves like a linear spring, where the force applied to the surface is directly proportional to the distance displaced. This assumption was deemed valid due to the fact that the force curves (Fig. 2.5) were linear for the contact section.

This approach allowed us to calculate an average stiffness per force map. Analysing a number of plants for the same treatments allowed us to get averages for each of the treatments and samples outlined in Tables 2.1 and 2.2.

Age (days)	4		6				8			
Line	L10		L10		col0		L10		col0	
Treatment	-	+	-	+	-	+	-	+	-	+
n	4	4	11	5	2	2	5	5	9	7

Table 2.1: Number of replicates for the first experiment. The age is how many days after germination the hypocotyl was measured, the line is which transgenic line was used (see section 2.1) the treatment shows whether dex was used to induce expression or not and n is the number of hypocotyls measured.

Age (days)	4							
Line	col0		CycD3		L9		L10	
Treatment	-	+	-	+	-	+	-	+
n	1	5	3	3	2	3	9	9

Age (days)	6							
Line	col0		CycD3		L9		L10	
Treatment	-	+	-	+	-	+	-	+
n	2	4	3	2	3	3	6	7

Age (days)	8							
Line	col0		CycD3		L9		L10	
Treatment	-	+	-	+	-	+	-	+
n	5	5	3	3	2	3	7	7

Table 2.2: Number of replicates for the second experiment. The age is how many days after germination the hypocotyl was measured, the line is which transgenic line was used (see section 2.1) and the treatment shows whether dex was used to induce expression or not.

Tables 2.1 and 2.2 show the number of hypocotyl replicates used in each experiment: a total of 54 were used in the first experiment and 100 were used in the second experiment. Not all hypocotyls were deemed suitable for measurement as some were too small to effectively mount to glass slides and measurements on some resulted in no useable data which accounts for the uneven number for different combinations of age, line and treatment.

Two experiments were performed on the hypocotyl. The first experiment focused on comparing the stiffness of hypocotyls from wild type plants (col0) and L10 plants in which expansin expression can be induced with dex. In a second, larger, experiment a second independent transgenic line with inducible expansin gene expression (L9) and a line with inducible CycD3 expression were included.

Results for hypocotyl stiffness for the two experiments are summarised in figures 2.6 (experiment 1) and 2.7 (experiment 2). Values shown are the averages +/- standard errors ($\frac{\sigma}{\sqrt{n}}$). Values of stiffness for the first experiment range from (0.29 ± 0.04) Nm^{-1} to (2.00 ± 0.11) Nm^{-1}. Values of stiffness for the second experiment range from (0.12) Nm^{-1} (n=1) to (0.28 ± 0.03) Nm^{-1}.

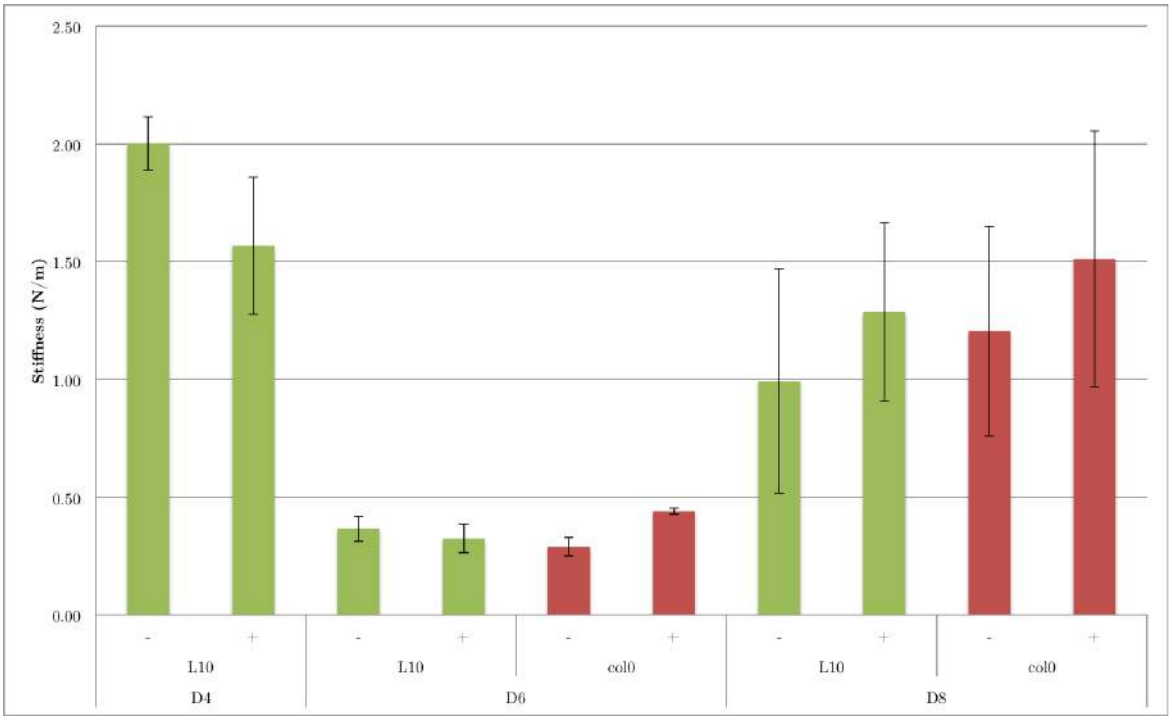

Figure 2.6: Graph of average stiffnesses (error bars, standard error) of the hypocotyl for the first experiment. + or - indicates whether the hypocotyl received a dex treatment for gene induction. col0/L10 is the plant line. D4/D6/D8 are the days after plating when the measurements were performed. (L10, green. col0, red)

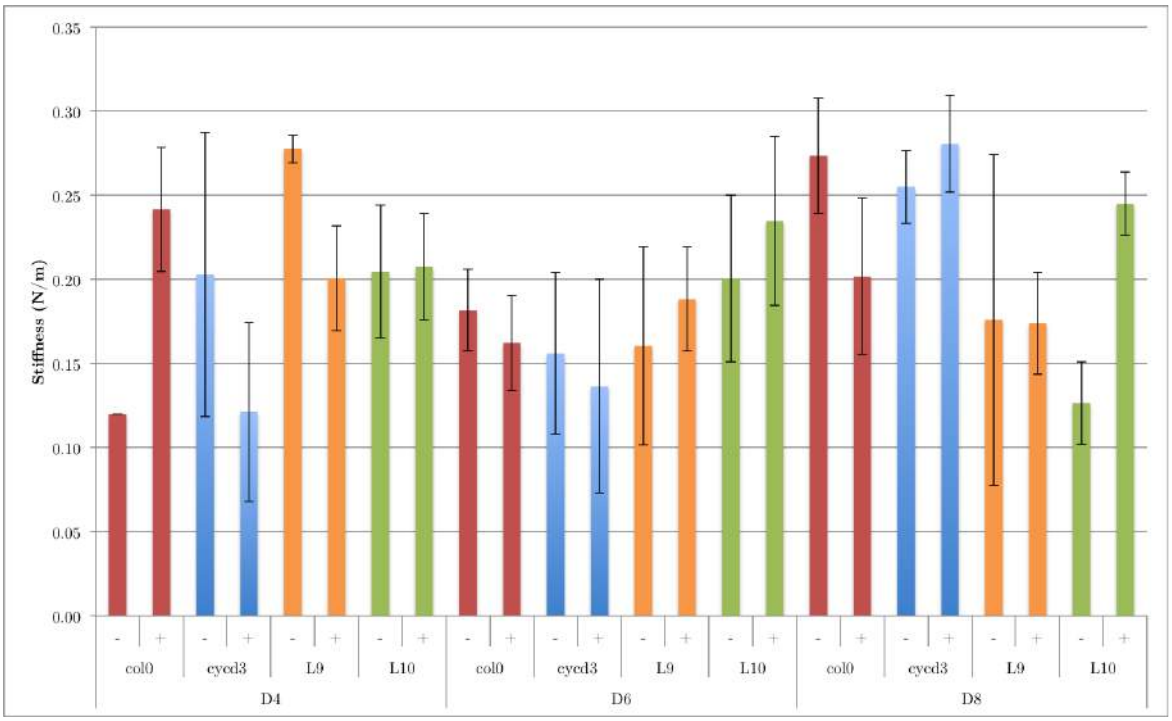

Figure 2.7: Graph of average stiffnesses (error bars, standard error) of the hypocotyl for the second experiment. + or - indicates whether the hypocotyl received a dex treatment for gene induction. col0/CycD3/L9/L10 is the plant line. D4/D6/D8 are the days after plating when the measurements were performed.(col0, red. CycD3, blue. L9, orange. L10, green)

Results from the first experiment (Figure 2.6) show that both L10 and col0 hypocotyls showed a marked increase in stiffness between days 6 and 8. Although results for col0 at day 4 unfortunately were not collected, for the L10 hypocotyls there is a decrease in stiffness between days 4 and 6 before the increase at day 8. However, due to the variation in the measurements for day 8, these results are not statistically significant.

An overall increase in tissue stiffness with age (from day 6 to day 8) would fit with the reported growth rates of hypocotyl tissue which shows a gradual decrease with time. The initial high level of stiffness in the day 4 L10 hypocotyls is unexpected but in the absence of the control data for this time point these data are difficult to interpret. Considering the L10 line, the results from this first experiment did not indicate any marked change in tissue stiffness as a result of the induction process, either at day 6 or day 8 when compared to col0 hypocotyls.

The results for the second experiment (Figure 2.7) are a little harder to interpret. The values of stiffness all range between 0.12 Nm^{-1} and 0.28 Nm^{-1}, whereas in the first experiment the maximal stiffness ranged up to 2 Nm^{-1} for the same line and the same time point. For example, the induced L10 hypocotyls at day 8 measured (1.29 $\pm$ 0.38) Nm^{-1} in the first experiment and (0.17 $\pm$ 0.03) Nm^{-1} in the second. The reasons for this large difference was not immediately obvious and this led to further investigations described below. Allowing for this major caveat, there was no obvious trend in altered stiffness between different lines and time points in the data shown in Figure 2.7. The increase in stiffness between day 6 and day 8 observed in experiment 1 was not convincingly shown in experiment 2.

Figures 2.9, 2.10, 2.11 and 2.12 show individual force maps for some of the hypocotyls measured in experiment 2.

By looking at individual force maps, some interesting insights became apparent. For some hypocotyls (e.g. figures 2.9 and 2.11) the distribution of stiffness values across

the surface is seemingly random. For others though (figures 2.10 and 2.12) the stiffness seemed to correlate quite well with the topography. The stiffness in these maps was lower at the cell junctions than the top of the cells. The tops of the cells were in some cases 1.5 times the stiffness measured at the junctions. This backs up the results reported in research by Routier-Kierzkowska *et al* [70] where they noticed a similar variation in stiffness again reporting a 1.5 times increase in stiffness at the tops of cells. They put this variation down to an as yet unidentified gusset of softer material filling in the gaps at the top of cell-cell junctions, although they show no evidence of this.

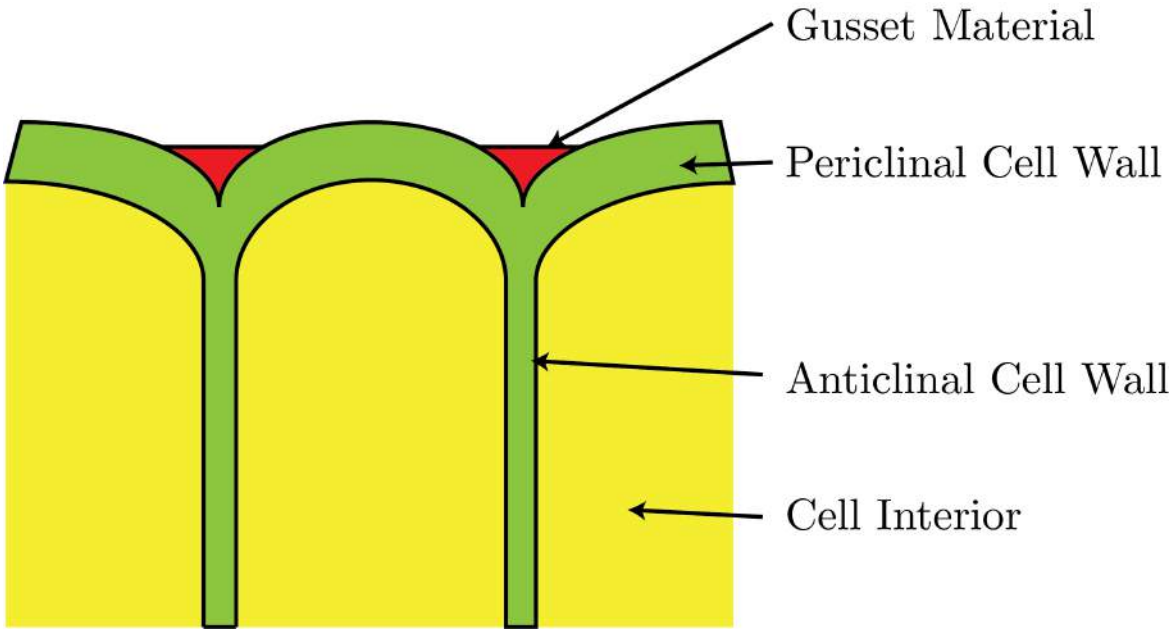

Figure 2.8: Cross sectional diagram of a hypocotyl, looking along the length. The theorised softer gusset material is present at the surface above the cell junctions. It is this that Routier-Kierzkowska *et al* say accounts for the reduced measured stiffness in their results.

The results shown in figure 2.6 and 2.7 indicated a high degree of variation between essentially very similar biological samples analysed on different days in different experiments. Although this might reflect real underlying biological variability, it is also possible that at least some of this variation was due to some aspect of the AFM technology being applied to a complex biological material. For example, the equation for stiffness (equation 2.3.2) takes into account the cantilever properties that are easily measured, the stiffness and the deflection sensitivity, but other factors have an affect

on the measurements made. One such property is the tip shape. The tip shape affects the pressure the cantilever probe exerts on the sample. If the tip is blunt the contact area will be larger and the pressure exerted will decrease, this correlates with an apparent increase in stiffness. Conversely if the tip is sharp, the contact area will be reduced, increasing the pressure leading to a decrease in measured stiffness [77]. A further potential source of variation is in the effect of indentation depth on the measurement, and this is explored in the next section.

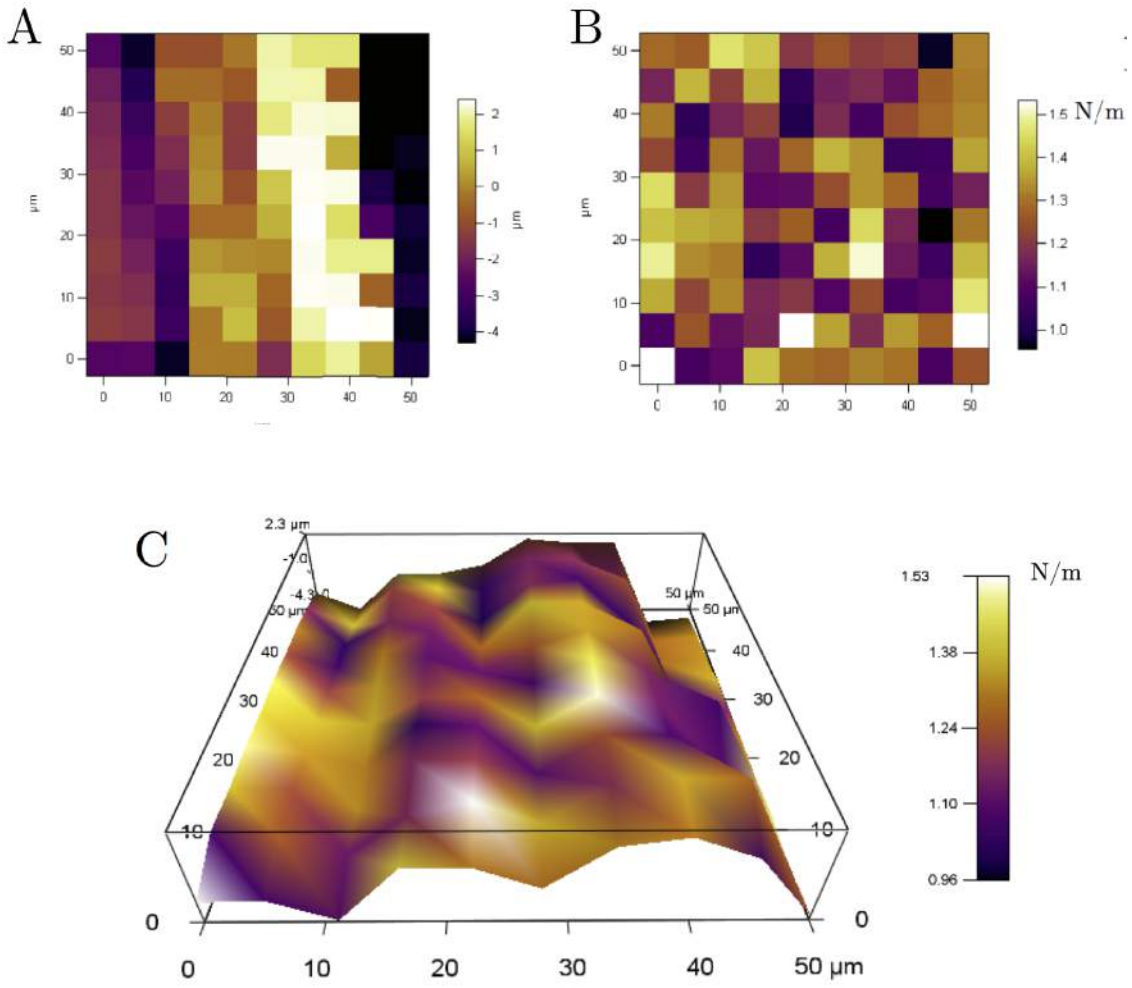

Figure 2.9: Data from a L10 hypocotyl from the second experiment. The hypocotyl is 8 days old and over expression was induced with dex. A, Map of height, the colour scale runs from -4 to 2 μm. B, Map of stiffness, the colour scale runs from 1.0 to 1.5 Nm^{-1}. C, 3D rendering of the height data with the stiffness data overlaid, the colour scale represents the stiffness, measured in Nm^{-1}. There is no correlation between morphology and stiffness in this example.

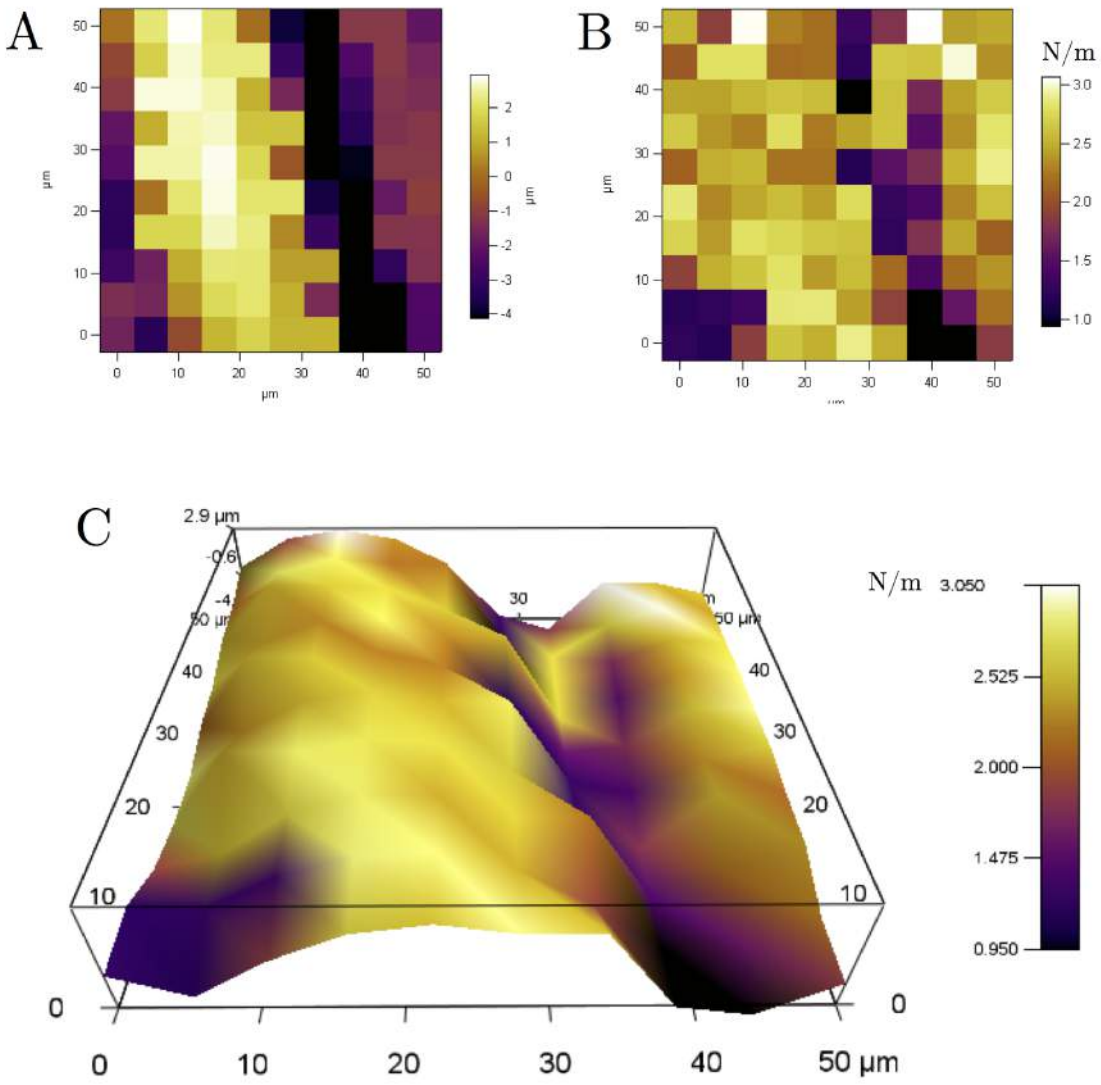

Figure 2.10: Data from a CycD3 hypocotyl from the second experiment. The hypocotyl is 4 days old and over expression was not induced with dex. A, Map of height, the colour scale runs from -4 to 2 μm. B, Map of stiffness, the colour scale runs from 1 to 3 Nm^{-1}. C, 3D rendering of the height data with the stiffness data overlaid, the colour scale represents the stiffness, measured in Nm^{-1}. There appears to be a correlation between morphology and stiffness here, with areas at the cell junctions having a lower stiffness than areas at the top of cells.

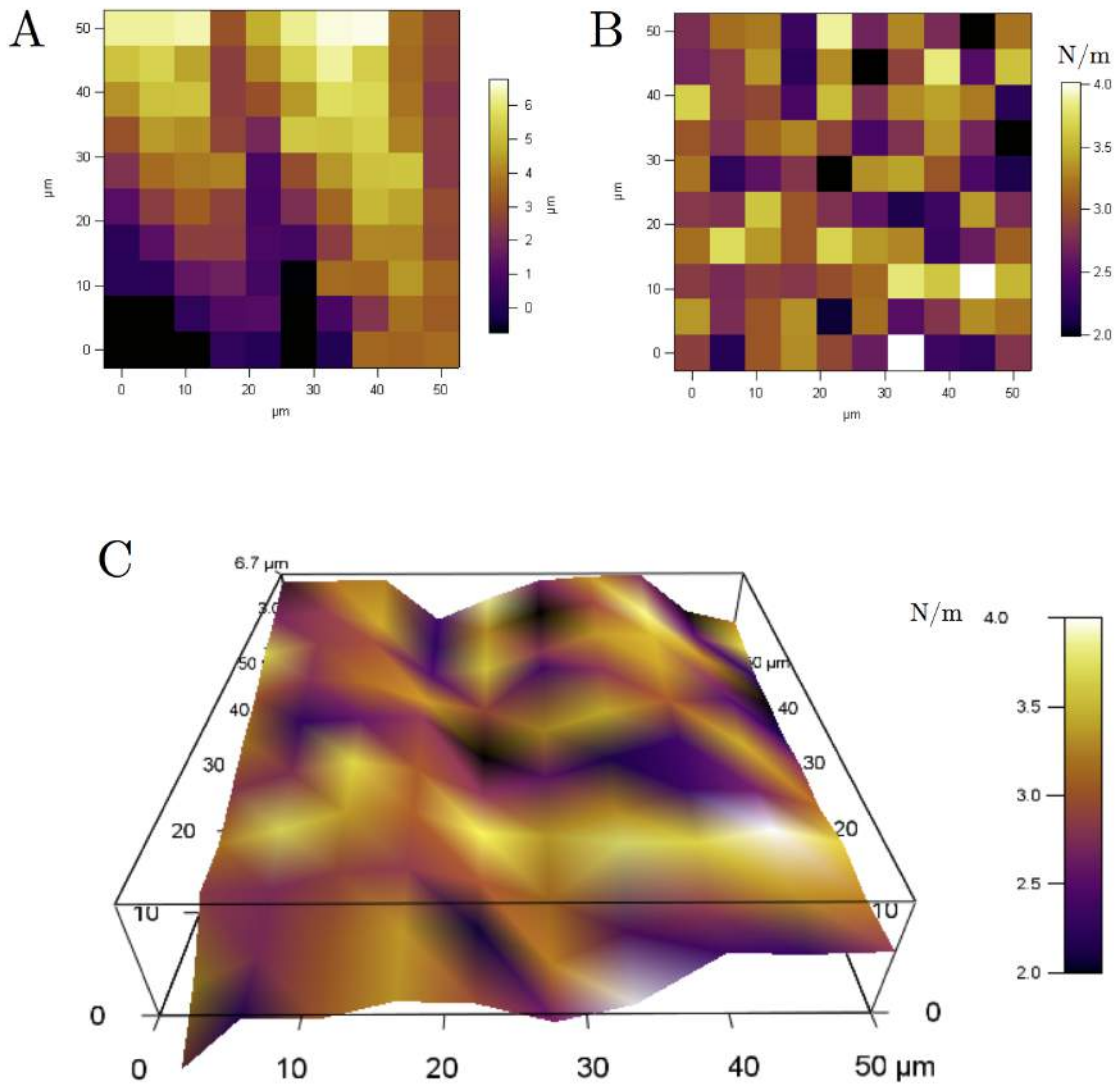

Figure 2.11: Data from a L9 hypocotyl from the second experiment. The hypocotyl is 6 days old and over expression was induced with dex. A, Map of height, the colour scale runs from 0 to 6 μm. B, Map of stiffness, the colour scale runs from 2 to 4 Nm^{-1}. C, 3D rendering of the height data with the stiffness data overlaid, the colour scale represents the stiffness, measured in Nm^{-1}. There is no correlation between morphology and stiffness in this example.

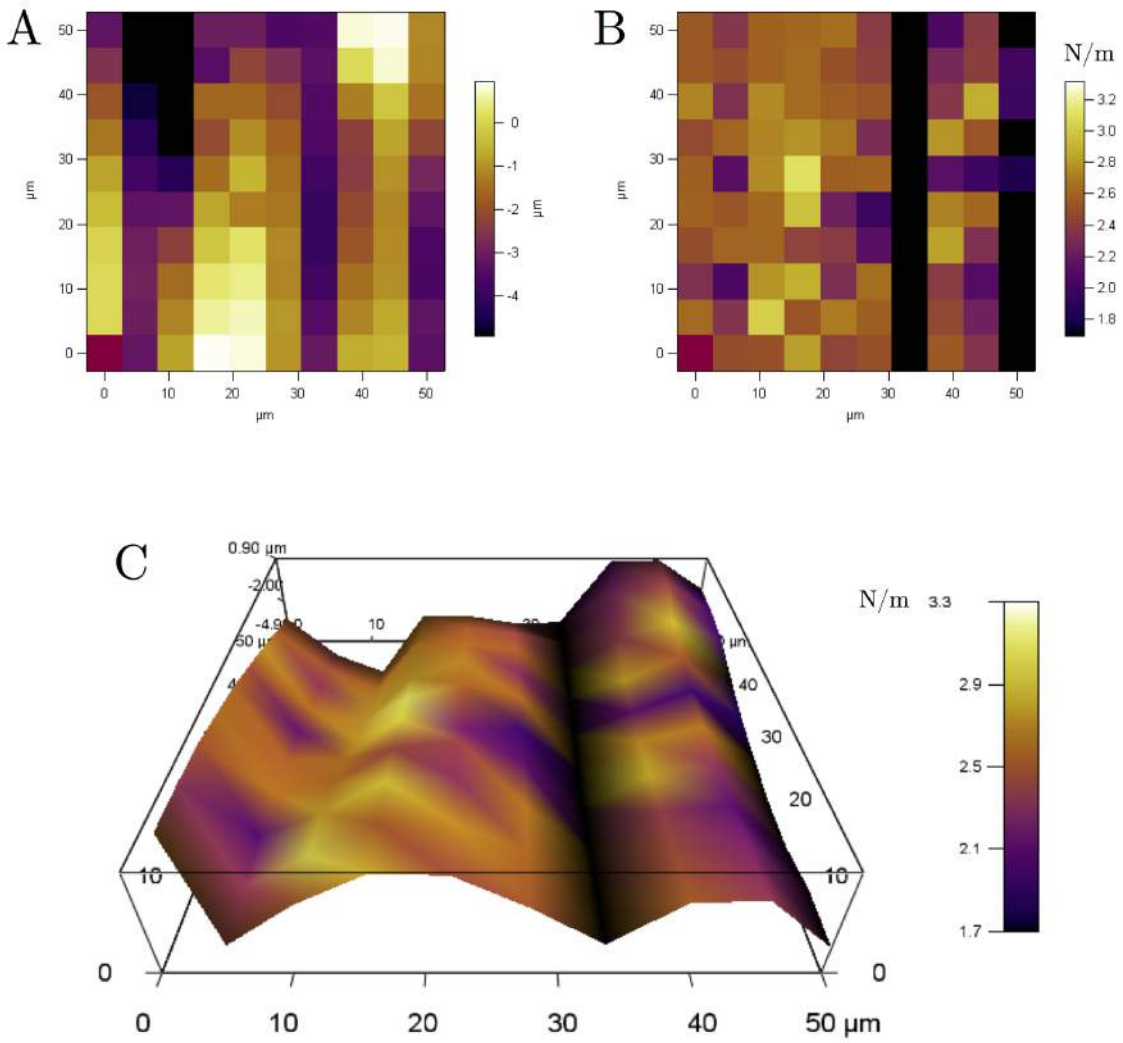

Figure 2.12: Data from a col0 hypocotyl from the second experiment. The hypocotyl is 6 days old and over expression was not induced with dex. A, Map of height, the colour scale runs from -5 to 1 μm. B, Map of stiffness, the colour scale runs from 1.8 to 3.2 Nm^{-1}. C, 3D rendering of the height data with the stiffness data overlaid, the colour scale represents the stiffness, measured in Nm^{-1}. There appears to be a correlation between morphology and stiffness here, with areas at the cell junctions having a lower stiffness than areas at the top of cells, although the difference is less pronounced in this example.

2.3.2 Depth Dependence of Stiffness Measurements

To test whether the depth we indent to during measurements has an effect on the values obtained, a series of experiments were performed. 25 x 25 point force maps were acquired on *Arabidopsis* leaf epidermal tissue at varying trigger values. For these force maps, the deflection of the cantilever was used as a trigger.

After calibrating the AFM (as described earlier in section 1.4), contact mode surface images were acquired to locate an area to acquire a force map. Areas of leaf epidermis in the centre of a cell were chosen for measurement to avoid the effects of indenting the cell-cell junction. Force maps were acquired with differing deflection trigger values to investigate the effect of indenting to different depths. A different area was used for each force map to avoid the effects of repeated indentation of the same area. Values quoted are the average values for a force map. Maps were acquired with trigger values of 20 nm, 50 nm, 75 nm, 100 nm, 150 nm, 175 nm, 180 nm and 190 nm to cover a wide range of indentation depths. The surface, whilst slanted, shows no significant morphology. Figure 2.13 shows some of the force maps acquired at these various trigger points, the colour scale shows the relative height and apart from 2.13B where the sample appears to have moved during measurement, the surface is relatively flat. The average indentation for these maps (+/- standard deviation) is shown in the graph in Figure 2.14.

Figure 2.14 shows the average indentation values for force maps against the value set for the deflection trigger point. Depending on the stiffness of the sample, and the stiffness variation as a function of indentation depth, the cantilever will indent the sample to different depths. From this we can deduce that the cantilever chosen for measurements was suitable as there is a measured indentation for each of the trigger values chosen. Figure 2.15 shows how the measured stiffness of the plant cell wall varies as indentation depth is increased. These values were calculated by averaging the stiffnesses (obtained by calculating the gradient of the force-indentation curves)

for each force map. Initially (from 20-60nm indentation depth) the measured stiffness of the wall increases, but then the rate of increase decreases so that by 120-160nm the measured stiffness reaches a plateau. If the contact area between the sample and the tip was increasing, then the stiffness would be expected to continually rise. As this was not observed, we have to assume that the tip is not indenting the sample after this indentation depth and that the cell wall is being displaced. As we are interested in measuring the properties by indenting the cell wall matrix, rather than measuring the force required for cell wall displacement, it was decided that future measures of stiffness would be calculated up to 40 nm of indentation.

Plants at this stage of development are not expected to have a mature waxy cuticle on the leaf epidermis or a secondary cell wall, as these processes occur only after cell expansion has ceased [8, 78], so the effect on measurements performed were deemed to be negligible.

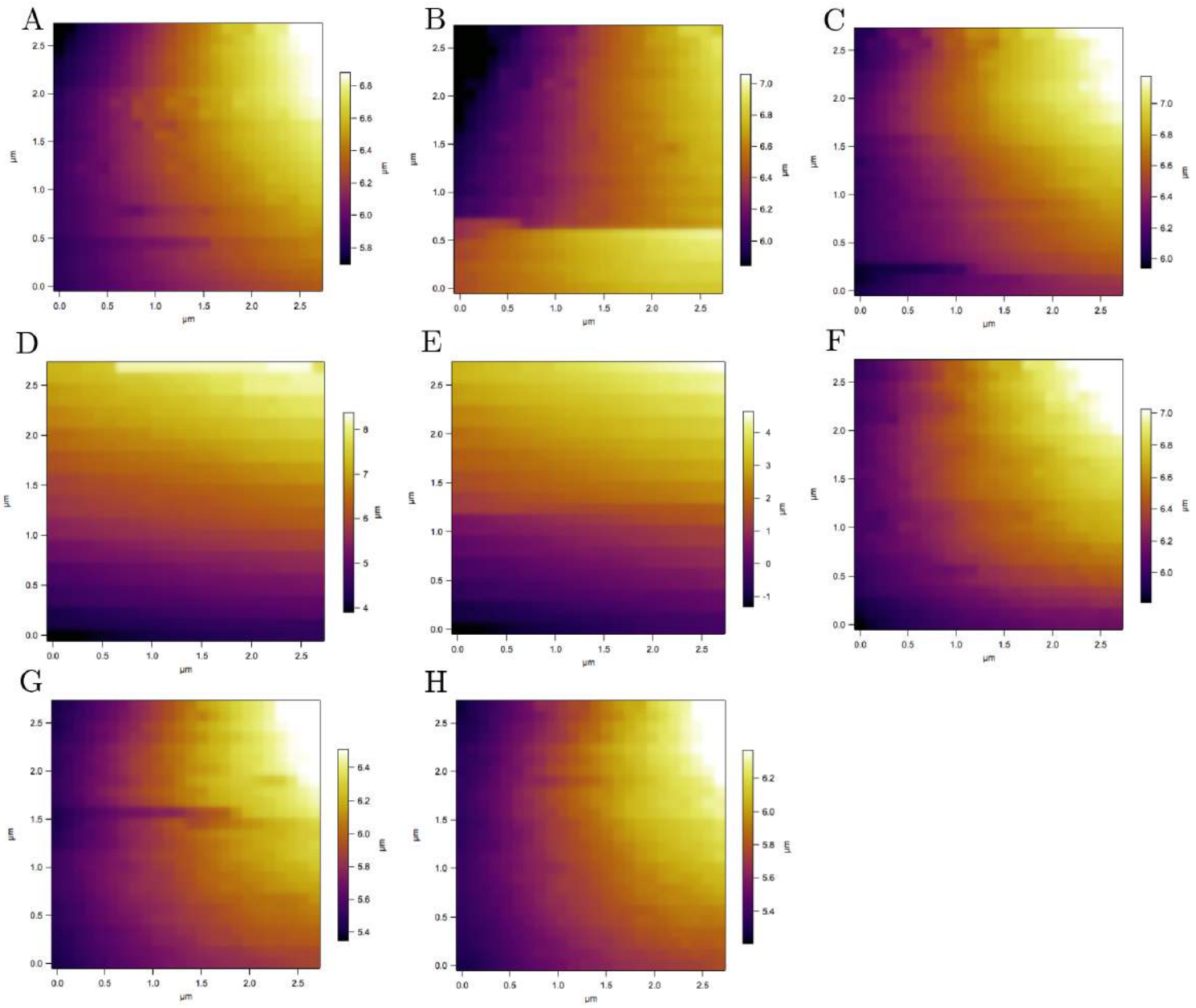

Figure 2.13: A-H, A series of height maps of leaf epidermis taken at varying deflection trigger values. A. 20nm deflection trigger B. 50nm deflection trigger C. 75nm deflection trigger D. 100nm deflection trigger E. 150nm deflection trigger F. 175nm deflection trigger G. 180nm deflection trigger H. 190nm deflection trigger

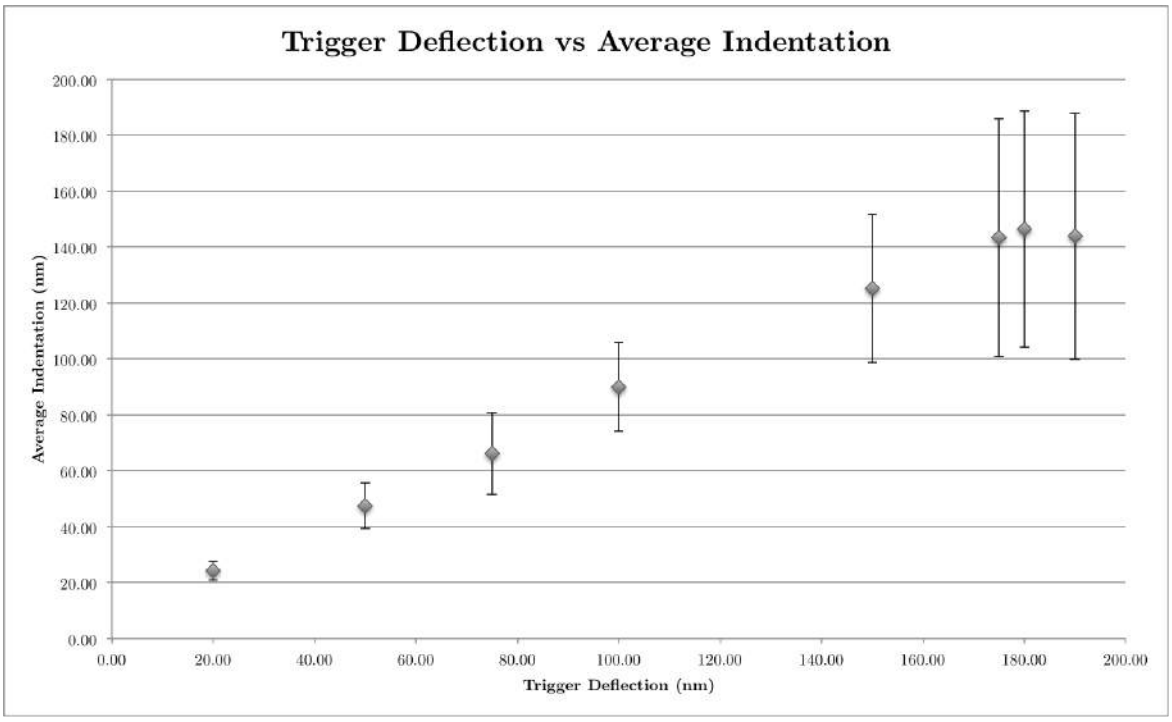

Figure 2.14: A graph of indentation vs. the deflection trigger value, error bars are standard deviation. There appears to be a linear relationship between the two variables up to 160 nm indentation. n=600 for each point.

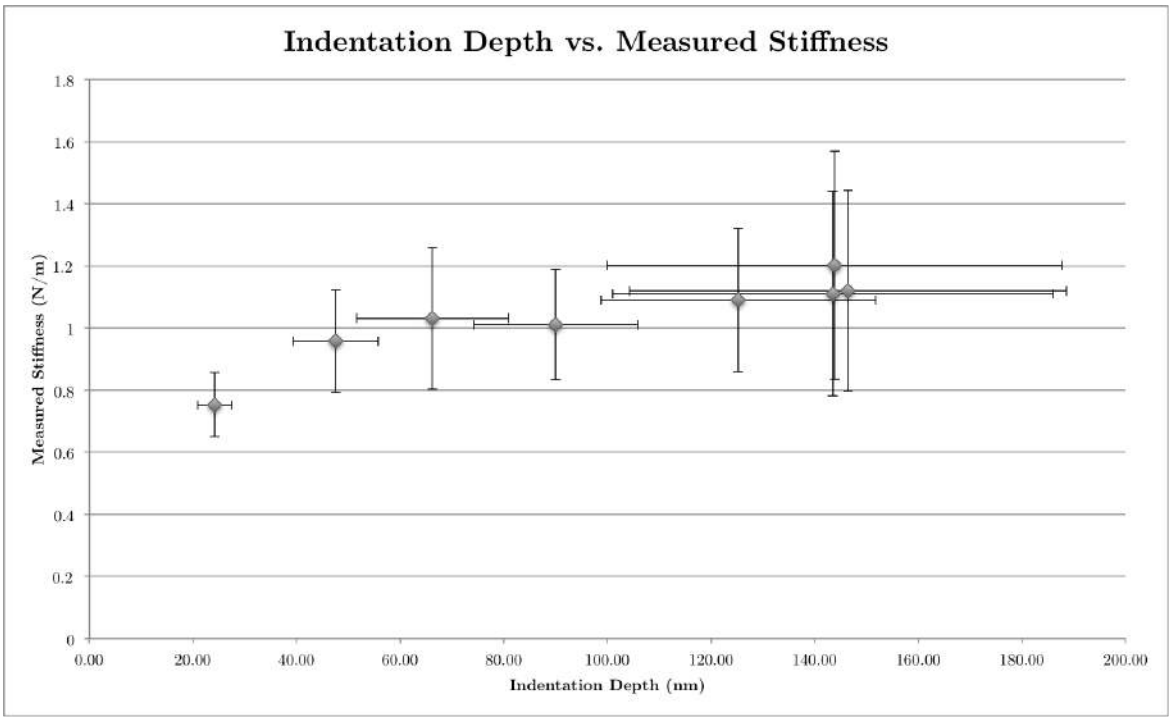

Figure 2.15: A graph of calculated stiffness vs. indentation, error bars are standard deviation. Once a certain indentation depth is reached the stiffness ceases to rise. n=600 for each point.

2.3.3 Indentation on an angled surface

A further potential source of variation in our measured values of stiffness is the potential for the topography of the surface to influence the values obtained.

As force is a vector quantity, the angle at which we indent the surface will have an effect on the measurements that are made. To test this effect, imprints of the leaf epidermis were made from dental silicone and the imprint subjected to AFM under similar conditions used for the living material. This dental silicone will have homogenous material properties and any variation in the measured properties should be due to the fact that not all the indentations are normal to the surface, thus giving an indication to the affect of topography on the data collected.

Leaves were excised from 21 day old plants and impressions were taken of the abaxial side with dental silicone. These impressions were mounted on glass microscope slides and placed under the AFM. Force maps were taken of areas where a range of indentation angles would be achieved.

By using the height data from the force maps and using the *surfnorm* function in Matlab, values for the normal vectors can be acquired. The *surfnorm* function performs a bicubic fit of the data in the x and y directions, calculates the diagonal vectors at each point and computes their cross-product to calculate the normal vectors (Figure 2.16).

By using the expression for the dot product (Eq. 2.3.5) of 2 vectors, an expression for the angle between them can be obtained. If $\mathbf{x}$ is the indentation vector (in the z direction) and $\mathbf{n}$ is the normal vector then:

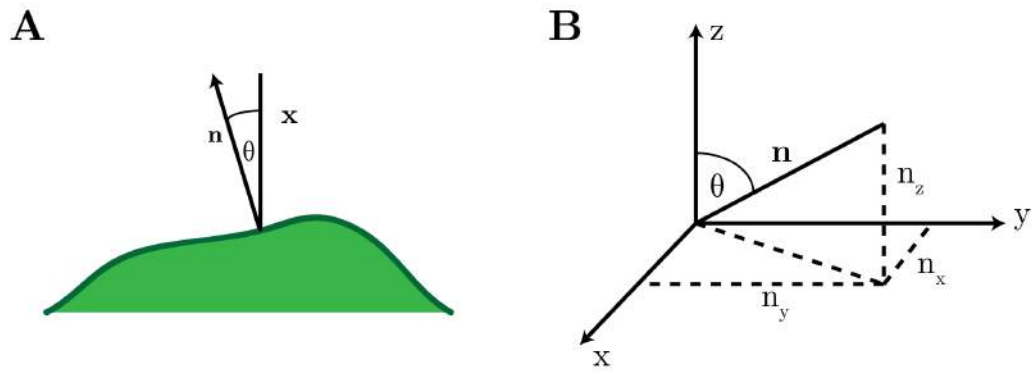

Figure 2.16: A, Diagram showing the relationship between the indentation vector, **x**, and the vector normal to the surface, **n**. B, the normal vector, **n** is made up of three orthogonal components, n_x, n_y and n_z, which are multiples of the cartesian unit vectors, $\hat{i}$, $\hat{j}$ and $\hat{k}$.

$$\mathbf{x} = \hat{k} \tag{2.3.3}$$

$$\mathbf{n} = n_x\hat{i} + n_y\hat{j} + n_z\hat{k} \tag{2.3.4}$$

$$\mathbf{x} \cdot \mathbf{n} = |\mathbf{x}||\mathbf{n}| \cos\theta \tag{2.3.5}$$

$$\mathbf{x} \cdot \mathbf{n} = \sum_{i=1}^{3} x_i n_i = n_z \tag{2.3.6}$$

$$|\mathbf{x}||\mathbf{n}| = \sqrt{n_x^2 + n_y^2 + n_z^2} \tag{2.3.7}$$

$$\cos\theta = \frac{n_z}{\sqrt{n_x^2 + n_y^2 + n_z^2}} \tag{2.3.8}$$

Where **x** and **n** are the vectors describing the indentation direction and the normal to the surface. n_x, n_y and n_z are the x, y and z components of the normal vector. $\hat{i}$, $\hat{j}$ and $\hat{k}$ are the unit vectors in the x, y and z directions and θ is the angle between the indentation vector and the normal to the surface.

If k_z is the stiffness measured in the z direction the the actual stiffness of the surface

will be $k_n = k_z / \cos\theta$.

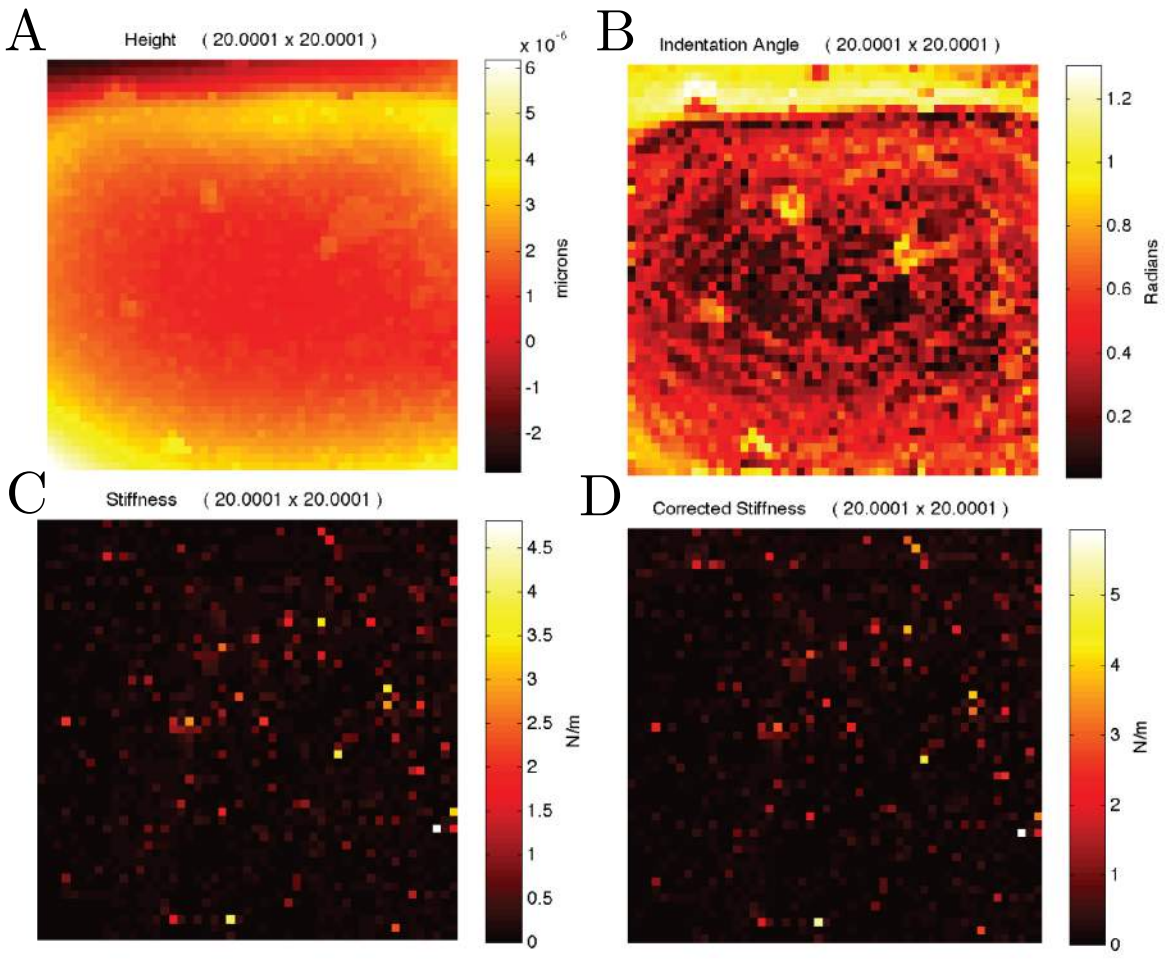

Figure 2.17: Force maps of dental silicone. A, Map of height. B, Map of the angle between the normal of the surface and the vertical indentation. C, Map of measured stiffness showing no correlation with the angle map. D, Map of corrected stiffness, again, showing no real correlation with the angle map.

Figure 2.17 shows force maps of a silicone impression of the surface of a leaf. Figure 2.17A display the height of the surface and Figure 2.17B shows the angle the surface normal makes with the vertical indentation. Figure 2.17C indicates the stiffness measured across the surface and Figure 2.17D displays the stiffness corrected for the angle of indentation using the method outlined above. The data in Figures 2.17 A and B indicate that the surface had a high degree of topography, leading to a range of indentation angles. However, both the uncorrected (Figure 2.17C) and corrected data (Figure 2.17D) for stiffness are highly similar and uniform (as expected for a homogenous material). These data indicate that the angle of indentation has no real

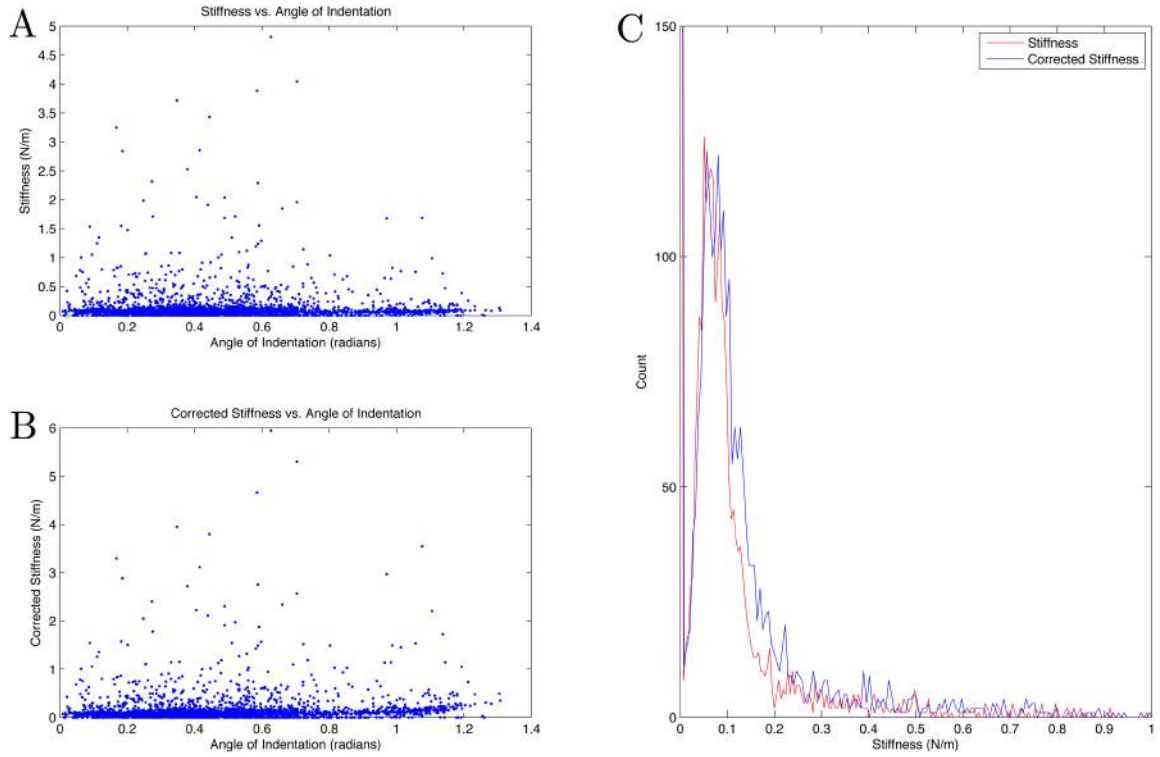

Figure 2.18: Graphs of stiffness variation with angle. A, Scatter plot of measured stiffness against angle of indentation. There is no significant correlation. B, Scatter plot of stiffness corrected for indentation angle against angle of indentation. Values at high angles of indentation have been raised slightly, increasing correlation. C, Distribution of stiffness values for uncorrected (red) and corrected (blue) stiffnesses, correcting for angle of indentation leaves the modal value of stiffness (the peak) unchanged.

effect on the measured value of stiffness in our system.

A statistical analysis of these data (Figure 2.18) supported this interpretation. Figure 2.18 shows the correlations between the stiffnesses and the angles of indentation. Figure 2.18A is a plot of the uncorrected stiffness against the angle of indentation. The correlation coefficient between stiffness and angle of indentation is -0.0180, which shows there is no significant correlation. If we correct for the angle of indentation (Figure 2.18B), there is actually an increase in correlation coefficient from -0.0180 to 0.0845, but still this values is not significant. The histogram (Figure 2.18C) shows the distribution of stiffness values for each of the stiffness maps, and shows that the angle correction does not change the representative modal value (i.e, the peak of the histogram) a significant amount. Due to the fact that these measurements showed little effect of angle of indentation on the stiffness values obtained, it was decided not to correct for angle in future analyses.

2.4 Conclusion

In this chapter I described a series of experiments performed on the hypocotyl and leaf epidermis of *Arabidopsis* to explore the use of AFM to obtain estimates of stiffness in living biological material.

The initial experiments on the hypocotyl indicated a high degree of variation in results between replicated experiments using similar biological material. Although some patterns were observed (e..g, a potential increase in hypocotyl stiffness between day 6 and day 8), these initial observations could not be replicated. To further explore potential reasons for the observed variability in data output, a series of follow on experiments were performed.

An investigation into the influence of indentation depth on stiffness values revealed that stiffness increased with depth (as expected) but only up to a value of about 60

nm. Beyond this depth the stiffness values reached a plateau which signifies the fact that the force curves became linear, as noted in section 2.3.1. For future experiments (described in the next chapter) stiffness measurements were restricted to the initial 30-40 nm of the plant cell wall. Through applying relevant models and by knowing the physical dimensions of the cell in question, and through optimisation of the experimental procedures it would be theoretically possible to obtain estimates of turgor pressure. Such measures were reported in [70], but the forces applied by their equipment were much greater than those obtained by AFM.

One potential concern was the topography of the plant material which might influence the stiffness values being measured. To test this possibility a series of experiments were performed using a homogenous material (dental silicone) with a topography similar to that of the biological material being investigated. The results of these experiments indicated that the surface topography did not have a significant influence on the stiffness values obtained, so this parameter can be discounted as a major source of variation in the data obtained. In the further experiments described in the next chapter, topography correction was not included.

A further potential source of variation in other researchers data output might be the model used to interpret AFM data. The Hertz model is the most widely used model of AFM indentation mechanics (although not used in this analysis) [46]. Despite the fact that the assumptions underpinning it are essentially incompatible with biological material, it remains the most popular method of extracting material properties from force-indentation curves. The Hertz model assumes a change in contact surface area as indentation increases. This means experiments using the Hertz model require an accurate measure of the tip geometry. For example, research performed by Braybrook *et al* used AFM cantilevers with a colloidal sphere attached to the end. By knowing the dimensions of this sphere, the contact area can be calculated relatively accurately and thus the Hertz model can be implemented relatively accurately. However, research outlined in this thesis used sharp silicon tips, where only nominal values of tip geometry

can be estimated. Such sharp tips greatly increase the spatial resolution obtained and allow measurements at sub-cellular resolutions. However, they also increase the potential source of error incorporated via application of the Hertz model since only nominal values of tip geometry can be estimated. Moreover, it is highly possible that tip geometry changes as a consequence of experimental contact with the material.

In the next chapter I describe a series of experiments focussed on a specific cell type in plants (stomata) which requires high-resolution, thus the use of sharp tips. The potential issues of interpreting these data using the Hertz model are explored further in that chapter.

These results highlight the fact that care needs to be taken when comparing measurements between different experiments as differences in experimental conditions may lead to differences in obtained results. The stiffness values obtained here depend not only on cell wall elasticity, but on turgor pressure [79], cell and tip geometry [80] and active processes within the cell, such as stress responses prior to measurement. As outlined above, although some of the variation in data described in this chapter might relate to the AFM method itself, it is also possible that the biological material under investigation (the hypocotyl) was also inherently variable. The target tissue comprised many cells which, although at first sight similar might have different molecular structure depending on their precise relative position within the tissue, the exact stage of development, or even minor variations in growth conditions. Such variability is an inherent issue with biological material and creates challenges for quantitative physical measurements.

To attempt to decrease the potential variability in the biological material, the decision was taken to attempt AFM measurements on a single specific cell type - guard cells.

Guard cells are found on the surface of all leaves, thus are easily accessible without major tissue preparation. They are easily identifiable by their cell shape, which should

ensure that there is a high level of confidence that comparable cells are being analysed in different experiments. Also, guard cells undergo a unique process of opening and shutting which is based on a physical/chemical process of altered turgor pressure acting on a surrounding cell wall, i.e., the guard cells have potentially interesting mechanical properties. In addition there is a large background literature on guard cell function at the genetic and physiological level, providing useful background context for an investigation of their mechanical properties. Finally, these cells play a vital role in plant function, controlling the exchange of gas (oxygen and CO_2) into the leaf and their is significant agronomic interest in the potential optimisation of guard cell structure/function.

For these reasons, an AFM study on the guard cell was initiated, the results of which are reported in the next chapter.

Chapter 3

Analysis of Guard Cell Mechanical Properties and their Role in Stomatal Function

3.1 Introduction

Following on from the work carried out in chapter 2 to establish an AFM technique for the analysis of plant tissue, the guard cell was chosen as the target for more detailed research.

Guard cells offer a useful target for developing a robust method of measuring cell wall mechanical properties. Due to the fact that they must change shape to function, it is theorised that they must possess differing mechanical properties from the cells that surround them and that different regions of the guard cell itself will have different mechanical properties. This difference in mechanical properties is thought to allow the cells to change shape as a result of changing their internal turgor pressure due to signals from external stimuli [81]. Due to the fact that it is technically possible to obtain the two guard cells that make up a stomata, plus some of the surrounding cells in the same

AFM scan, it should be possible to make relative quantitation of mechanical properties both within guard cells and between guard cells and neighbouring cells. This should ameliorate some of the issues identified in the previous chapter where the comparison of cell mechanical properties in different biological samples was rendered difficult by the apparent inherent variability in absolute values of stiffness measured. This chapter reports on a series of experiments to investigate the mechanical properties of guard cells using AFM.

Stomata are a dynamic system. The function of the guard cells is to change shape to open and close the pore of the stomate (the stoma), thus regulating gas exchange into and out of the interior of the leaf. Guard cells achieve this function by carefully regulating their turgor pressure. The main signalling molecule involved in stomatal closure due to drought stresses is abscisic acid (ABA) [82], and by applying this chemical to the fluid medium surrounding the leaf we can signal the stomata to close. ABA acts to increase the rate of ion transport out of the cell. The loss of these soluble osmolytes from the cell reduces the osmotic potential and causes water to travel across the cell membrane and out of the cell, reducing the turgor pressure and closing the stomata [83]. Another way of closing stomata is by using a solution of mannitol. In a mannitol solution the osmotic potential of the solution is changed, facilitating the transport of water out of the stomata and the surrounding cells vacuoles, reducing the turgor pressure and closing the stomata. By changing the medium the state of the stomata can be controlled, and the mechanics during these changes can be investigated.

Stomata play a key role in crop water use efficiency, closing in drought to minimise water loss, and opening to allow appropriate gas exchange. With a deeper understanding of the mechanisms of stomatal dynamics and the effects genetic manipulations have on these dynamics, there is a potential for improvements in drought tolerance meaning improvements in stomatal performance might have relevance in agronomy. Until now, most research in this area has focussed on the endogenous signals controlling stomatal

function (e.g., ABA) and the genes controlling stomatal formation. Much less work has been done on the actual mechanics of the cell wall which must play a key role in guard cell function.

Research carried out in the 1970s [84] used finite element shell analysis of the guard cell to measure deformations as a function of the pressure within the cells. They showed that a change in turgor pressure alone was not sufficient to change the pore width, it was the difference in pressures between the guard cells and their supporting cells that drove stomatal dynamics, with values differing by as much as 8×10^5 Pa. It is this pressure difference that drives the change in shape of the stomata. For stomata to be able to change shape in reaction to this pressure change, it would make sense for the guard cells to have differing mechanical properties to the supporting pavement cells.

More recent research carried out by Meckel *et al* [85] sought to investigate the changes in guard cell membrane surface area, and in turn volume, during stomatal opening and closing. They hypothesised that exo/endocytosis of the plasma membrane must occur during surface area change due to the fact the the membrane has a low extensibility. They measured changes of 25% and 15% of the volume and surface area respectively during these dynamic changes. Due to the fact that the cell wall and the plasma membrane are separate, and no material is removed from the cell wall as stomata close, the cell wall must be elastic to allow it to change shape and surface area.

In this chapter I will describe work carried out to try and measure and quantify the mechanical properties of guard cells, to attempt to gain a deeper understanding as to their structure and physical properties. Methods were developed to perform atomic force microscopy force volume measurements on intact leaves and custom data analysis procedures were coded and developed. Experiments were carried out to determine the effect that excising whole leaves and mounting them on dental silicone had on cell viability. Hormones and osmolytes were added to the AFM liquid imaging solutions to control and record the dynamics of stomatal opening and closing.

3.2 Materials and Methods

3.2.1 AFM Imaging and Force Measurements

Leaves were prepared for measurement as in section 2.2. Standard measuring procedure involved calibrating the AFM as previously described (see section 2.2.2). Slides containing the mounted samples were then placed under the head of the AFM and the cantilever was engaged to the surface. Depending on the roughness and topography of the sample, the scan size was set to between 20 μm and 30 μm and the scan rate was set to 2 Hz. This gave an imaging time of around 4 minutes. Once a stomata was located, (which took anywhere from 4 minutes to 40 minutes), a force map was acquired. If it took longer than 40 minutes to locate a stomata, the sample was discarded and a new leaf was prepared. Force maps of 50 x 50 pixel resolution were taken with an indent rate of 1 Hz. At this rate force maps took approximately 40 minutes to complete.

3.2.2 Checking Sample Viabiltiy

With leaves having been excised for up to an hour during measurement, it became apparent that their viability should be tested, to make sure measurements were still being performed on live samples.

To test the viability of cells within leaves that have been excised a fluorescein diacetate (FDA) stain was used [86]. In healthy cells the non-fluorescent FDA is converted into the green fluorescent compound fluorescein by esterases located within the protoplast and these will fluoresce green (emission at $\lambda = 521$ nm) when excited with ultraviolet light (excitation at $\lambda = 494$ nm). Membrane compromised cells will not convert the non-fluorescent FDA into fluorescein.

Plants were grown and mounted as if for AFM measurement (section 2.2). 3 cases

were tested: plants mounted on dental silicone and covered in autoclaved water for 40 minutes; leaves suspended in autoclaved water for 40 minutes; and leaves suspended in ethanol for 40 minutes. The ethanol treatment was expected to denature the cells in the leaf and act as a control. After the 40 minute treatment leaves were removed and stained with FDA. The staining solution was prepared by dissolving 5 mg of fluorescein diacetate (Sigma Aldrich) in 1 ml of acetone (Fischer Scientific). This was then diluted at 1% (v/v) with autoclaved water. Leaves were submerged in the FDA solution for 10 minutes before being rinsed with autoclaved water and mounted on glass slides (75 mm x 25 mm) (ThermoFisher Scientific). Samples were viewed under a stereo fluorescent microscope (Olympus IX51) at 100x magnification with GFP filter cube installed (excitation at λ = 450-490 nm, emission at λ = 520 nm). A digital camera (Olympus DP71) was used to capture images at a resolution of 4080 x 3072 pixels.

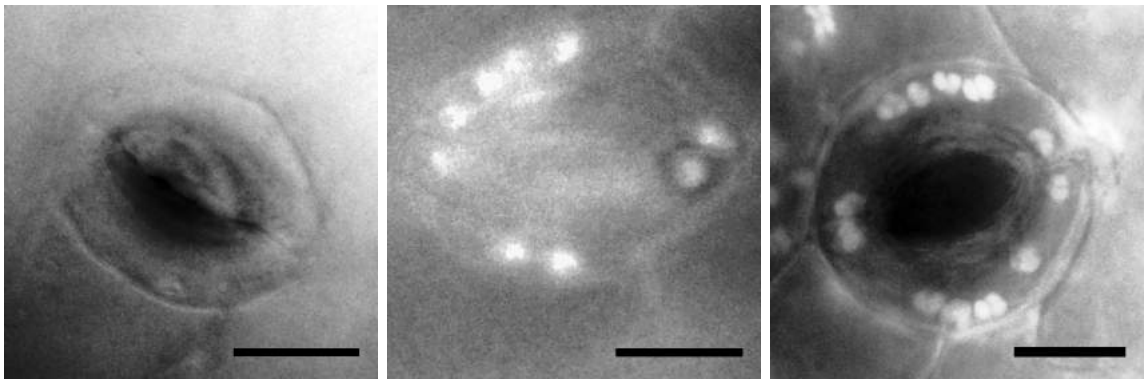

(a) Ethanol, no mounting media (b) Water, no mounting media (c) Water, Provil-Novo mounting media

Figure 3.1: Fluorescence micrographs of fluorescein diacetate stained guard cells. a) Stomate from a leaf immersed in ethanol before staining. b) Stomate from a leaf immersed in water before staining. c) Stomate from a leaf attached to a microscope slide with dental silicone and immersed in water before staining. b) and c) show localised fluorescence within the guard cells at the sites of FDA hydrolysis. Scale bars 20 μm

Representative fluorescent micrographs (Figure 3.1) show stomata in various states of health. Figure 3.1a shows a stomata that has been bathed in ethanol for 40 minutes. There is no localised fluorescence within the guard cells and this stomate is expected to be non-viable. Conversely, Figures 3.1b and 3.1c (stomata that have been bathed in water for 40 minutes) show areas of localised fluorescence within the guard

cells and are expected to be viable. These representative images are typical of all the images obtained. 3 micrographs were captured from each leaf and 2 leaves were used for each treatment totalling 18 micrographs. The percentage of stomata with localised fluorescence for each treatment is shown in table 3.1. Approximately 90% of all water-immersed and processed stomata showed a positive viability test. From this it was concluded that excising the leaves and using dental silicone as a fixative had no significant effect on the viability compared to excising the leaves and submerging in water, up to the measured time point of 40 minutes.

	Percentage of Stomata with Localised Fluorescence	
Ethanol, No Media	0%	n= 22
Water, No Media	92%	n= 24
Water, Provil Novo Media	89%	n= 18

Table 3.1

3.2.3 The Challenge of Locating Stomata

One of the major bottlenecks in the stomata force measurements procedure was locating stomata using contact imaging mode on the AFM. Typically, the abaxial side of an *Arabidopsis* leaf has 200 stomata per mm^2. If the maximum xy scan size of the AFM is 100 μm x 100 μm, then there will be, on average, 2 stomata in that area (Figure 3.2). If we scan at 25 μm x 25 μm, then on average, there will only be a stomata in 1 out of every 8 scans. This, coupled with the morphological difficulties outlined in section 2.2.3 (high topographic variation in the leaf surface), meant that a lot of sessions using the AFM resulted in no usable data.

Certain *Arabidopsis* mutants have been developed to express green fluorescent protein combined with genes that are only expressed within guard cells. One of these genes, APK1 (Arabidopsis protein kinase 1), is expressed only in stomata and is involved in stomatal signalling (Figure 3.3). It was suggested that if we could locate stomata with the AFM fluorescently, then this would greatly speed up the data acquisition

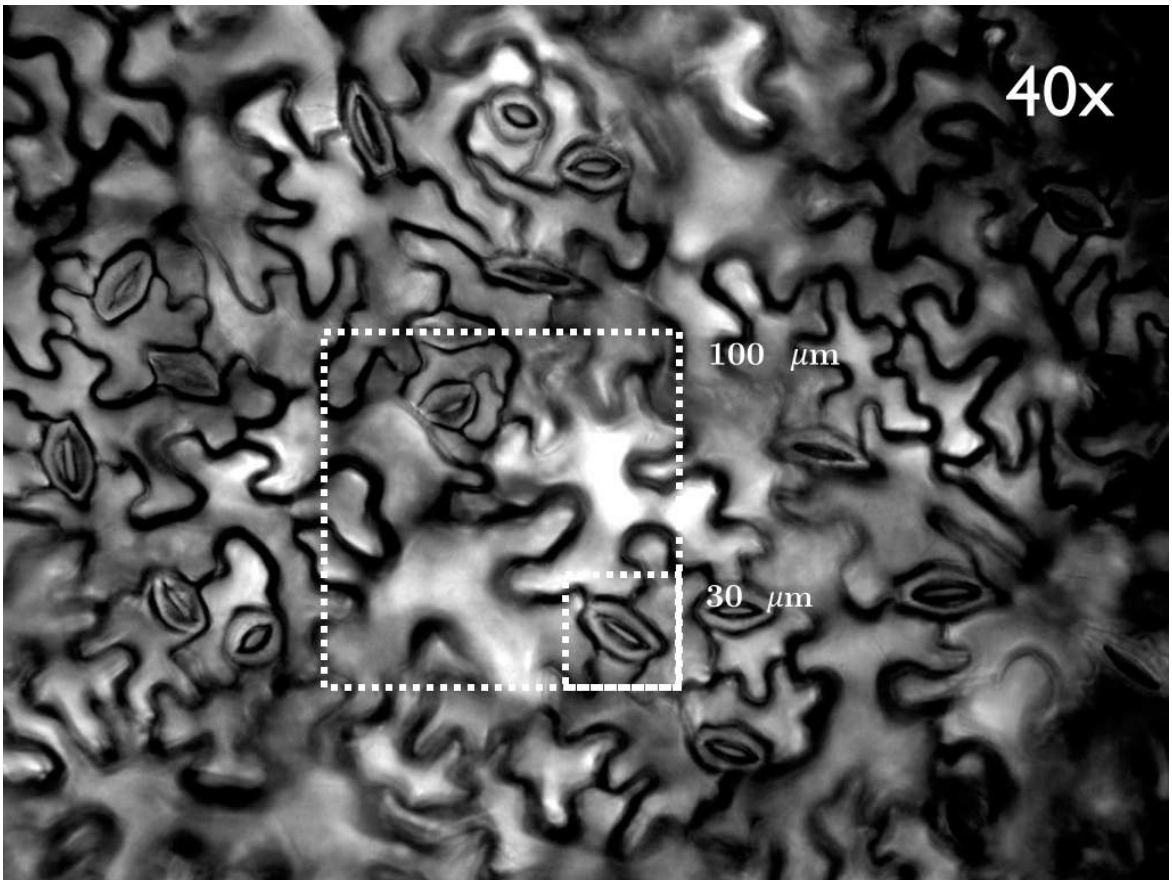

Figure 3.2: A 40x differential interference contrast micrograph of the abaxial leaf surface. The larger square shows the maximum scan size of the AFM whilst the smaller one shows the typical scan size achieved during measurement

process.

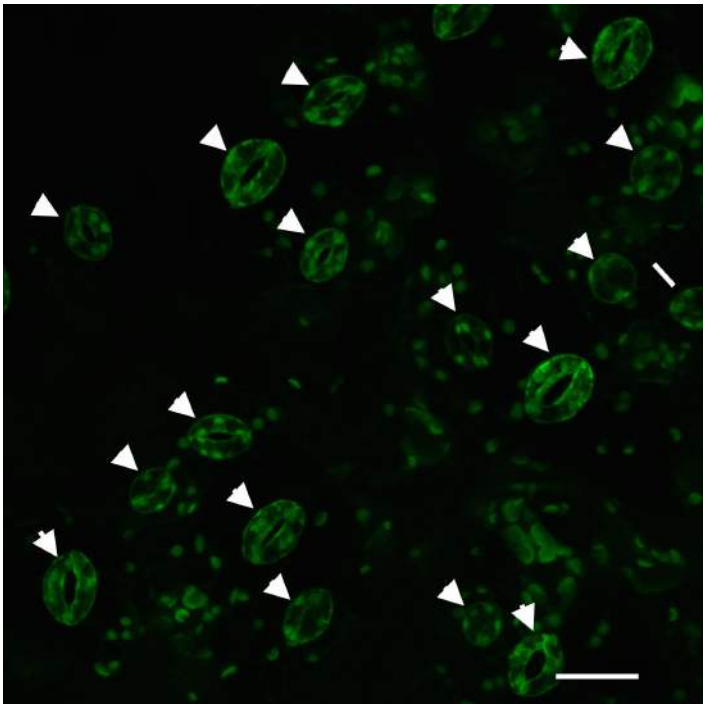

Figure 3.3: Confocal image of fluorescent apk1::gfp labelled stomata. Arrowheads show stomata that are fluorescing. Scale bar = 30 μm

The AFM setup used included an inverted optical microscope (Olympus IX71) but, due to the fact that the dental silicone substrate used to attach the leaves to the microscope slides is opaque, this was unusable. The AFM includes top-view optics for the purposes of setup/calibration and coarse adjustments of sample position. By default the top-view optics uses a white light source but if a light source suitable for fluorescence experiments and the relevant filters were installed it may be possible to use the top view optics as a fluorescent microscope to locate stomata. GFP excitation and emission filters were installed in the relevant positions and apk1::gfp *Arabidopsis* leaves were imaged with the top view optics as shown in Figure 3.4. As can be seen, the image quality for viewing the sample is quite bad and for the purposes of locating stomata, unusable. This is probably due to the fact that the top-view optics were never designed for quality sample imaging. After this it was decided to continue with the original method of scanning the leaf surface in contact mode to locate stomata but increasing the line acquisition rate to 2 or 3 Hz. This resulted in images that did not

track the surface of the leaf very well, but it was still possible to discriminate between cell types and locate stomata.

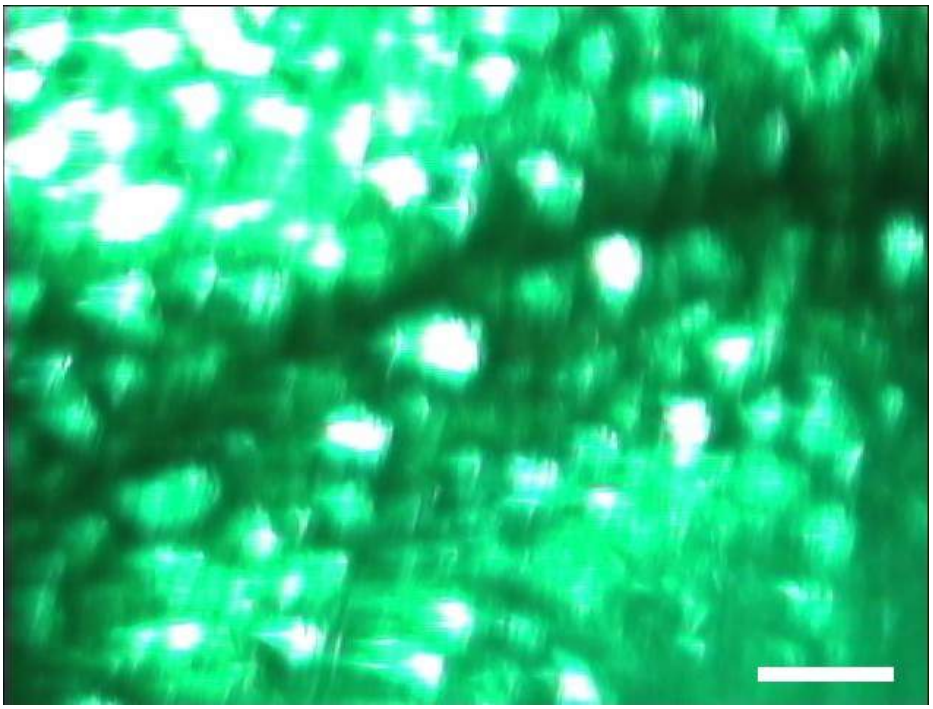

Figure 3.4: The view of the apk1::gfp abaxial leaf surface through the top view optics. The quality of the setup makes it impossible to resolve individual stomata. Scale bar = 200 μm

3.2.4 Optimising Data Analysis

Force maps were collected at 50x50 pixel resolution at a 1 Hz indentation rate using a cantilever of nominal stiffness 0.3 Nm^{-1} (Bruker SNL probes). Force mapping took approximately 40 minutes per map.

Each point on the force map consists of a force indentation curve (Fig. 3.5). Extracting some value for a property from this curve and plotting it on a 50 x 50 grid allows the spatial distribution of this property to be seen. Commonly, properties such as height or adhesion can be extracted but the focus of this work was to investigate the differing mechanical properties of the sample.

The Asylum Research data acquisition and analysis software is very flexible, allowing a researcher with programming skills to write their own data analysis algorithms.

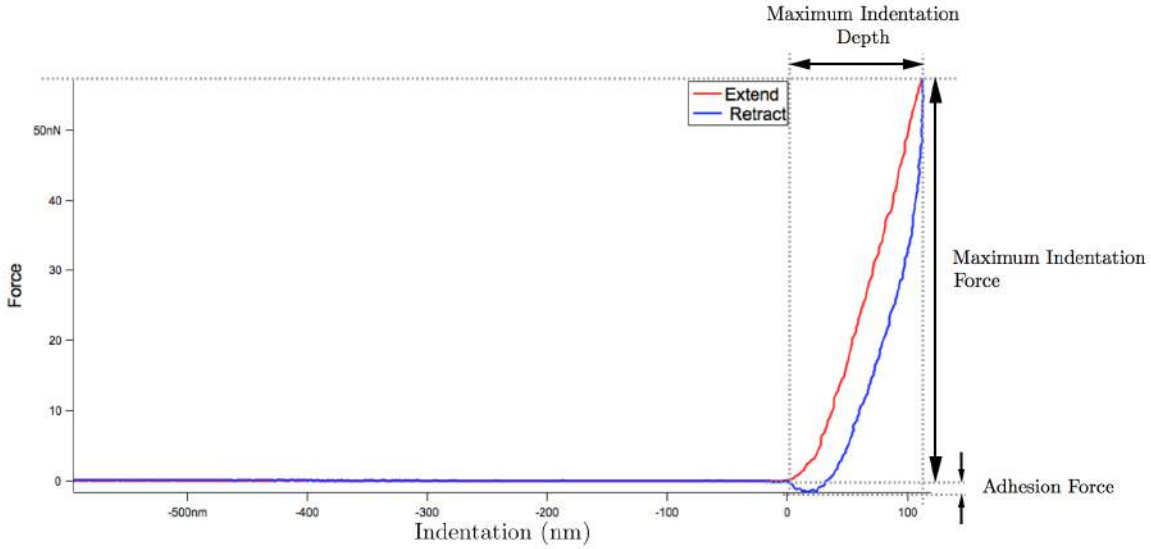

Figure 3.5: A force vs indentation curve taken on plant cell wall. Maximum indentation force, maximum indentation depth and the adhesive force between the tip and the sample are labelled.

Starting with the built in functions for determining stiffness, and after discussions, 3 revisions were made to get more accurate and relevant results.

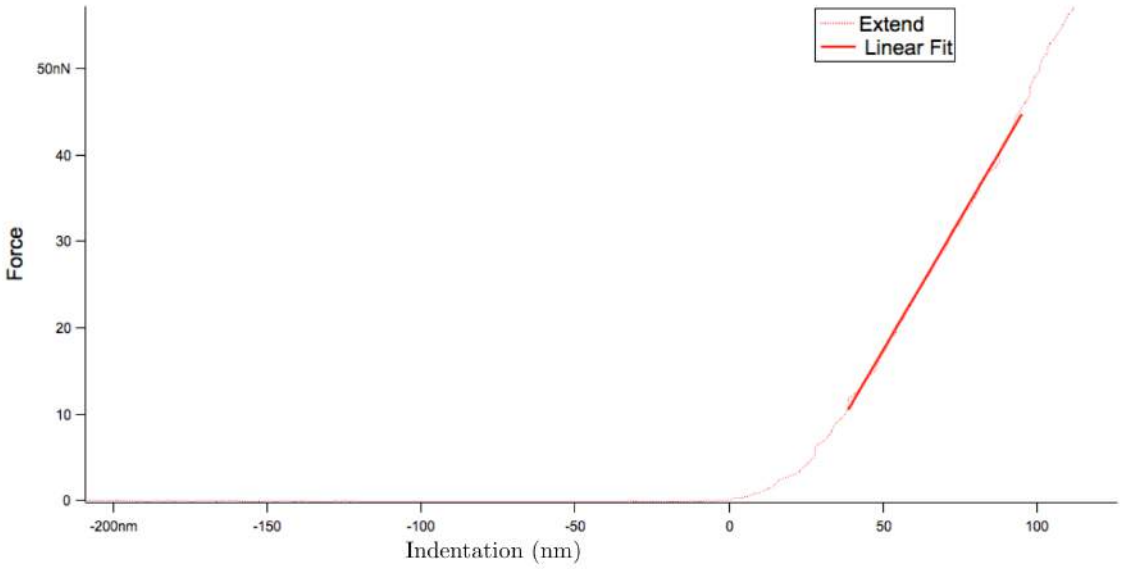

Figure 3.6: A force vs indentation curve taken on plant cell wall. A straight line has been fitted to the contact section of the curve between 20% and 80% of the maximum applied force.

First analysis was performed with the in built function for determining stiffness. This function fits a straight line to the force-indentation data between 20% and 80% of the maximum force and reports the gradient of that line (See Figure 3.6).

Depending on the stiffness of the sample the cantilever will indent to a different depth before reaching the trigger deflection. This means that the values extracted for stiffness using the above methodology were calculated over different indentation depths. To make stiffness comparable it was deemed necessary to measure the stiffness only between a pre-defined indentation depth. Experiments to determine the optimum indentation depth were described in section 2.3.2. From the graph of calculated stiffness versus indentation depth (Figure 2.15), it was seen that stiffness ceased to increase after about 60nm indentation which implies a change from indentation to displacement of the sample.

The process for calculating the stiffness at 30 nm was more complicated that just reporting an average gradient, as it was necessary to determine the point of contact between the tip and the sample. This was accomplished by using a moving window algorithm that runs along the force-indentation data and determines when there is a significant change in gradient, signifying the cantilever has contacted the sample. This point is then defined as zero indentation. The force axis was also offset by calculating the average of the last ten points in the non-contact region of the curve and setting this to zero. Once the data has been offset correctly, the gradient between 10 nm and 30 nm is calculated by fitting a straight line to the data as in Figure 3.7, which shows a straight line that has been fitted to the initial 10 nm- 30 nm of indentation.

As measuring the gradient over a range of indentations would return an average stiffness for indentations between 10 nm and 30 nm, this method was also rejected. As we require the instantaneous stiffness at 30 nm indentation, a third formalism was implemented.

By fitting a 3rd order polynomial curve to the force-indentation data and differentiating it we then have an expression for the gradient (stiffness) for any value of indentation. A 3rd order polynomial was chosen as it gives a good fit to the data and is easily differentiable, allowing the stiffness to be calculated.

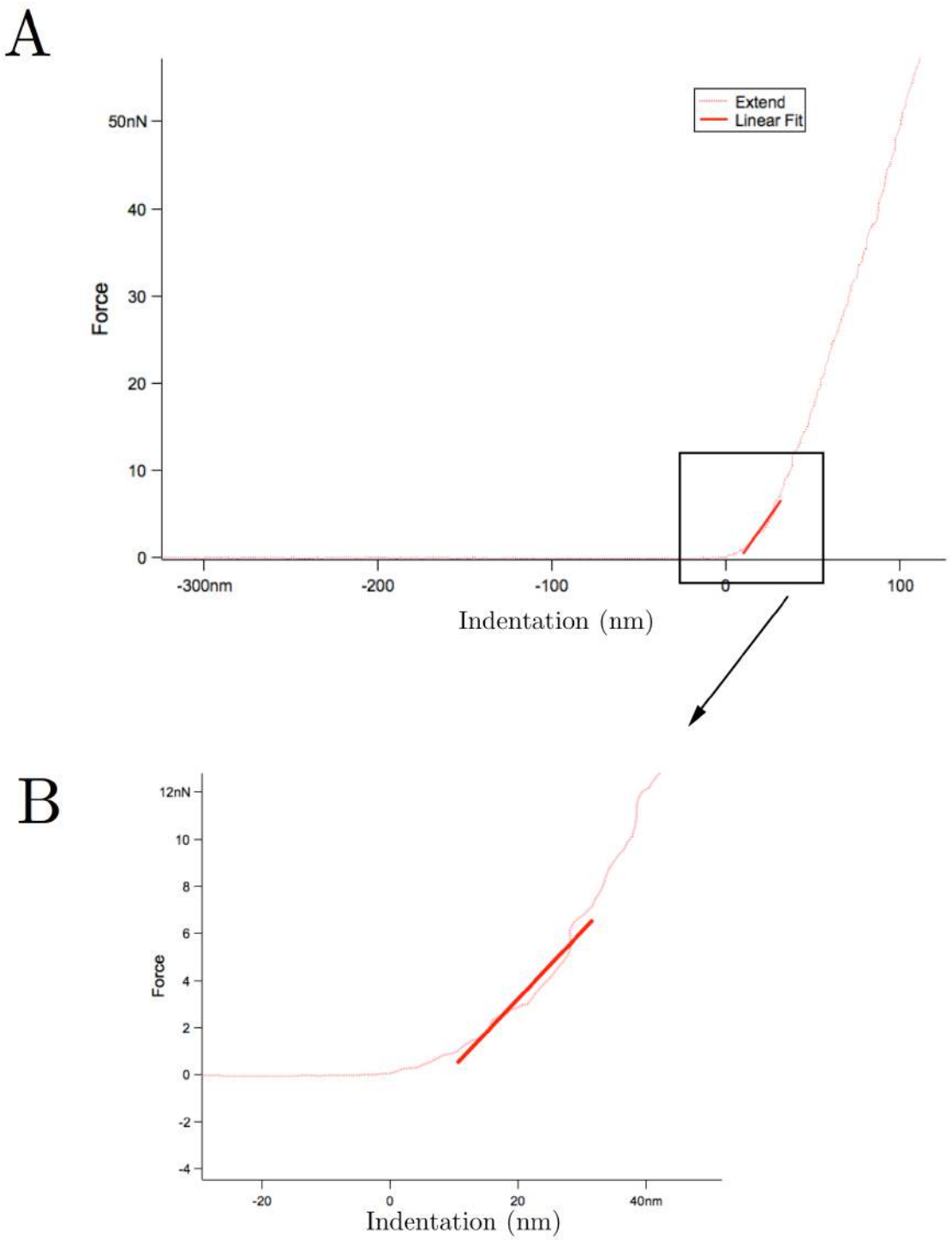

Figure 3.7: A force vs indentation curve taken on plant cell wall. A straight line has been fitted between 10nm and 30nm indentation depth. A, The whole force curve showing the large non-contact area between -300 nm and 0 nm. B, magnification of the area where the straight line was fitted.

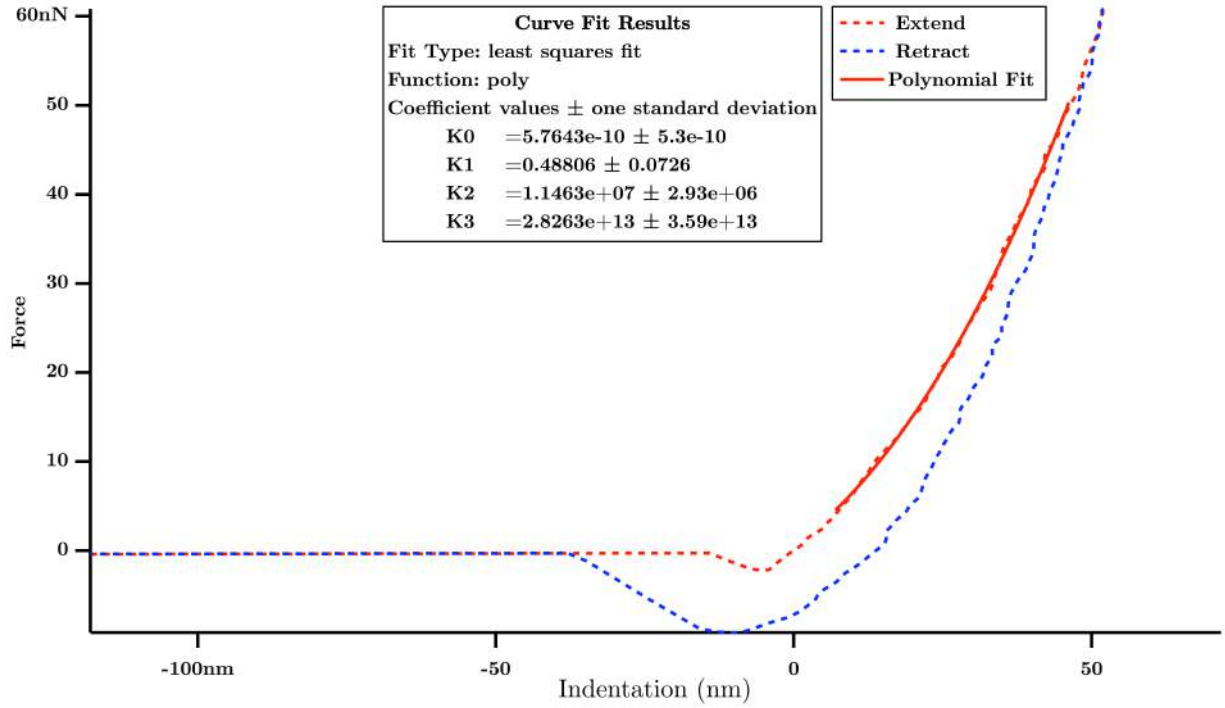

Figure 3.8: A force vs indentation curve taken on plant cell wall. A third order polynomial is fitted to the extend section of the curve (red dotted line). The curve fitting results are shown and correspond to the coefficients in equation 3.2.1.

The third order polynomial and it's derivative have the form:

$$F(\delta) = K_0 + K_1\delta + K_2\delta^2 + K_3\delta^3 \tag{3.2.1}$$

$$k(\delta) = \frac{dF}{d\delta} = K_1 + 2K_2\delta + 3K_3\delta^2 \tag{3.2.2}$$

The data was first offset in the force and indentation axes as described above. A 3rd order polynomial of the form of equation (3.2.1) was fitted to the contact portion of the curve to determine the coefficients K_0, K_1, K_2 and K_3. These were then used in equation (3.2.2) to get an expression for the stiffness in terms of the indentation (δ). The value for stiffness at an indentation of 30 nm was then calculated and used in the construction of stiffness maps. Figure 3.8 shows the contact section of a force indentation curve. The red dotted section is the extend section where the polynomial

was fitted. Values for the coefficients of the polynomial are shown in the box and correspond to the coefficients in equation 3.2.1 and can be used in the differentiated function (equation 3.2.2) to calculate the stiffness.

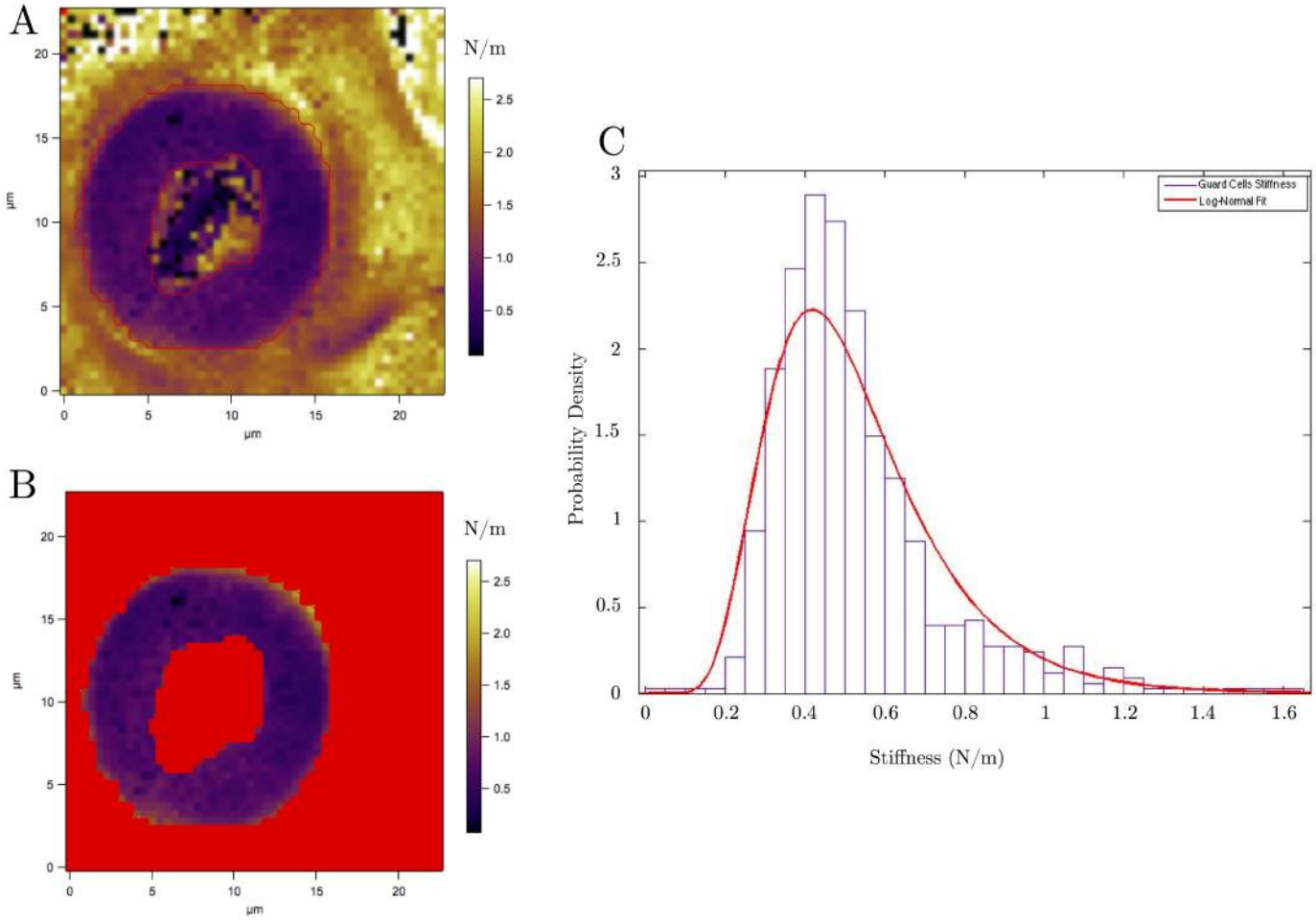

Figure 3.9: A. Stiffness map of a stomate showing the variation in stiffness between the guard cells and the supporting cells. B. The red area shows the area excluded when extracting values used to calculate the guard cells stiffness. C. Histogram of stiffness values from a pair of guard cells. The red line is a fit of a log-normal distribution used to extract the peak or modal value. The modal value for the supporting cells (red area in B) was extracted in the same way

To get a representative stiffness value for the cell wall of a single cell, values were extracted by manually choosing points within cells (Fig. 3.9) for both the guard cells and the supporting cells. A log-normal probability distribution function (PDF, equation 3.2.3) was fitted to histograms of the stiffness data (Fig. 3.9). Again, a log-normal distribution was chosen as this function was a good fit to the data and allowed a representative peak value to be extracted. Log-normal fits returned scale

and shape parameters, μ and σ. These are related to the mean, median, and mode as follows:

$$PDF = \frac{1}{x\sqrt{2\pi}\sigma} e^{-\frac{(ln\ x-\mu)^2}{2\sigma^2}} \tag{3.2.3}$$

$$Mean = e^{\mu+\frac{1}{2}\sigma^2} \tag{3.2.4}$$

$$Median = e^{\mu} \tag{3.2.5}$$

$$Mode = e^{\mu-\sigma^2} \tag{3.2.6}$$

The mode of the stiffness values from the guard cells (k_{GC}) and the supporting cells (k_{SC}) were extracted from each force map and the ratio of the two stiffnesses was used for comparison between samples (stiffness ratio, α);

$$\alpha = \frac{k_{GC}}{k_{SC}} \tag{3.2.7}$$

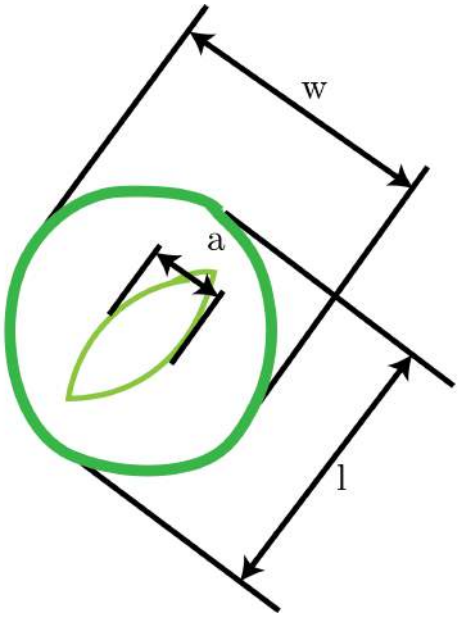

Figure 3.10: A diagram of the measurements made on each stomate, The width and length (w and l) of the guard cell pair as well as the pore width (a) are measured (pore width is measured as in Figure 3.11)

In addition to the mechanical measurements mentioned above the following measure-

ments were also made (Fig. 3.10);

- Stomate width, w
- Stomate length, l
- Pore width, a
- Axis ratio, $\frac{l}{w}$
- Relative pore width, $\frac{a}{w}$
- Stomate surface area, $\frac{\pi}{4}lw$

A value for the pore width was taken by assuming the guard cells had a circular cross-section and measuring the distance between the closest points of the two circles (Figure 3.11B). Taking guard cell cross-sections to be circular is an assumption, as not all guard cells are, but this assumption gives a more accurate value than just measuring from the force maps such as in Figure 3.11A.

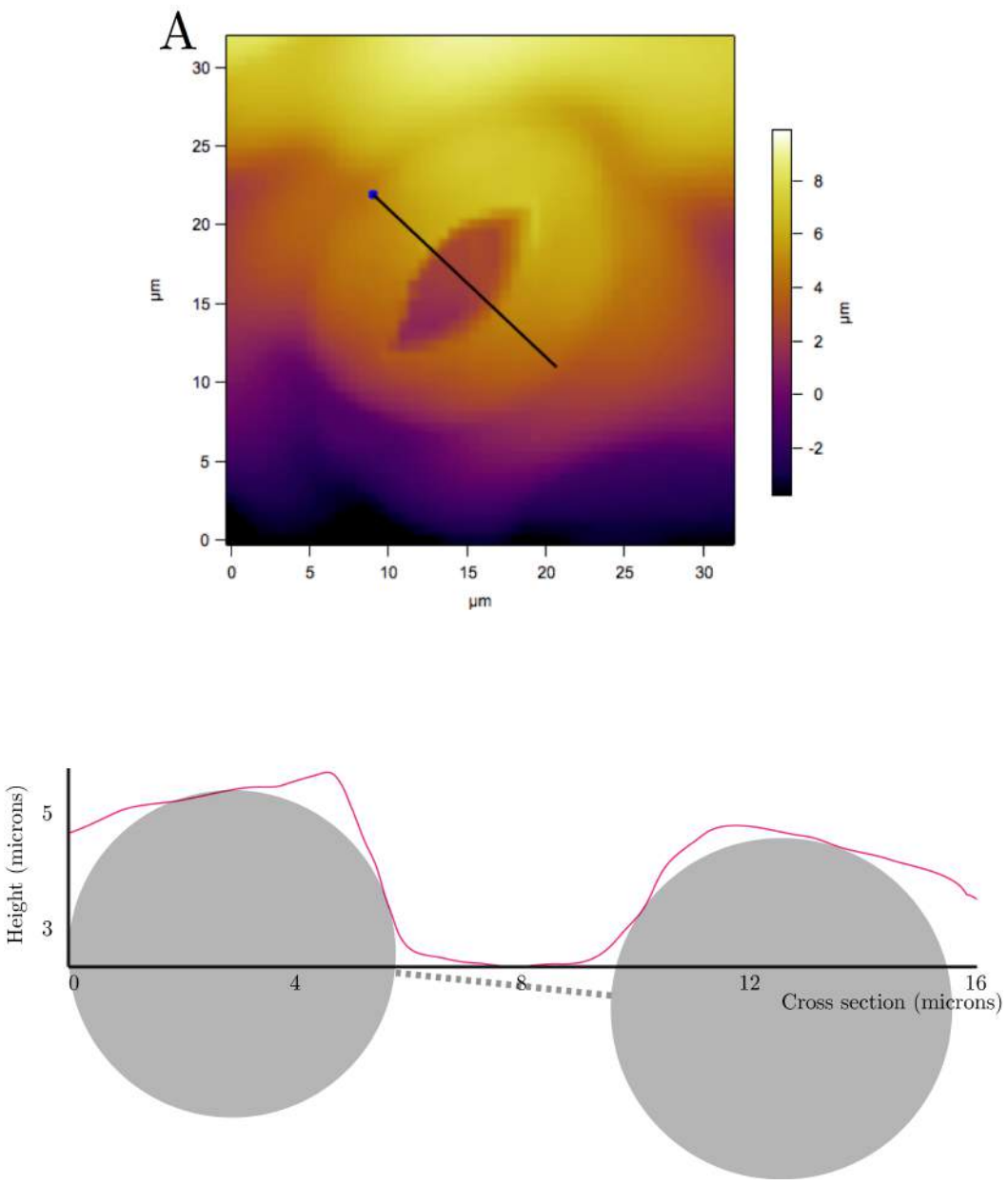

Figure 3.11: Cross section of a stomata showing how a value for the pore width was obtained. A. A force map, showing height data, of a stomate showing the position of the cross section. B. Cross section of the height though a stomate. Circles have been added to represent the guard cell cross section (grey circles), and the pore width has been estimated as the closest distance between the two circles (grey dotted line).

3.3 Results and Discussion

3.3.1 Mechanics of Stomata

Absolute stiffness values for the stomata and their supporting cells varied greatly (Table 3.3). This is mainly due to differences outlined in section 3.2.1. To avoid the effect that measurements on different days with different tips has on the absolute values of stiffness, it was decided to report the stiffness values as a ratio of the mode stiffness of the guard cells relative to the mode stiffness of the supporting cells, such as in equation 3.2.7. This gave a value to the mechanical advantage thought to play a large role in stomatal dynamics and allowed measurements recorded at different times and with different cantilevers to be compared. For example, in table 3.3, stomata 06 and stomata 07 have the same stiffness ratios (to 2 decimal places) but different absolute values for the two different stiffnesses.

Table 3.2 shows the geometrical parameters measured from the stomata. Included are stomate width and length, pore width, axis ratio, relative pore width and stomata area. The smallest stomate had a surface area of 67 μm^2 with a width of 8.33 μm and a length of 10.24 μm. The largest stomate had a surface area of 420 μm^2 with a width of 19.80 μm and a length of 27.05 μm. The axis ratio, a measure of circularity, ranged from around 1 for circular stomata up to 2.01 for long and thin stomata. Relative pore widths varied from 0 for closed stomata up to 0.37 which indicated a pore width of 37% the total stomate width. Errors in the length, width and pore width are related to the pixel size in the force maps.

Table 3.3 shows the mechanical properties measured from the stomata, including modal stiffness of the guard cells, modal stiffness of the supporting cells and the ratio of the two (stiffness ratio). The stiffnesses were calculated using equation 3.2.2 and the modal values were found by fitting log normal distributions to the histograms of these stiffnesses 3.9. Values for absolute guard cell modal stiffness ranged from 0.02 Nm^{-1}

	Stomate Width (μm)	Stomate Length (μm)	Pore Width (μm)	Axis Ratio	Reltive Pore Width	Stomate Area (μm^2)
stomata02	18.80	19.39	1.79	1.03	0.10	286
stomata03	15.20	17.60	0.00	1.16	0.00	210
stomata04	19.10	23.78	0.00	1.24	0.00	356
stomata05	16.00	21.69	0.10	1.36	0.01	272
stomata06	13.60	13.48	0.87	0.99	0.06	143
stomata07	11.50	14.15	0.00	1.23	0.00	127
stomata08	17.30	16.58	3.00	0.96	0.17	225
stomata09	8.33	10.24	0.00	1.23	0.00	67
stomata10	16.40	18.33	1.45	1.12	0.09	236
stomata12	12.30	18.56	0.00	1.51	0.00	179
stomata13	19.90	26.35	1.00	1.32	0.05	411
stomata14	19.80	27.05	1.50	1.37	0.08	420
stomata15	17.30	21.34	5.20	1.23	0.30	289
stomata16	14.30	15.64	0.00	1.09	0.00	175
stomata17	16.90	17.11	0.20	1.01	0.01	227
stomata18	12.30	24.66	0.50	2.01	0.04	238
stomata19	16.10	22.09	1.50	1.37	0.09	279
stomata20	15.40	16.37	0.78	1.06	0.05	197
stomata21	16.20	20.02	1.50	1.24	0.09	254
stomata22	14.50	26.76	1.50	1.85	0.10	304
stomata23	16.00	22.87	3.51	1.43	0.22	287
stomata24	16.50	28.22	1.87	1.71	0.11	365
stomata25	16.20	23.46	3.00	1.45	0.19	298
stomata26	15.60	22.87	0.72	1.47	0.05	280
stomata27	15.70	26.74	1.20	1.70	0.08	329
stomata28	16.20	26.21	5.93	1.62	0.37	333
stomata29	16.20	24.40	2.70	1.51	0.17	310
stomata30	13.80	27.13	0.00	1.97	0.00	294
stomata31	14.55	17.70	1.91	1.22	0.13	202
stomata32	14.07	15.00	0.00	1.07	0.00	165
stomata33	11.95	26.36	0.00	2.21	0.00	247
stomata34	13.99	23.32	0.00	1.67	0.00	256

Table 3.2: Table of the geometrical parameters measured for all the stomata used in this study.

	GC Modal Stiffness (Nm^{-1})	SC Modal Stiffness (Nm^{-1})	Stiffness Ratio
stomata02	0.17	0.24	0.71
stomata03	0.23	0.25	0.92
stomata04	0.36	0.33	1.10
stomata05	0.23	0.32	0.71
stomata06	0.85	0.73	1.16
stomata07	1.26	1.09	1.16
stomata08	0.17	0.12	1.43
stomata09	0.23	0.23	1.02
stomata10	0.44	0.28	1.56
stomata12	0.34	0.30	1.13
stomata13	0.12	0.13	0.94
stomata14	1.11	1.11	1.00
stomata15	0.09	0.09	1.02
stomata16	0.58	1.61	0.36
stomata17	0.42	1.07	0.39
stomata18	0.78	0.83	0.94
stomata19	0.52	0.50	1.05
stomata20	0.28	0.40	0.70
stomata21	0.20	0.20	1.01
stomata22	0.12	0.14	0.86
stomata23	0.16	0.16	0.97
stomata24	0.33	0.27	1.22
stomata25	0.48	0.48	1.00
stomata26	1.32	1.04	1.27
stomata27	1.02	1.14	0.89
stomata28	0.15	0.49	0.30
stomata29	0.88	0.76	1.16
stomata30	0.74	0.79	0.94
stomata31	0.19	0.22	0.86
stomata32	0.25	0.53	0.48
stomata33	0.02	0.02	1.08
stomata34	0.12	0.09	1.31

Table 3.3: Table of the mechanical properties measured for all the stomata used in this study. GC = Guard cell, SC = Supporting Cell

up to 1.32 Nm^{-1}. Values for the supporting cells were over a similar range, from 0.02 Nm^{-1} up to 1.61 Nm^{-1}. The stiffness ratios varied from 0.36, where guard cells were 36% as stiff as their supporting cells up to 1.43, where the guard cells were 143% as stiff as their supporting cells.

Figure 3.12 shows some representative force maps of the stomata that were measured. Each shows the height data (on the left), to give an indication of the topography and the stiffness data (on the right), as calculated by equation 3.2.2.

Figures 3.12B and 3.12D clearly show stomata with a reduced stiffness when compared to their supporting cells, thus figure 3.12B shows cells with a stiffness ratio of 0.36 and Figure 3.12D shows cells with a stiffness ratio of 0.39. The distributions for the stiffness values for stomata 16 are shown in figure 3.13B. These histograms of stiffness and their respective log-normal distribution fits show significantly different peak (modal) values, i.e. the peaks of the green and blue lines are different. These maps were acquired early on during experimentation and spurred interest in continuing research. It should be noted that the data in tables 3.2 and 3.3 are not in chronological order.

Figure 3.12F shows a higher resolution force map of a stomata. The guards cells in this image look to be less stiff than the supporting cells, but due to the automated technique of extracting the stiffnesses this change was not reported in the stiffness ratio, with a stiffness ratio of 1.02 being calculated. This highlights an issue with this method of automated data analysis; the algorithms employed fit log-normal distributions to the stiffness data. If the data cannot be approximated well by a log normal distribution, then the value reported will not be representative of the data. By fitting a log-normal distribution and reporting a modal value as apposed to a mean, it was hoped this would be avoided, but the skewness in the distributions can mean the fitting algorithms can over/under estimate modal values.

Figure 3.12H shows a force map of a stomata where the mechanical properties of the guard cells and supporting cells were very similar (stiffness ratio of 1.16). The

distributions are shown in figure 3.13A. Stomata of this type formed the majority of data collected. The remaining stomata force maps are shown in Appendix B.

The original hypothesis being tested was that guard cells would have differing mechanical properties to their supporting cells. The rationale being that, as stomata were required to change shape to operate effectively, they should be more pliable when compared to the cells that support them. This was seen in experiments performed early on in the project (such as the stomata in Figure 3.12 B and D), but the majority of the stomata measured showed no significant difference between the two types of cells.

To test whether there is a correlation between the stiffness ratio of the stomata and any of the measurements shown on figure 3.10, a multivariate correlation analysis was performed. By comparing each measurement with every other and testing for correlation, any dependence between variables can be examined. Correlations with a p-value of less than 0.01 were deemed statistically significant. The p-values for the correlation analysis are shown in table 3.4 with statistically significant ($p < 0.01$) correlations highlighted in red.

Most of the significant correlations shown in Table 3.4 are trivial, such as stomata width and length correlating with stomata area. Of the correlations that were significant only two related tissue stiffness to an independent stomatal property. These were stomate area against stiffness ratio and relative pore width (pore width/stomate width) against stiffness ratio (guard cell stiffness divided by supporting cell stiffness).

Figure 3.14 shows a graph of relative pore width against stiffness ratio. There is a weak positive correlation (correlation coefficient = 0.36) but the values of stiffness ratio for closed stomata range from 0.36 to 1.09.

One of the problems with comparing data between different stomata is accurately determining their age or developmental stage since this might have an effect on cell wall stiffness. Young stomata would still be growing and their cell walls may be

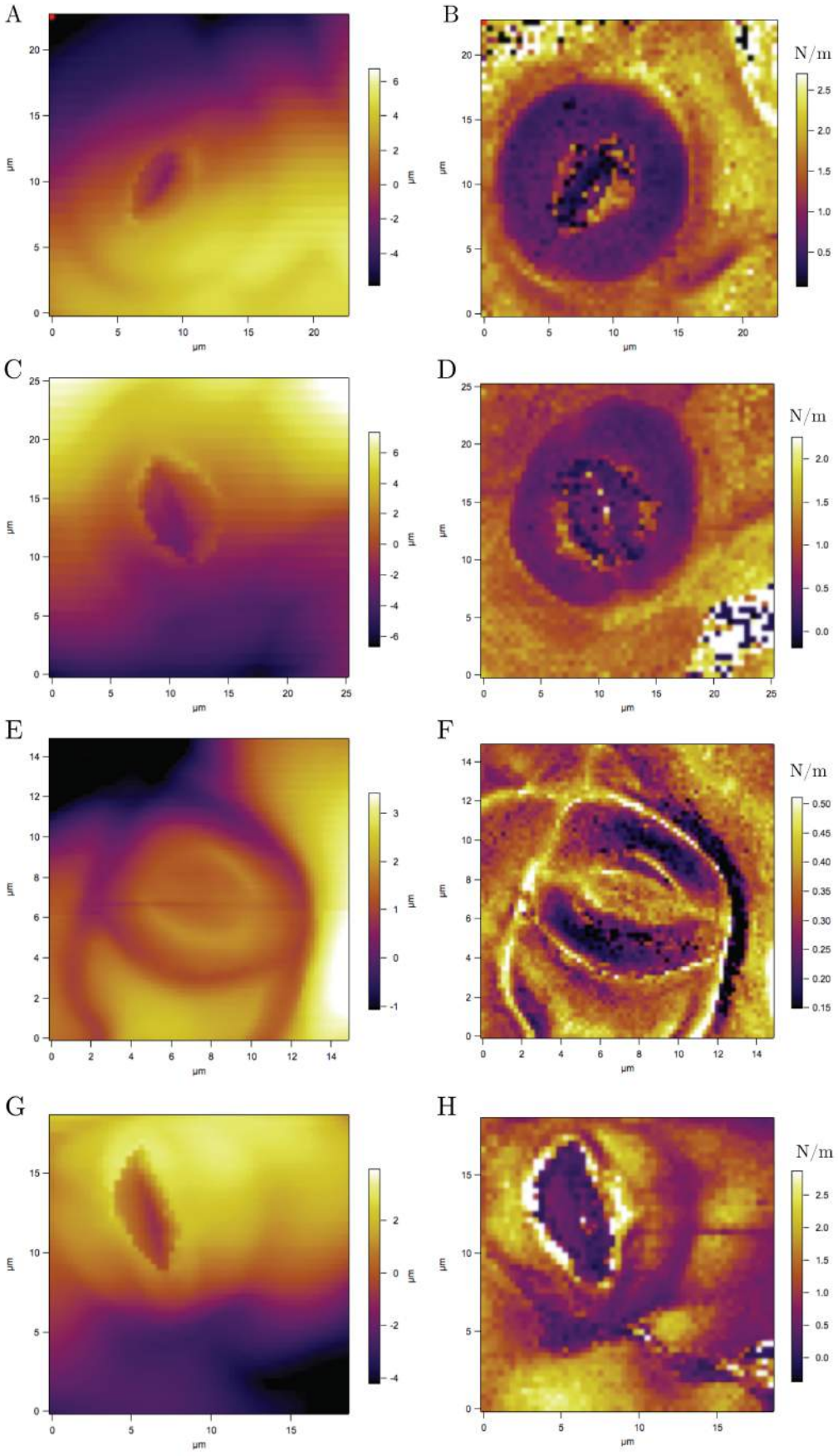

Figure 3.12: Stomata force maps showing height on the left and stiffness on the right. A,B, stomate 16. C,D, stomate 17. E,F, stomate 9. G,H, stomate 6.

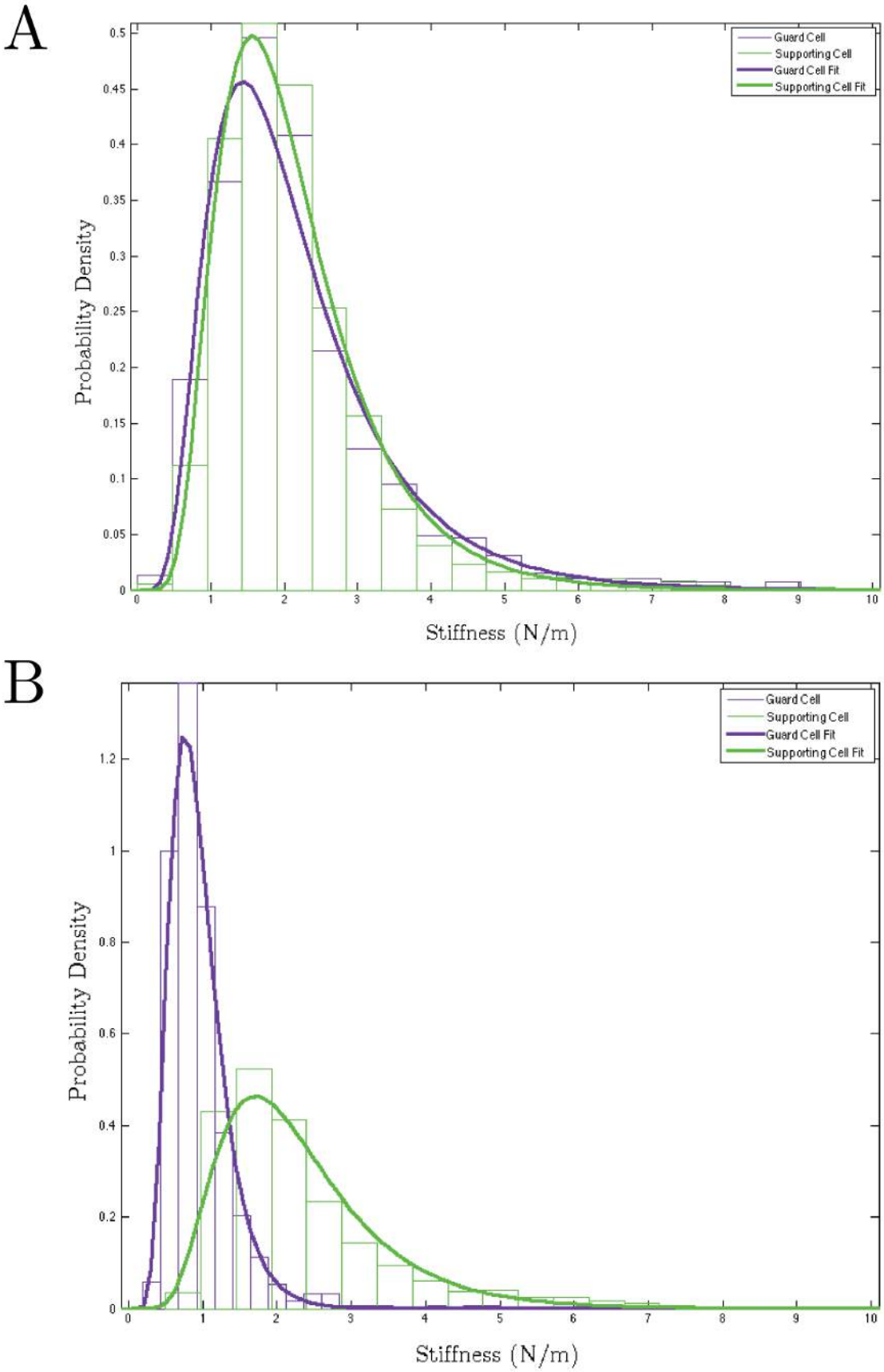

Figure 3.13: Histograms showing the distribution of stiffness values from two stomata force maps. The bars show the data and the lines show the log normal fit. A, Stiffness values for stomata 6. There is no significant difference between the guard cells and the supporting cells. B, Stiffness values for stomata 16. There is a difference between the modal values (peaks) for the guard cells and the supporting cells.

	Stomata Width	Stomata Length	Pore Width	Relative Pore Width	Axis Ratio	Stomata Area	GC Stiffness	SC Stiffness	Stiffness Ratio
Stomata Width	1.00	7.47×10^{-08}	2.79×10^{-04}	7.56×10^{-04}	7.48×10^{-04}	9.45×10^{-10}	0.683	0.359	0.645
Stomata Length	7.47×10^{-08}	1.00	2.34×10^{-03}	1.63×10^{-03}	1.16×10^{-10}	6.41×10^{-14}	0.988	0.828	0.934
Pore Width	2.79×10^{-04}	2.34×10^{-03}	1.00	2.39×10^{-19}	9.60×10^{-02}	2.28×10^{-04}	0.604	0.701	0.868
Relative Pore Width	7.56×10^{-04}	1.63×10^{-03}	2.39×10^{-19}	1.00	3.38×10^{-02}	8.04×10^{-04}	0.465	0.596	8.03×10^{-03}
Axis Ratio	7.48×10^{-04}	1.16×10^{-10}	9.60×10^{-02}	3.38×10^{-02}	1.00	4.80×10^{-05}	0.914	0.863	0.858
Stomata Area	9.45×10^{-10}	6.41×10^{-14}	2.28×10^{-04}	8.04×10^{-04}	4.80×10^{-05}	1.00	0.919	0.593	1.42×10^{-03}
GC Stiffness	0.683	0.988	0.604	0.465	0.914	0.919	1.00	1.06×10^{-08}	0.323
SC Stiffness	0.359	0.828	0.701	0.596	0.863	0.593	1.06×10^{-08}	1.00	9.54×10^{-02}
Stiffness Ratio	0.645	0.934	0.868	8.03×10^{-03}	0.858	1.42×10^{-03}	0.323	9.54×10^{-02}	1.00

Table 3.4: Table of Multi-Variate correlation analysis p-values. Significant values (i.e., values less than 0.01) are coloured red

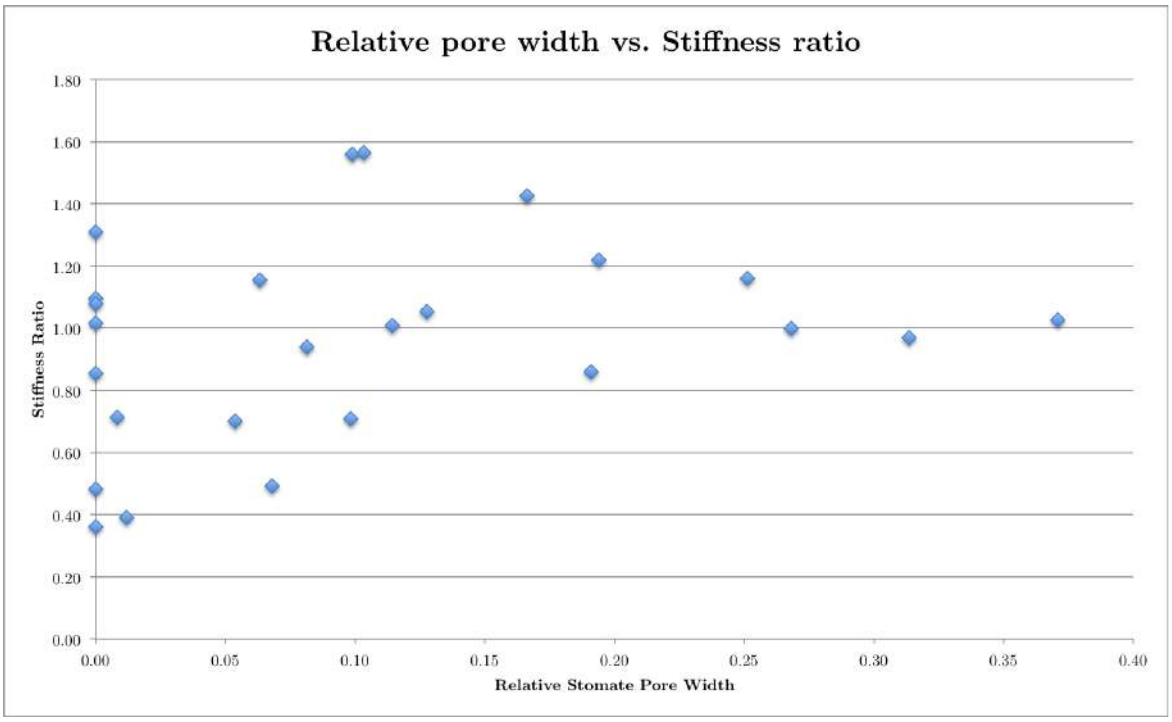

Figure 3.14: A graph of stomatal pore width against stiffness ratio. There is a weak positive correlation.

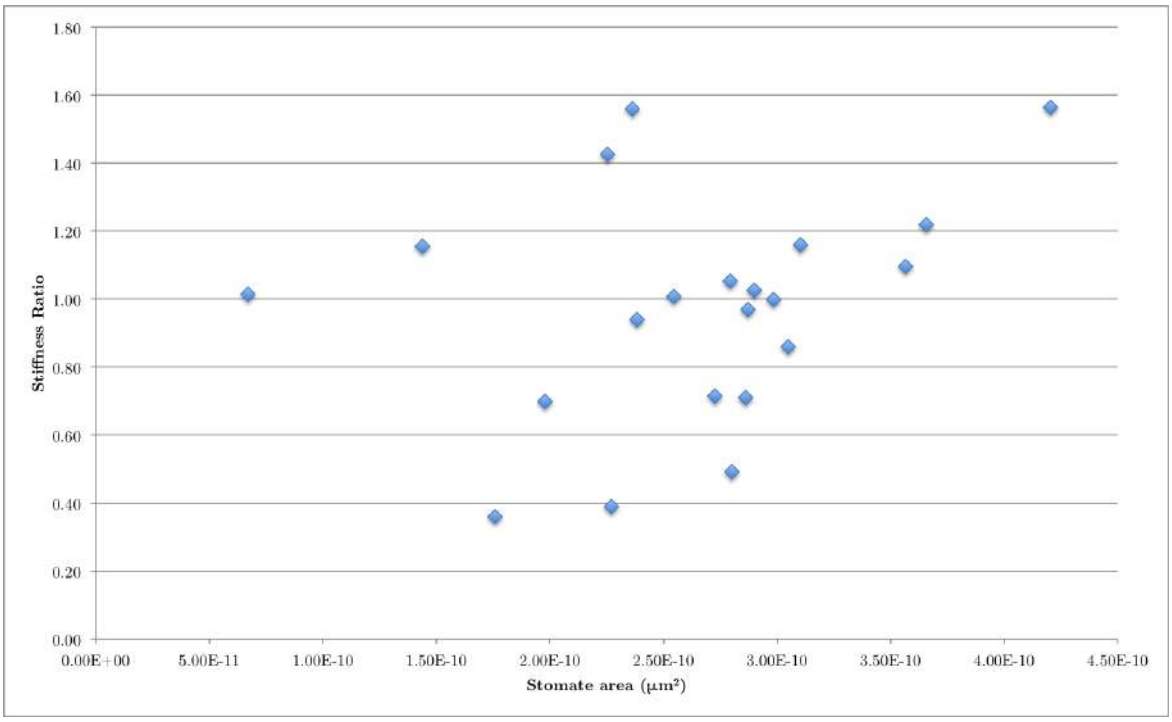

Figure 3.15: A graph of stomata size against stiffness ratio. There is a weak positive correlation.

mechanically different to mature stomata. At the organ level it is relatively simple to pick leaves of the same developmental age, however the stomata on a leaf will be of different ages, due to the fact that they do not all differentiate at the same time. This means that some of the variation seen between stomata (Table 3.3) could be due to the fact that they are at different developmental stages. The size of a stomate can be used as an indication of its age, as can the axis ratio (circularity). Young stomata are likely to be smaller than older stomata and also, young stomata tend to be rounder than older stomata [87]. The stomata used in this study varied in both size and shape, as can be seen both from the values in table 3.2 and in figure 3.16. Comparing the stiffness ratio to the size of the stomate (total guard cell area) (Figure 3.15) there is, again, a slight positive correlation(correlation coefficient = 0.29). The larger the stomate, the higher the stiffness ratio. If we use size as a proxy for age, it could be said that older stomata are stiffer compared to their surrounding cells than younger stomata, having completed their development.

A major issue with force-indentation experiments on any sample is that one needs to understand the surface that is being indented. With an homogenous elastic material, silicone for example, there are many models of indentation that can be used to calculate material properties. When one is indenting a complex composite structure, such as plant cell wall, the resistance to indentation could come from many sources. For example, the pectin that makes up the matrix of the cell wall is relatively soft and gel like [88] and is easily deformed. The cellulose microfibrils embedded within the pectin matrix are highly crystalline [89]. This makes it a lot less deformable and indenting a cellulose microfibril would likely just displace it. These factors make it difficult to put a meaning to the quantity one extracts from a single force-indentation measurement (force curve), but taking a representative value from a number of indentations should average out these effects. It should also be noted that the AFM measures stiffnesses perpendicular to the surface. It is likely that the composite nature of the plant cell wall, the physiology of the cells and the anisotropy of material properties make the

tangential stiffnesses important. Even if these cannot be directly measured, the AFM gives an insight into the local radial stiffness properties of the cell wall. Nonetheless, comparing measurements from AFM experiments to properties obtained by other methods (such as those mentioned in section 1.3) should be done whilst keeping in mind which assumptions each use and the limitations they have.

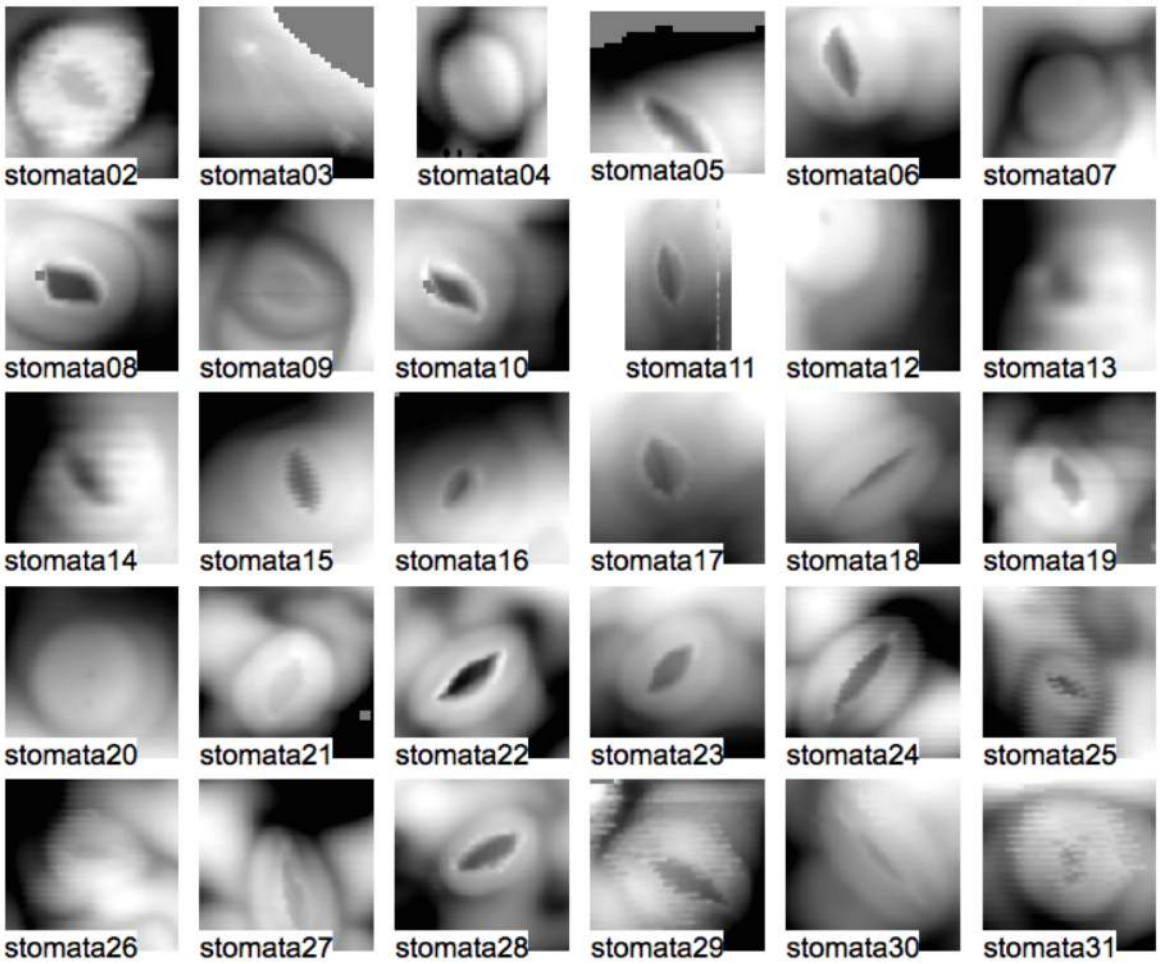

Figure 3.16: Height maps of the stomata used in this study

3.3.2 Capturing the Dynamics of Stomatal Movement

The AFM is a powerful tool for high resolution imaging. In addition to the measurement of mechanical properties outlined above, we also took the opportunity to investigate the dynamics of stomatal action.

While performing measurements with the AFM it is possible to capture images in succession. This allowed us to capture the act of stomata opening and closing in more detail than has been previously achieved. By analysing successive images and measuring the rate of change of the pore width, we were able to calculate opening and closing velocities and match these with previously reported research.

A 10μM solution of ABA with water was used to induce stomatal closing via endogenous signalling. As an alternative, we also used a mannitol solution to force stomata closure by altering the osmotic potential of the media. In the case of mannitol treatment, a 0.5 M solution in water was used.

Leaves were first imaged in water to locate a pair of guard cells. Once a stomate was located the imaging media was changed to a solution of abscisic acid or mannitol, or back to water if the cells had been previously imaged in solution. Consecutive contact mode images were taken at a rate of 2-4 minutes per image (Figure 3.18).

Only two stomata were imaged in this way, as it proved challenging to locate the same stomate after changing the bathing solution.

In the case of the closing stomate (Figure 3.17), guard cells were first located in water. Once located the bathing solution was changed to ABA and the stomata closed. Due to the dynamic nature of the morphology, it was only possible to keep the stomata in frame for around 40 minutes. In this time, the aperture width decreased from 6.1 μm to 4.6 μm with an average speed of 38.4 nm min^{-1}.

For the second stomate that was imaged (Figure 3.18), the guard cells were located in a solution of mannitol. Once located, the bathing solution was changed to water and

the stomata began to open. Again, due to the dynamic nature of the morphology it was only possible to keep this stomate in frame for around 25 minutes. In this time, the aperture width increased from 1.8 μm to 3.6 μm with an average speed of 72.5 nm min^{-1}.

Figure 3.19 shows the change of the stomatal pore size over time for the two cases described above. The red points are for the closing stomata (Figure 3.17) and the blue points are for the opening stomata (Figure 3.18).

These values of opening and closing speeds correspond with results published in the literature. Research performed by Zelitch [90] reported closing speeds of between 20 nm min^{-1} and 30 nm min^{-1} through the action of different biochemicals. More recent research by Wang *et al* [91] investigated light induced stomatal opening and measured apertures after 30 mins of exposure to white light. They measured an average of a 1.5 μm change in aperture over a half hour period, which corresponds to an opening speed of 50 nm min^{-1}. These values are all in the same range and offer validity to the results reported here.

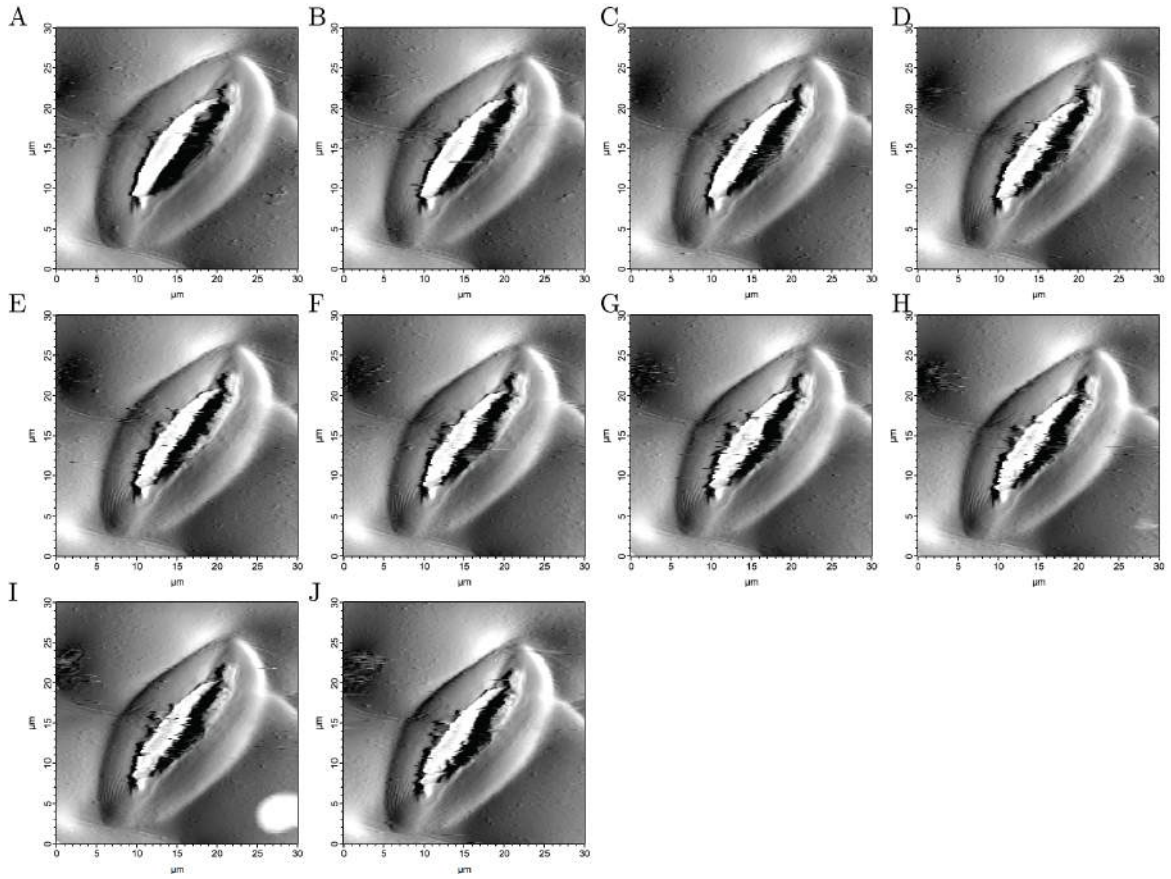

Figure 3.17: A stomate closing after having the bathing solution has been changed to mannitol. The scan size is 30 μm x 30 μm. The time between each images is 1 mins 57 s, running from A - J

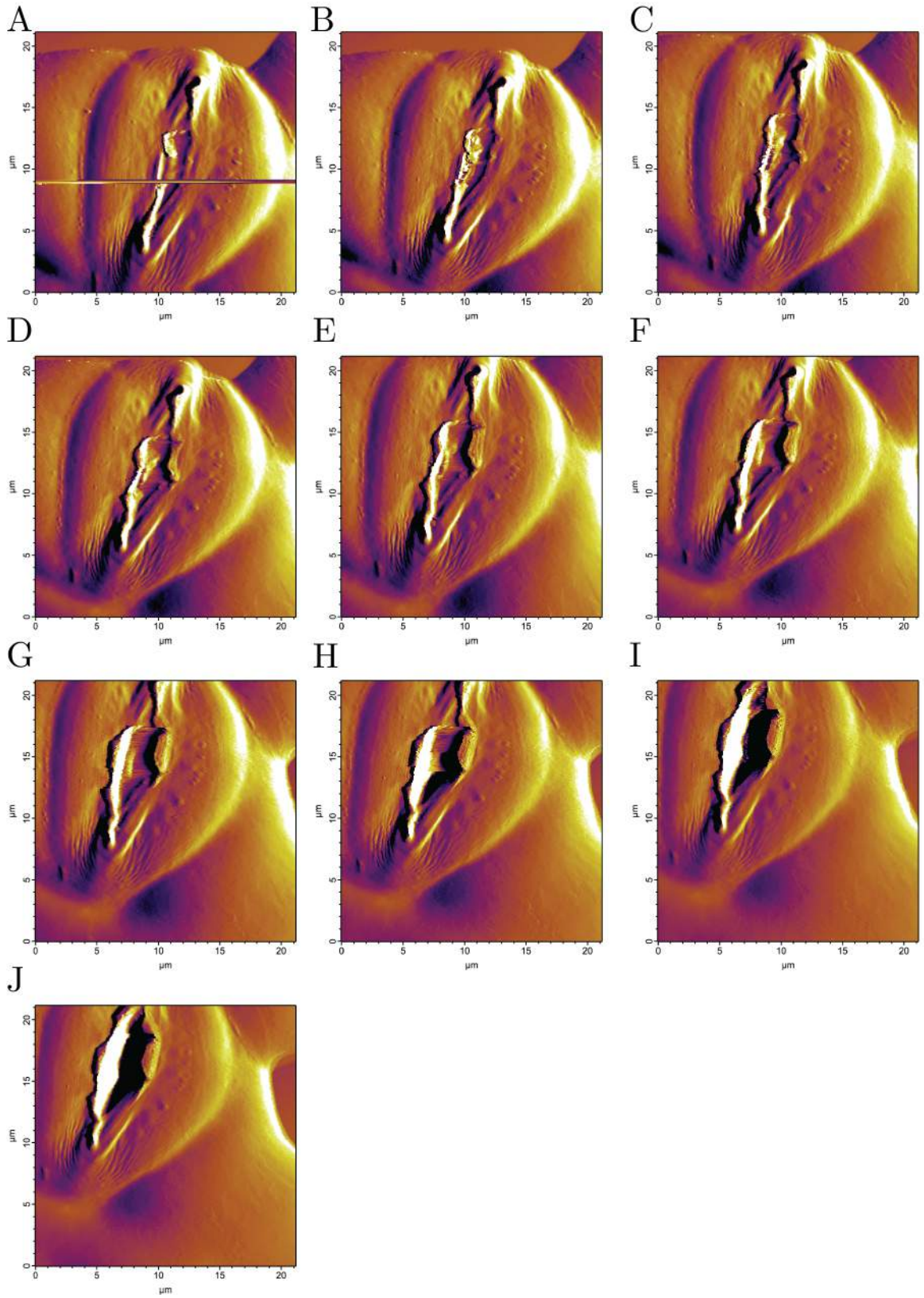

Figure 3.18: A stomate opening after having been returned to water from a solution of mannitol. The scan size is 22 μm x 22 μm. The time between each images is 2 mins 51 s, running from A - J

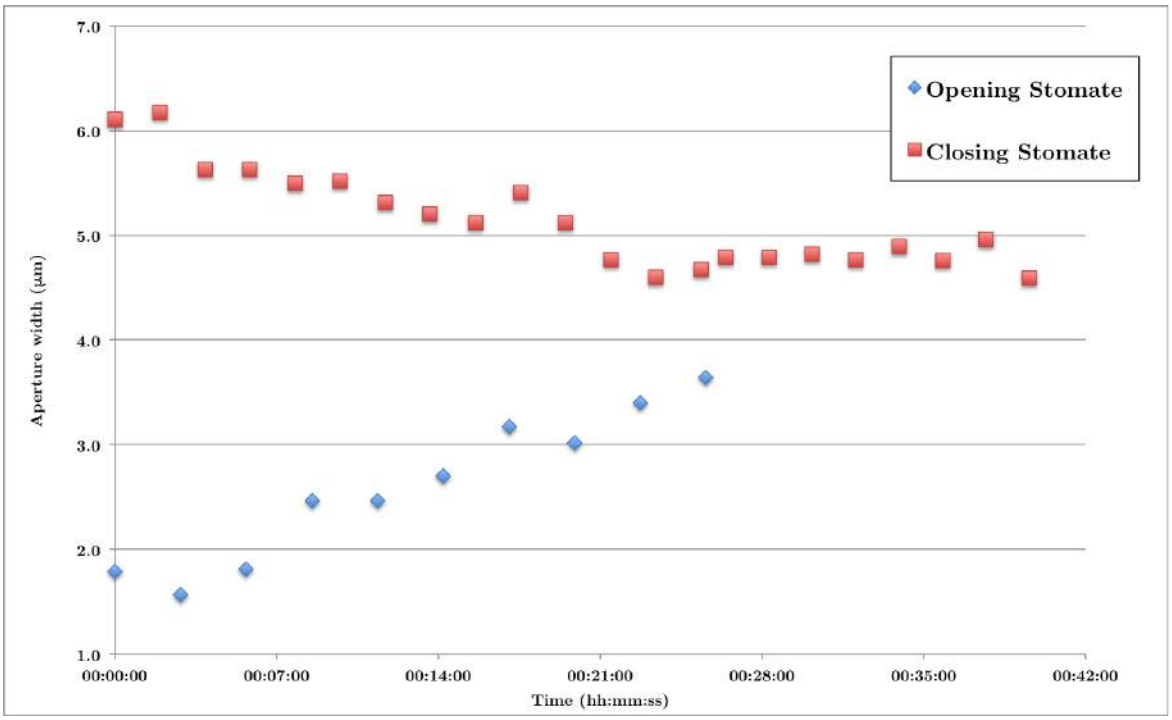

Figure 3.19: Graph of stomata pore size versus time. In the case of the closing stomate (red points), ABA was applied at the minus 10 minute time point. In the case of the opening stomate, the solution was applied at the minus 4 minute time point.

3.3.3 Stomatal Buckling

Compared to other methods of microscopy, AFM offers high resolution 3D images of the surface of samples. As discussed in section 3.1, the plasma membrane has been shown to change surface area during stomatal opening/closing. Due to the fact that the cell wall surface cannot undergo endocytosis in the same way as the plasma membrane, there must be some deformation of the cell wall to account for this area change as no cell wall material is being removed.

During the measurement of stomatal dynamics, as outlined in section 3.3.2, it was noticed that the walls of guard cells buckle and ridges form as stomata close (Figure 3.20). This buckling was only noticed when looking at the dynamics of stomata, as when performing the mechanical measurements, stomata were imaged quickly and at low resolution and the force mapping was again performed at low resolution. Buckling events were often located around the area where the two guard cells joined, and were always parallel to the circumference of the stomata. In the images of the stomate

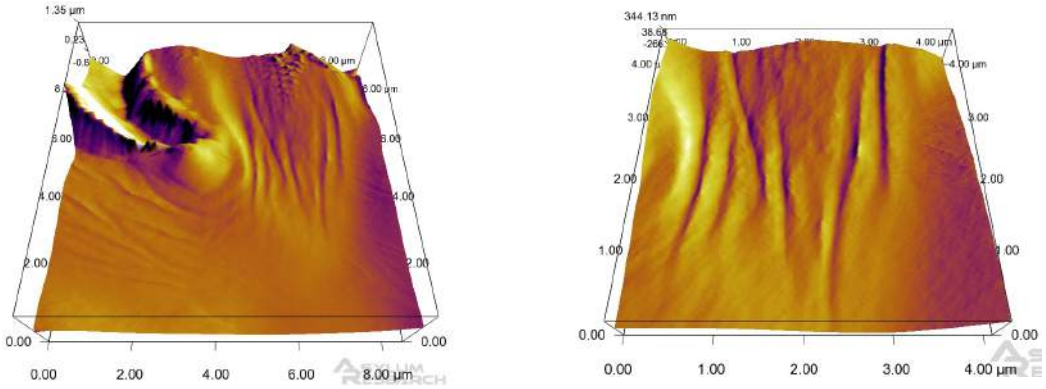

(a) (b)

Figure 3.20: 3D renders of AFM height images of an area of guard cell where stomatal buckling is evident. (a) Overview of the area of interest, just beneath the stomatal pore. (b) Higher resolution image of the area of buckling.

shown (Fig. 3.20) the ridges of the buckling are around 300 nm wide and 25 nm high.

This could be direct evidence of the cell wall responding to changes in plasma membrane reorganisation underneath itself or to the pressure changes within the cell. Of course this is merely circumstantial and further work is needed, but it opens the door to research that could focus on the dynamic morphology of guard cells at such a level of detail. If confirmed, the data would indicate that the guard cells do not simply act in an elastic fashion during opening and closing of the stomates, rather the stresses built up within the cell wall during change in cell volume are at least partially relieved by buckling events. This would imply that the structure of the cell wall must allow such reversible buckling to occur.

3.4 Conclusions

In this chapter I described a series of experiments performed on *Arabidopsis thaliana* stomatal cells. This carried on from preliminary work described in chapter 2 to develop a robust technique for measuring plant cell mechanics with the AFM.

To further validate AFM as a method of measuring plant cellular mechanical properties, the methods of sample preparation and their effect on cell viability was investigated. A common method of testing plant cell viability is with an fluorescein diacetate (FDA) stain. In live cells FDA is hydrolysed and broken down in to fluorescein, which fluoresces green under ultraviolet light. To test whether the mounting media that was used had an effect on the viability of the sample, leaves were prepared as if they were being used for AFM measurements and the fluorescence was viewed after 40 minutes, a typical amount of time for AFM experimentation. The majority of samples expressed a similar amount of localised fluorescein fluorescence as leaves that had not undergone the preparation technique and the methods were deemed suitable.

During experimentation it became evident that the built in analysis algorithms for extracting mechanical measurements from force curves would not be suitable for this work. Custom analysis code was developed and used for this analysis (see Appendix A). Three methods were used, one to extract the average stiffness over the entire variable indentation, a second to extract the average stiffness over a set indentation range and a third to extract the instantaneous stiffness at a set indentation. These three formalisms were applied to the guard cells and supporting cells and a representative value for each was extracted. These values were used to construct a metric comparing the stiffness of the two cell types (stiffness ratio). A multivariate analysis was performed with the other geometrical measurements collected from the stomata and significant correlations were discussed.

Multivariate analysis highlighted that stiffness ratio of guard cells to supporting cells correlated with stomatal size and stomatal relative pore width, with smaller stomata

and stomata with a smaller relative pore width having a lower stiffness ratio. The fact that stomata which are more widely open, relative to their width, are stiffer when compared to their supporting cells also makes sense intuitively. The fact that the turgor pressure is higher in these cells, compared to the supporting cells, means a tension is being applied to the cell wall. This tension could be registered as a higher stiffness in a non-linear elastic material, which the plant cell wall is assumed to be. This tension-stiffening effect has been recorded in other systems before, such as dividing eukaryotic cells [92] and is thought to be crucial for the growth and division of plant cells [93].

During measurement, a putative buckling effect was noticed on guard cells as they closed. According to research performed by Meckel *et al* [85], guard cells change volume and surface area during opening and closing. This change of size was shown to be due to the endo/exocytosis of the plasma membrane. Due to the fact that the cell wall cannot undergo changes at the same rate as the plasma membrane, any extra material in the cell wall would have to bunch up to accommodate the changes of the membrane beneath. Further work is being carried out to investigate these buckling events in more detail.

In the next chapter I will describe work carried out on a separate part of this project to further develop a model of morphogen dynamics in the leaf margin to include details of auxin importers and their role in forming leaf shape.

Chapter 4

Modelling Auxin Transport in the Leaf Perimeter and its Role in Differential growth

4.1 Introduction

The group of hormones known as auxins are thought to be involved in nearly all areas of plant development and cell growth, from guiding root development underground, to initiating leaf primordia above ground. The most common form of auxin in plants is indole-3-acetic acid (IAA) and any mention of auxin in this thesis will refer to this specific type. Auxin diffuses freely within cells and passively permeates the cell membrane and wall via diffusion. Auxin is also actively transported by certain membrane bound transporter proteins. These to processes lead to the formation spatial gradients and patterns in tissues that are thought to drive cell growth and differentiation.

Local differential growth leads to change of shape (morphogenesis) and a significant body of evidence indicates that this is driven by the formation of auxin gradients and maxima in tissues. For such maxima to form auxin must be transported against the

diffusion gradient and research has identified an active transport process, termed Polar Auxin Transport (PAT) which enables the formation of such maxima. This is accomplished by the localised deployment of a family of auxin efflux transporters, known as the pin-formed proteins (PINs). Work on auxin transporters has, so far, mainly focused on these efflux transporters, but evidence is emerging that, to create complex patterns of auxin concentration, influx importers must be considered as well.

PIN1 is a polar auxin efflux transporter, it acts to transport auxin from areas of low concentration to areas of high concentration. Visualising the wall on which PIN1 is localised can show where auxin is being transported and show areas of higher auxin concentration [16]. CUC2 allows PIN1 to localise preferentially to certain cell walls; in CUC2 mutants leaves formed smooth margins [94]. CUC2 maxima form in the sinuses between serrations and are thought to retard growth [95].

As well as the PIN family of efflux transporters there are a group of influx transporters called the auxin and auxin-like transporters (AUX/LAX) [96]. It is thought that the differential expression of these transporters is the key mechanism that forms serrations in the *Arabidopsis* leaf margin. The object of this chapter is to employ mathematical descriptions of auxin transport in the leaf margin and to model the effects the differential expression of these transporter proteins has on serration formation in the leaf margin.

Research performed by Smith *et al* [97] used conceptual models of auxin transport by PIN proteins to recreate the patterns generated during spiral phyllotaxis in *Arabidopsis*. Their model used competing mechanisms of active transport and diffusion to create local peaks of auxin which lead to organ outgrowth. Their model was able to reproduce, within the standard error, the divergence angles within the shoot apical meristem of *Arabidopsis*.

Carrying on from this work, Bilsborough *et al* [98] applied the rules developed for the model of phyllotaxis to the development of the leaf margin. Their model was able

to reproduce the local outgrowths seen in *Arabidopsis* leaves, but the positioning and timing of the outgrowth formation did not match with what is seen in the plants.

Using this as a starting point, we aimed to recreate this model, with the addition of a family of auxin efflux transporters (AUX/LAX proteins) shown to be important in leaf development.

4.2 Expression Patterns

All of the experimental work in this section and section 4.3 was carried out by Ania Kasprewska [99] and provides the data against which the computational model is refined and tested.

To investigate the functional significance of the AUX1/LAX family of auxin transport proteins in leaf morphogenesis a GUS reporter construct [100] fused to the controlling promoter elements for each protein of interest was used to visualise the spatio-temporal expression of certain auxin transporters during early leaf development. The three members of this family analysed were AUX1, LAX1 and LAX2. A fourth and final member of this family of genes, LAX3, is never expressed in the leaf and so was excluded from this study. By looking at the expression patterns of these transporters we can build up a model of how they work together to transport auxin and form patterns that guide the timing and position of serrations in the leaf margin.

Beginning with LAX1 expression, the earliest visible GUS signal was located in a group of cells at the tip of the leaf (Figure 4.1 A). This maxima, formed in the meristem prior to primordia emergence [101], is present throughout the development of the leaf. Later (Figure 4.1 B), two peaks form at the edge of the leaf just below the midpoint between the base of the leaf and the tip. At later stages, new symmetrical regions of LAX1 expression appear below the original sites, closer to the base of the leaf. The older regions of LAX1 expression are observed to now be at the tips of local outgrowths

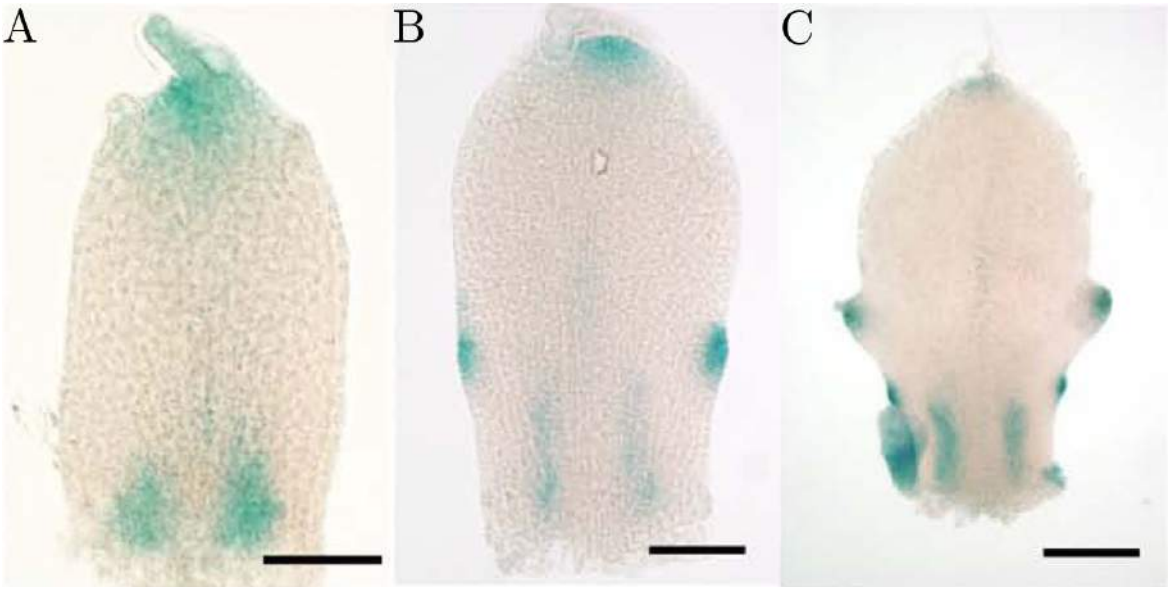

Figure 4.1: Gus expression of the LAX1 auxin importer during leaf development. A, Early leaf. B, Mid Leaf. C, Late leaf. Signal is observed as blue colouration. Scale bars A. 50μm B. 100μm C. 200μm [99]

(Fig. 4.1 C).

In contrast, as shown in figure 4.2, LAX2 expression was limited to the interior of the leaf. At the earliest stage expression was contained to the distal half of the leaf interior (Figure 4.2 A). In later stages (Figure 4.2 B,C), expression appears more towards the base of the leaf, but never lower than the newest peak of LAX1 on the margin (Fig. 4.2) (Compare to figure 4.1). LAX2 expression was always excluded from the outer layer of cells and at later stages it started to resemble the complicated network structure of the developing leaf vasculature system (Figure 4.2 C).

The expression of the third auxin influx protein analysed in this study, AUX1, was limited to the margin throughout all stages of development (Fig. 4.3 A, B, C)

The patterns of auxin transporters provide inferences on where auxin might accumulate within a tissue. Direct visualisation of auxin in tissue is extremely difficult but an indirect assessment of auxin levels can be made using a specific reporter gene called DR5 [102]. As shown in figure 4.4 A, in early stage primordia there is a peak of auxin activity at the tip of the leaf. As the leaf develops, peaks of expression appear at points along the margin preceding serration formation (Fig. 4.4 B,C). There is also

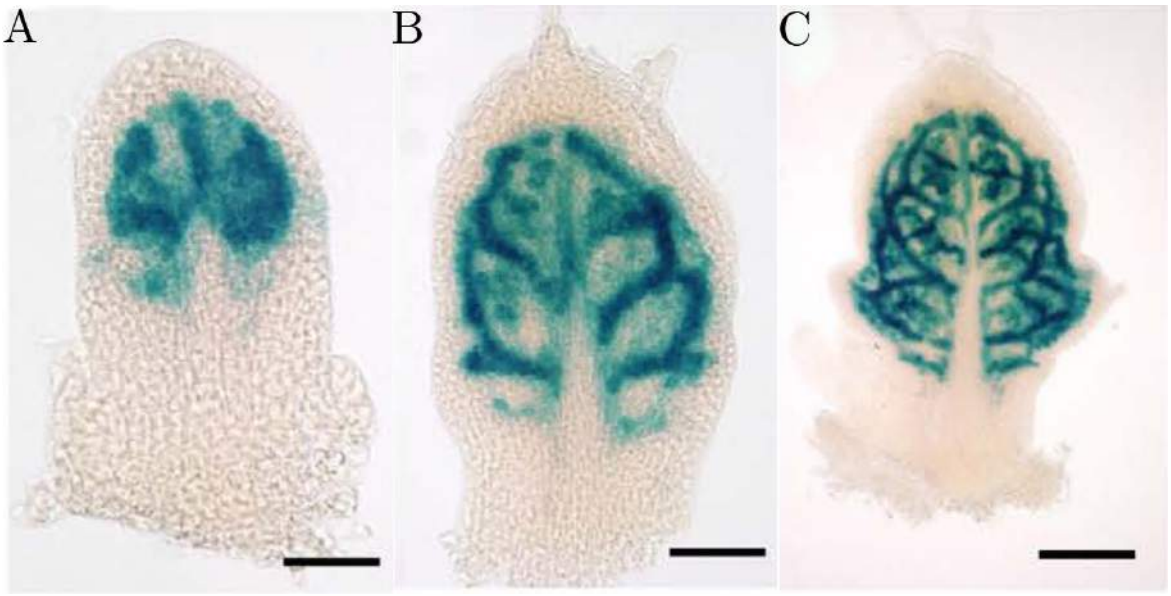

Figure 4.2: Gus expression of LAX2 auxin importer. A, Early leaf. B, Mid Leaf. C, Late leaf. Signal is observed as blue colouration. Scale bars A. 50μm B. 100μm C. 200μm [99]

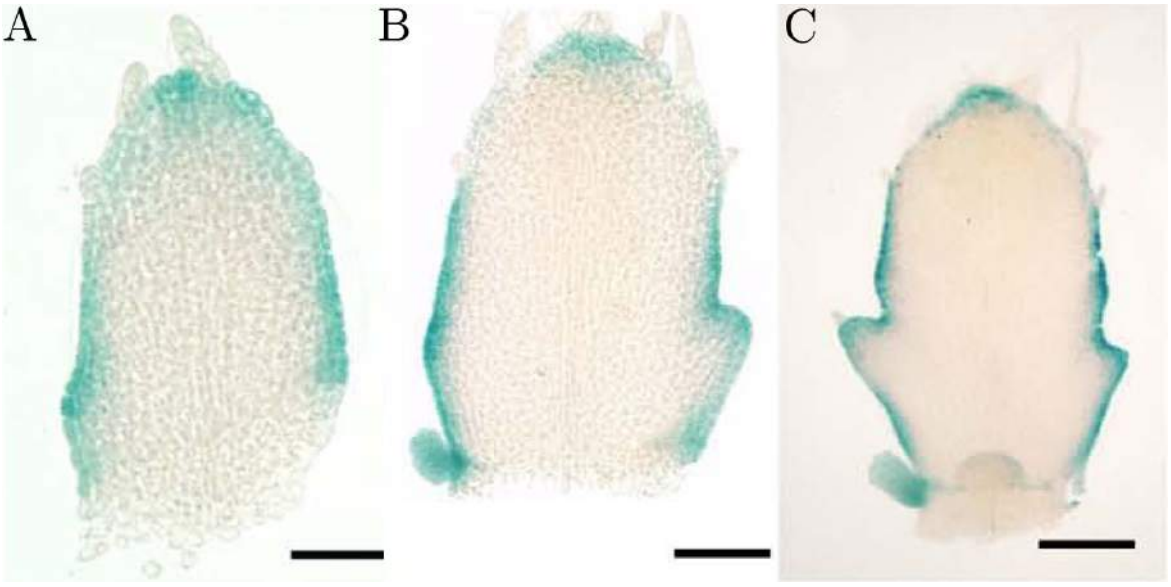

Figure 4.3: Gus expression of AUX1 auxin importer. A, Early leaf. B, Mid Leaf. C, Late leaf. Signal is observed as blue colouration. Scale bars A. 50μm B. 100μm C. 200μm [99]

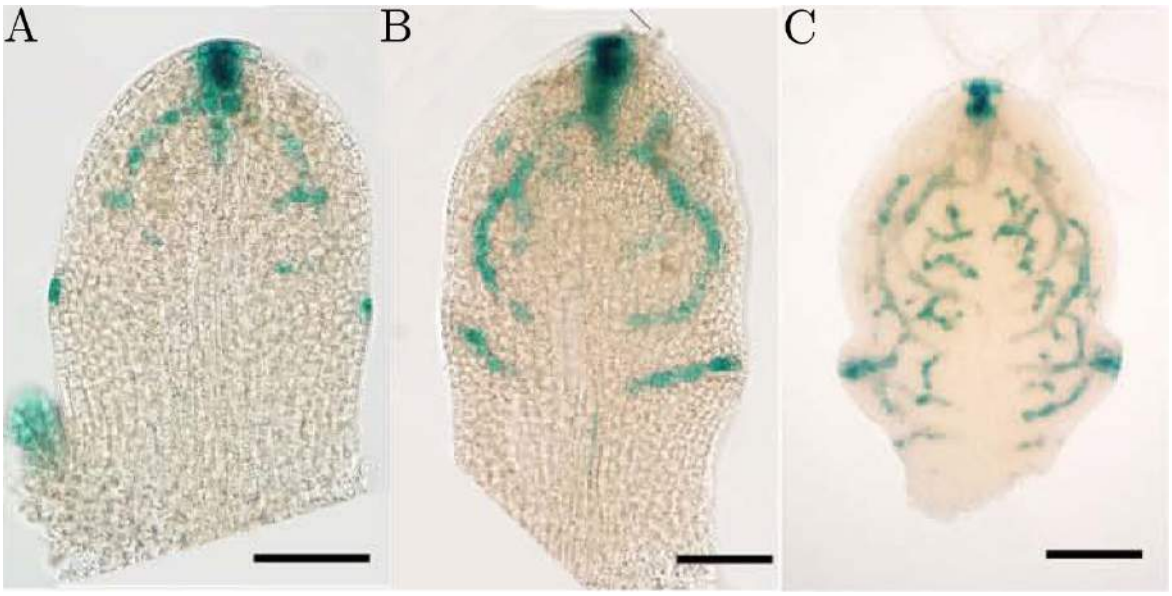

Figure 4.4: Gus expression of DR5 auxin importer. A, Early leaf. B, Mid Leaf. C, Late leaf. Signal is observed as blue coloration. Scale bars A. 50μm B. 100μm C. 200μm [99]

a complex pattern of DR5 expression visible in the interior of the leaf, presumably guiding the formation of the vasculature system.

4.3 Mutant Phenotypes

By knocking out one, two or all three of the auxin influx transporters described in the previous section we can get an idea as to their function and the effect they have on the shape of the developing leaf.

In the wild type (WT) leaf the primordia were initially smooth (Fig. 4.5 A). In later developmental stages (Fig. 4.5 B), serrations appeared towards the leaf base and as the leaf grew further, more serrations formed proximal to the initial ones (Fig. 4.5 C). As the main body of the leaf is growing, these secondary serrations were less pronounced than the initial ones [75].

Using genetic techniques, plants in which each of the AUX1, LAX1 or LAX2 genes was mutated were created [99], as well as plants in which all possible combinations of mutations (including a triple knockout mutation) were present. In single and double

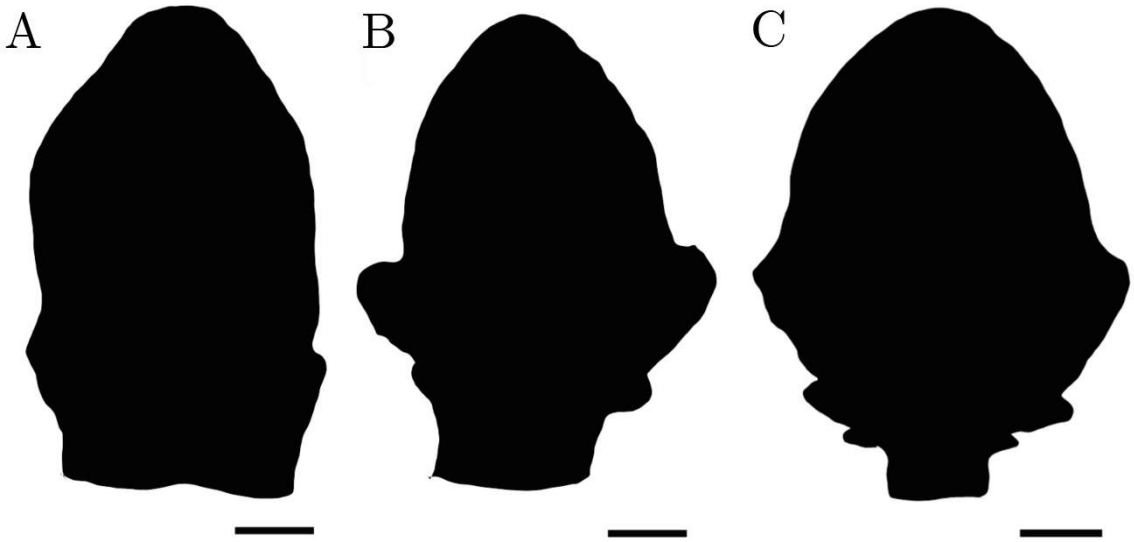

Figure 4.5: Silhouettes of wild type Arabidopsis leaves for three developmental stages. A, Early stage. B, Mid stage. C, Late stage. Scale bar = A, 50 μm; B 200 μm; C, 500 μm [99]

knockouts (i.e., aux1, lax1, lax2, aux1/lax1, aux1/lax2, lax1/lax2 plants) there was no significant leaf shape phenotype. However, when AUX1, LAX1 and LAX2 were all knocked out (the triple mutant) an observable phenotype was observed. In triple mutant leaves serrations were not distinguishable in the early and mid developmental stages (Fig. 4.6 A,B). When leaves reached the late developmental stage leaf serration did still occur although growth was stunted (Fig. 4.6 C).

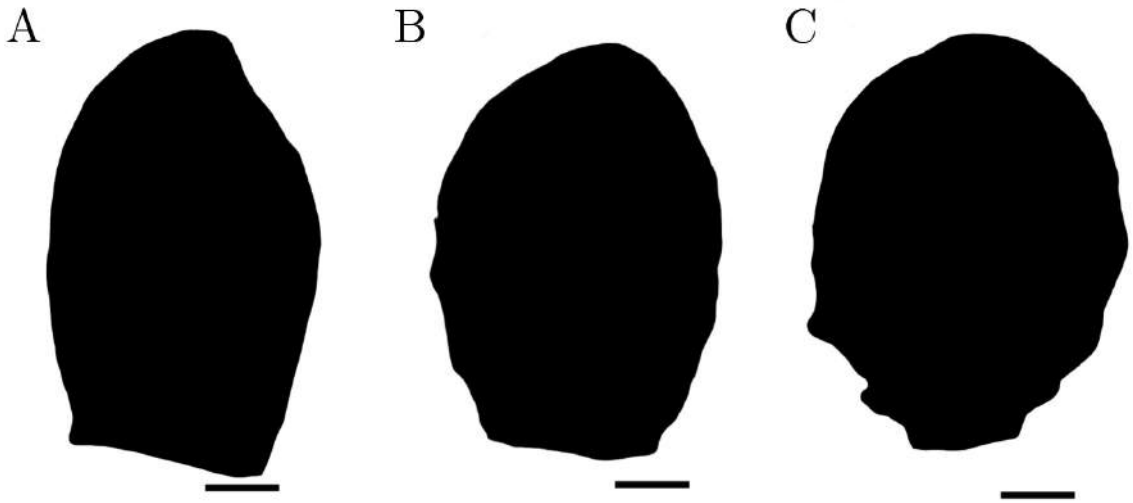

Figure 4.6: Silhouettes of Arabidopsis leaves for the AUX1/LAX1/LAX2 knockout mutant for three developmental stages. A, Early stage. B, Mid stage. C, Late stage. Scale bar A, 50 μm; B 200 μm; C, 500 μm [99]

As described in the introduction, an interplay between CUC2 transcription factors and

PIN1 auxin transport proteins is of major importance in shape change (serration formation) at the leaf margin [98]. To investigate whether knocking out combinations of LAX1/LAX2/AUX1 had an effect on the underlying PIN/CUC2 mechanism of serration formation, PIN1::GFP and CUC2::RFP constructs were transformed into mutant plant backgrounds and the pattern of gene expression observed. Figure 4.7 shows that PIN1 and CUC2 expression was similar in the triple mutant and the control WT background. Thus, in both genotypes PIN1 proteins point towards the serration outgrowth and CUC2 maxima remain at the sinuses (Figure 4.7C,D,G,H). Thus the basic PIN/CUC2 patterning machinery in the leaf margin appears unaffected by the loss of the three auxin importers and, thus, cannot account for the observed phenotype.

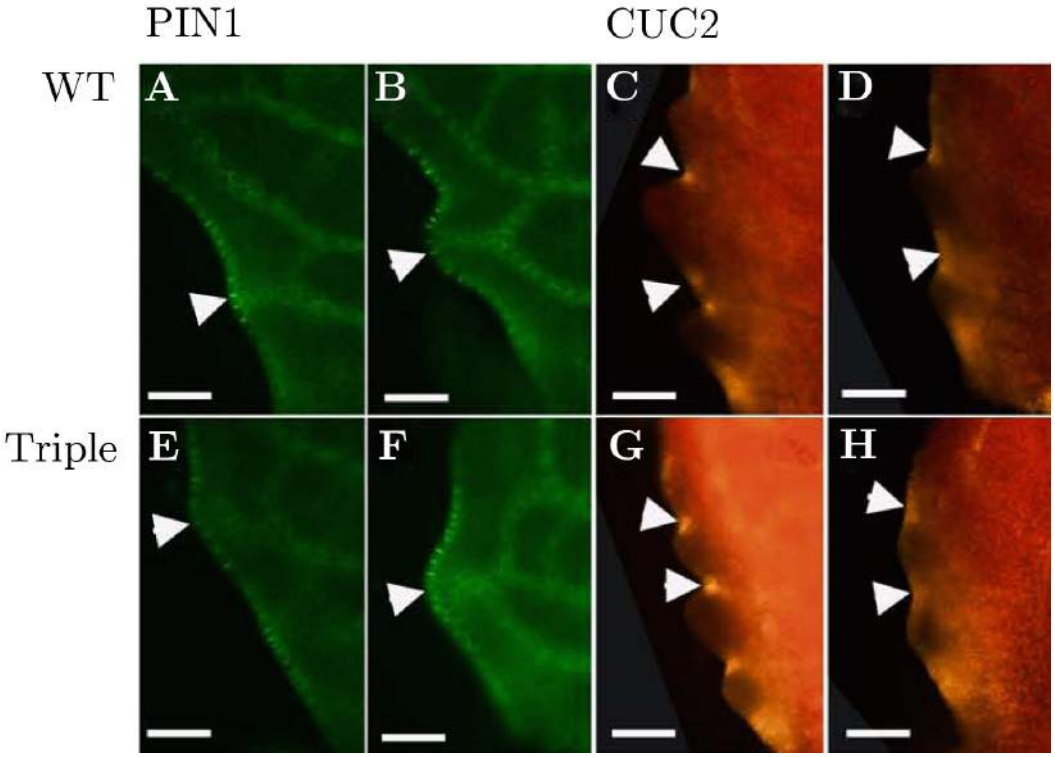

Figure 4.7: Fluorescence images of PIN1 and CUC2 localisation in the leaf margin. The top row is the wild type and the bottom row is the triple mutant. Scale bar 50 μm [99]

Another way of disrupting auxin transport is by the use of certain auxin transport inhibitors. One such inhibitor is n-1-naphthylphthalamic acid or NPA. Supplied to the leaf exogenously, NPA treatment leads to leaves with similar characteristics to the triple mutant, notably, a loss in serration formation and a smoother margin [103].

Control plants with DR5Pr::GUS expression show auxin signalling peaks at the tips of the serrations (Fig. 4.8 A-C). As shown in figure 4.8 D-F, after treatment with NPA the GUS signal intensity is greatly decreased but the signal is still restricted to the emerging serrations (which only occur later in leaf development). Patterns of LAX1 and LAX2 expression were similar in NPA treated leaves to those observed in the control leaves, but again, patterns of accumulation at the serration tips formed only at a later developmental stage and were less pronounced than in the controls (Fig. 4.9 A-F).

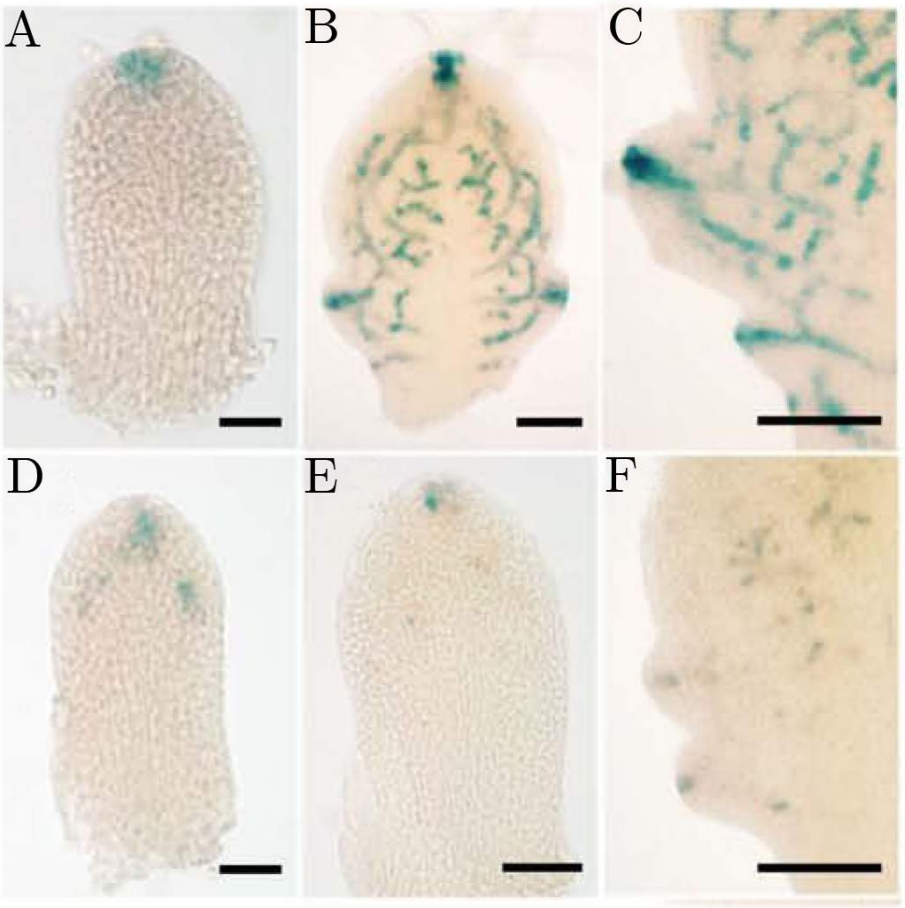

Figure 4.8: DR5 expression in a wild type leaf and a leaf treated with 10 μm NPA solution. A-C, early, mid and late stage wild type leaf. D-F, early, mid and late stage NPA treated leaf. Scale bars. A,D 50 μm. B,E 100 μm. C,F 500 μm. [99]

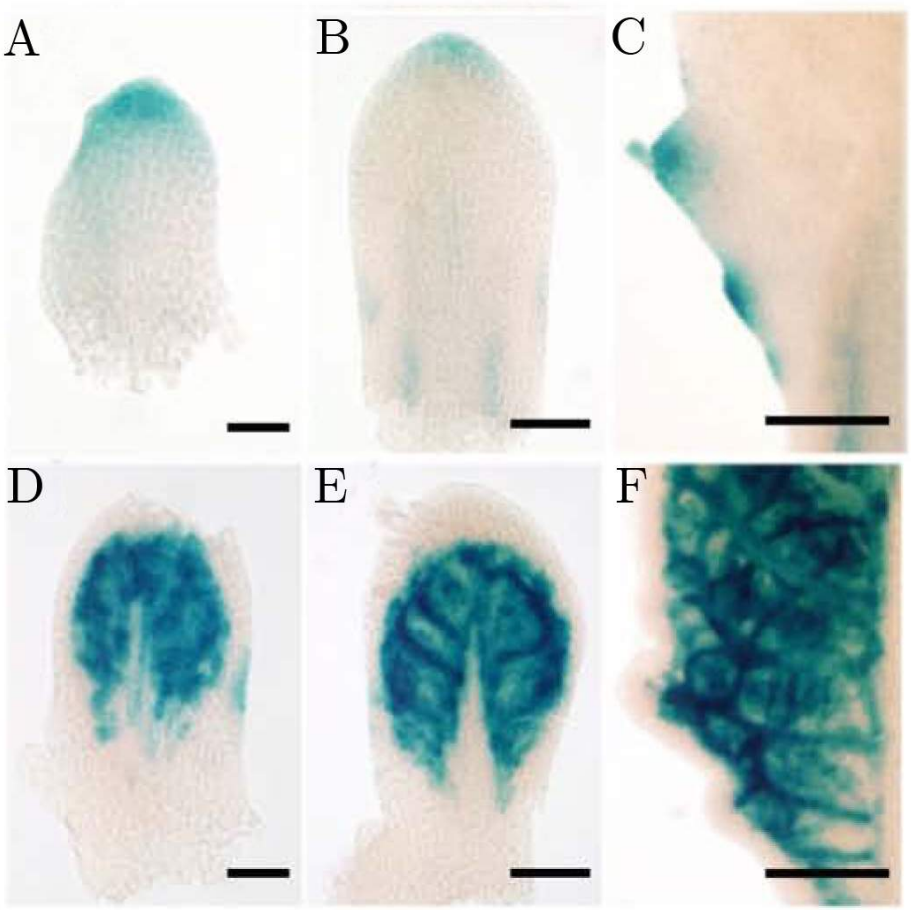

Figure 4.9: LAX1 and LAX2 expression in NPA treated leaves. A-C, LAX1 expression in an early, mid and late stage leaf. D-F, LAX2 expression in an early, mid and late stage leaf. Scale bars. A,D 50 μm. B,E 100 μm. C,F 500 μm. [99]

4.4 Description of the Mathematical Model

The aim of this study was to use the novel observations on auxin importer expression pattern and leaf phenotype (described in the previous sections) to develop a mathematical model which might assist in the interpretation of the data. Before constructing a model that describes the dynamics of auxin transport within the system, the geometry of the system must be defined.

4.4.1 Geometry of the Model

The system described by this model is a one dimensional row of N cells which represents the cells contained within the leaf boundary. Each cell is labelled with an index number, i, where $1 \leq i \leq N$. The cells 1 and N represent the cells adjacent to the petiole (Fig. 4.10). In this model the size of the cells and the cell walls is fixed to unity and the geometry is assumed to be static.

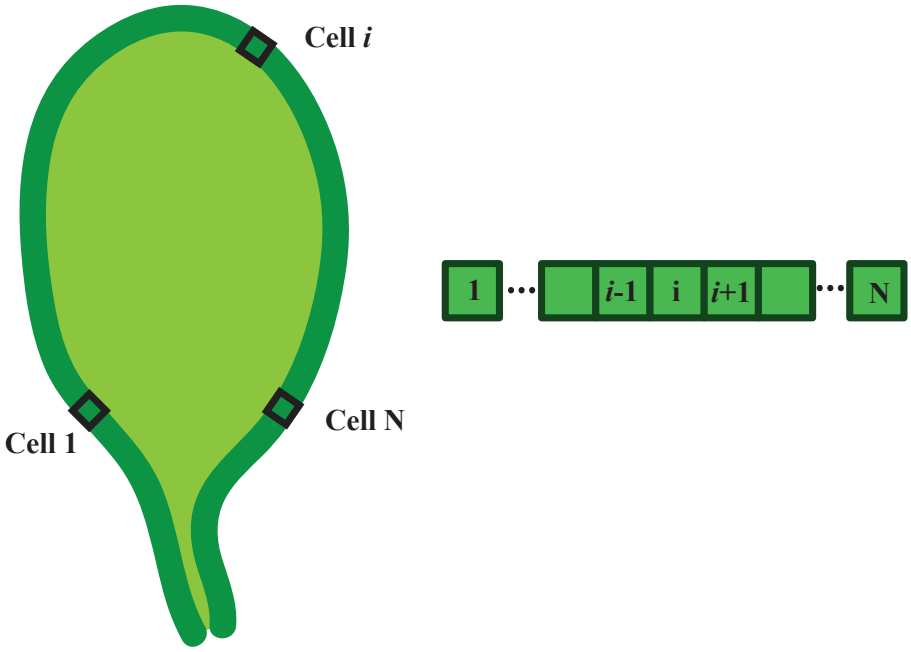

Figure 4.10: Geometry of the model, showing the positions of the boundary cells on a leaf and the one dimensional domain of square cells.

4.4.2 Molecular Processes

In the simulation, the time evolutions of the concentrations of auxin, CUC2 and LAX1/2 are described by an ordinary differential equation for each. These equations follow the formalism of Bilsborough *et al* [98] and were modified to include the action of auxin influx transporters. The rate of change of auxin concentration in cell i has the form:

$$\frac{d}{dt}[AUX]_i = p_1(p_2 - [AUX]_i) - p_3[AUX]_i + \Pi_i + \Delta_i \tag{4.4.1}$$

where $[AUX]_i$ is the concentration of auxin in cell i. The first term, $p_1(p_2 - [AUX]_i)$, describes the biosynthesis of auxin in the cell and is a saturating function. Auxin levels saturate at a value of p_2 with a rate controlled by p_1. The second term, $p_3[AUX]_i$, describes the linear degradation of auxin at a rate of p_3. Π_i represents the PIN1 mediated polar auxin transport into and out of cell i given by:

$$\Pi_i = p_4(-[AUX]_i + [PIN_{i-1\to i}][AUX]_{i-1} + [PIN_{i+1\to i}][AUX]_{i+1}) \tag{4.4.2}$$

The three terms in equation (4.4.2) represent, the auxin cell i transports to its neighbours (efflux) and the auxin transported into cell i from the cell's left and right neighbours (influx). p_4 is the auxin transport coefficient and represents the amount of auxin transported per time step.

$[PIN_{i-1\to i}]$ denotes the fraction of PIN1 on the membrane within cell $i-1$ adjoining cell i (Figure 4.11) and has the form:

$$[PIN_{i-1\to i}] = \begin{cases} \dfrac{6^{[AUX]_i}}{6^{[AUX]_i} + 6^{[AUX]_{i-2}}} & \text{if } [CUC2]_i > \text{Threshold} \\ 1/2 & \text{if } [CUC2]_i < \text{Threshold} \end{cases} \tag{4.4.3}$$

which models the recorded behaviour that PIN1 localises to the membrane neighbour-

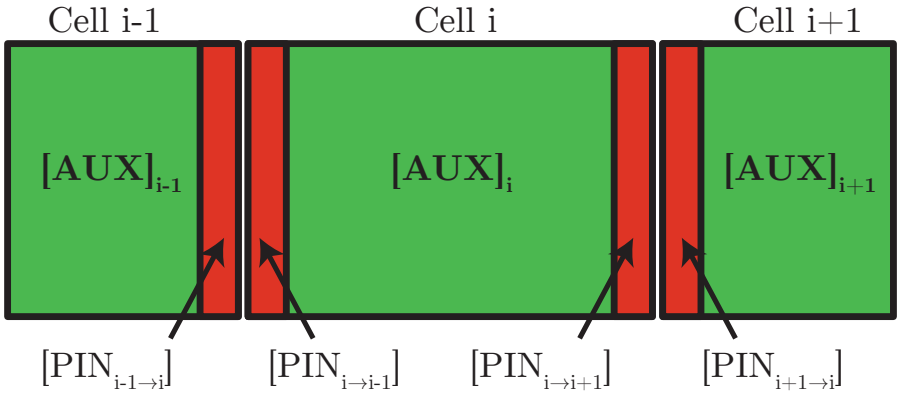

Figure 4.11: Diagram showing how the PIN concentration on the cell membranes is labeled

ing the cell upstream of the auxin flux [97]. The exponentiation base of six is an arbitrary choice and ensures a strong coupling of PIN1 localisation to walls neighbouring cells of high auxin concentration. CUC2 concentration has an effect on whether PIN1 can preferentially polarise to the cell membrane so equation (4.4.3) only holds if CUC2 within the cell in question is above a certain threshold level (in this case, 1). For CUC2 levels below that threshold PIN1 is distributed evenly between the two cell membranes and $[PIN_{i-1\to i}] = 0.5$ [98].

The apolar transport of auxin is modelled by:

$$\Delta_i = p_5\delta_i - p_{16}\delta_i - p_{10}[LAX1]_i\delta_i - p_{11}[LAX2]_i \tag{4.4.4}$$

The four terms represent auxin efflux by diffusion (at a rate, p_5), influx by AUX1 (at a rate, p_{16}), influx by LAX1 (at a rate, p_{10}) and efflux by LAX2 (at a rate, p_{11}) respectively. The δ_i term is the discrete version of the second derivative in space of $[AUX]$ and describes apolar transport of auxin:

$$\delta_i = ([AUX]_{i-1} - 2[AUX]_i + [AUX]_{i+1}) \tag{4.4.5}$$

The concentration of CUC2 in cell i is modelled by the following equation and follows the formalism of Bilsborough *et al* [98]:

$$\frac{d}{dt}[CUC2]_i = \frac{p_6}{1+p_7[AUX]_i}[CUC2]_i - (p_8 + p_9[AUX]_i)[CUC2]_i \tag{4.4.6}$$

Where $[CUC2]_i$ is the concentration of CUC2 in cell i. The first saturating term models the production of CUC2 with a production rate of p_6 and p_7 controls the amount of CUC2 down regulation by auxin. The second term models the CUC2 turnover, with a linear term with rate p_8 and an auxin dependent term with rate p_9.

LAX1 concentrations in cell i are modelled by the following equation:

$$\frac{d}{dt}[LAX1]_i = \frac{p_{12}[AUX]_i^2}{1+p_{13}[AUX]_i^2}[LAX1]_i - p_{14}[LAX1]_i \tag{4.4.7}$$

The form of the first term describes the production of LAX1 and captures the fact that LAX1 and auxin concentration maxima are co-localised but LAX1 maxima form later and assumes that these phenomena are causally linked (Fig. 4.1). p_{12} and p_{13} control the production rate and the maximum levels of LAX1 in the first term, which is a saturating function. The second term models a linear turnover of LAX1 at a rate of p_{14}. LAX1 acts as an auxin importer and the concentration, $[LAX1]_i$, is included in equation (4.4.1).

LAX2 concentrations in cell i are modelled by the following equation:

$$\frac{d}{dt}[LAX2]_i = \begin{cases} p_{15}(1-[LAX2]_i)[AUX]_i & \text{for } \ 26 < i < 74 \\ 0 & \text{otherwise} \end{cases} \tag{4.4.8}$$

LAX2 is only present in the interior of the leaf and is also an auxin importer. To model this fact the LAX2 term in equation (4.4.1) is an efflux term as auxin is being imported to the interior of the leaf, away from the marginal cells. The concentration of LAX2 is modelled by equation (4.4.8). LAX2 is produced at a rate of p_{15} and plateaus at a concentration of 1. LAX2 is only present towards the distal tip of the interior of the leaf (Fig. 4.2). To simulate this observation, LAX2 only has an effect on margin cells

that are towards the distal tip of the leaf or, in the case of this simulation, towards the centre of the file of cells. For these simulations the number of cells is 100 and LAX2 only has an affect on cells 26 to 74, the centre half of the leaf margin.

The fact that this differential expression of LAX2 is formally imposed on the model is the main mechanism that will decide the positioning and timing of the peaks. This is recreating what we see in the expression patterns (figure 4.2) and is, I feel, a reasonable hypothesis.

4.4.3 Simulating Mutants

Mutants were simulated by removing the effect that the knocked-out protein has on the auxin dynamics. This was achieved by setting the relevant parameter in equation (4.4.5) to zero, stopping the relevant protein having an effect on auxin concentration. For the LAX1 mutant, p_{10} was set to zero; for the LAX2 mutant, p_{11} was set to zero; and for the AUX1 mutant, p_{16} was set to zero.

Naphthylphthalamic acid (NPA) has been shown to inhibit PIN mediated polar auxin transport [104]. To simulate the effects of adding NPA to the system, the transport coefficient was adjusted. p_4, the PIN mediated transport rate, was changed to 80%/60%/40% of its default value to represent weak/medium/strong solutions of NPA respectively.

4.4.4 Initial Conditions and Boundary Conditions

The problem is an initial value problem (IVP) in the time dimension, and a boundary value problem (BVP) in the space dimension. The initial conditions take the following values:

$[AUX]_i(0) = AUX_0 = 0 + \epsilon\Theta_i$

$[CUC2]_i(0) = CUC2_0 = 1$

$$[LAX1]_i(0) = LAX1_0 = 0$$

$$[LAX2]_i(0) = LAX2_0 = 0$$

Where Θ_i is a random number selected from a uniform distribution between 0 and 1, and is different for each value of i. ϵ is a variable controlling the amplitude of the noise, in the default case $\epsilon = 0.01$.

The boundary conditions are set so that there is no gradient in auxin concentration, i.e. cells one and two have the same value of auxin as each other, as do cells $N-1$ and N.

This sets the gradient of auxin concentration to be zero at the boundaries all times (zero Neumann conditions) but allows the actual value to vary (variable Dirichlet conditions). The boundary conditions are not periodic as the leaf margin at either side of the petiole do not meet.

4.4.5 Parameter Values

Estimates for some of the parameters outlined in table 4.1 exist, such as approximate values for auxin transport and diffusion rates and rates of auxin production and turnover [97, 105–107]. At present most of the values remain unknown and the values chosen were speculative which is consistent with the qualitative nature of the model and are assumed to be of the correct order of magnitude. The various parameters, p_n, in equations (4.4.1) to (4.4.8) have the physical descriptions depicted in table 4.1. The values for wild type are listed and the values that were altered to simulate different mutants/treatments are also shown.

The columns have the following meanings:

- WT - Wild type
- L1 - LAX1 mutant
- L2 - LAX2 mutant

- A1 - AUX1 mutant
- TR - LAX1:LAX2:AUX1 mutant
- NPA - Naphthylphthalamic acid treatment (low, medium and high concentration treatments)
- BB - Original Bilsborough et al. model

4.4.6 Computation

This model was implemented in Matlab (v7.14, Mathworks). The differential equations were solved numerically using the ode45 function which uses an explicit Runge-Kutta algorithm. Specifically it uses the Dormand-Prince method to calculate fourth and fifth order accurate solutions [108]. The simulations were run on a 2.4 GHZ Intel Core 2 Duo MacBook Pro.

Parameter		Units	WT	L1	L2	A1	TR	NPA	BB	Reference
p_1	Auxin production rate	s^{-1}	0.4							[97, 105–107]
p_2	Maximum auxin level	$[conc]$	10							[97, 105–107]
p_3	Auxin turnover rate	s^{-1}	0.3							[97, 105–107]
p_4	Auxin transport coefficient	s^{-1}	0.4					0.32/0.24/0.16		[97, 105–107]
p_5	Auxin diffusion coefficient	s^{-1}	2.5							[97, 105–107]
p_6	CUC2 production rate	s^{-1}	63							
p_7	Sensitivity of CUC2 turnover to auxin	$[conc]^{-1}$	1.7							
p_8	CUC2 turnover rate	s^{-1}	3.6							
p_9	Auxin dependent CUC2 turnover rate	$[conc]^{-1}s^{-1}$	0.0018							
p_{10}	Auxin import due to LAX1	$[conc]^{-1}s^{-1}$	1.6	0			0		0	
p_{11}	Auxin export due to LAX2	$[conc]^{-1}s^{-1}$	2		0		0		0	
p_{12}	LAX1 production rate	$[conc]^{-2}s^{-1}$	2						0	
p_{13}	Auxin dependent LAX1 production rate	$[conc]^{-2}$	0.4						0	
p_{14}	LAX1 turnover rate	s^{-1}	1						0	
p_{15}	Maximun LAX2 level	s^{-1}	1						0	
p_{16}	AUX1 effect on auxin concentration	s^{-1}	0.1			0	0		0	

Table 4.1: Table of default parameter values for the simulation and the values changed to simulate mutants

4.5 Model Results

By looking at the time evolution and the spatial evolution of peaks and troughs in the concentration profiles, we start to see similarities between the expression patterns in the real leaves and the results of the simulation.

As shown by Bilsborough et al. [98] and described in the introduction, all that is needed to create a pattern of auxin peaks is an active transport of auxin against the gradient, provided by simulating the action of PINs, a diffusion term to stop peaks growing exponentially and a CUC2 term to control the polarisation of the PINs . However this formalism fails to account for some of the features we see in real *Arabidopsis* leaves, such as the temporal order of lobe formation and the distinct lack of lobes at the distal end of the leaf (Fig. 4.5). If this pattern is transduced into differential growth, then a leaf would be produced with serrations around the entire margin. This is not observed in real leaf (see Figure 4.5). If we just model the system using the PIN/CUC formalism then we get a pattern of auxin peaks interspersed with a pattern of CUC2 peaks (Fig. 4.12 A). With the addition of the AUX/LAX auxin importers to the model we see features more in common with those observed in real *Arabidopsis leaves* (Fig. 4.12 B), i.e, patterning occurs only towards the boundary of the model (equivalent to the base of the leaf).

A deeper insight into the model is provided by showing the outputs as space-time plots of the evolution of the auxin concentrations with the parameter choices from table 4.1, as shown in figure 4.13. The x-axis is time and the y-axis is cell number or space. The colour scale runs from bright red for maxima through to blue for minima. We make the assumption that a local maxima of auxin concentration is read out by cells in that area as a maxima of growth response, thus leading to morphogenesis and, in the case of this research, leaf serration.

The model results in a symmetrical pattern around the leaf perimeter with peaks of auxin concentration at the proximal end of the leaf (Figure 4.13 A). Due to the differ-

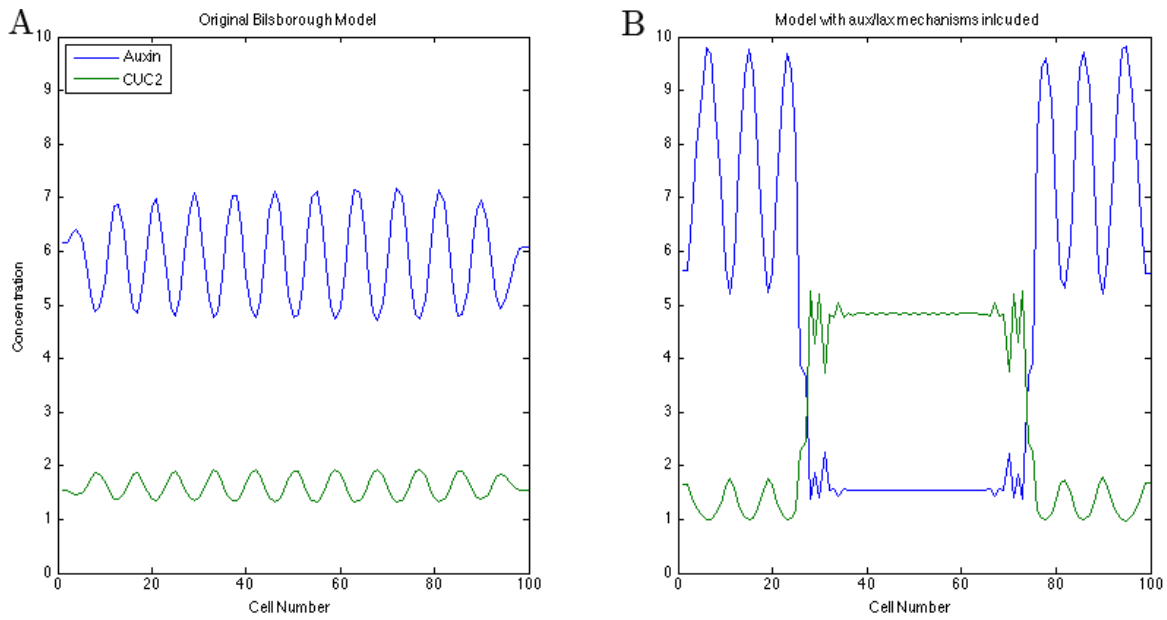

Figure 4.12: Comparison of results from the original Bilsborough model and the model with AUX/LAX mechanisms included. A, Original Bilsborough model showing no spatial regulation of auxin peaks. B, AUX/LAX model showing peaks limited to the proximal half of the leaf margin.

ential expression of LAX2 imposed in the model and the auxin drain this imposes on the perimeter, the distal end of the leaf lacks auxin peaks. This differential expression of LAX2 infers an internal boundary within the leaf driving the formation of peaks from an area closer to the boundary leading away in a reproducible temporal pattern. This mirrors what is seen in real leaves where serrations form in pairs closest to the distal end first and then further down towards the proximal end.

By removing the action of LAX1, LAX2 and/or AUX1 by setting the relevant parameters in table 4.1 to zero, we can simulate knockout mutants in these genes and compare the output results to leaves from the relevant *Arabidopsis* knockouts. Figures 4.13 B, C and D show space-time plots for these knockouts. The removal of LAX1 or AUX1 (Figure 4.13 B and C) had no significant effect on the outcome of the simulation. Peaks were less sharply defined and formed slightly later but the number of peaks and the timing of peak formation remained essentially unchanged. Single mutants in these genes are thus predicted to have no significant phenotype and that is what we observe in leaves from *Arabidopsis* AUX1 and LAX1 mutants.

A significant phenotype was only observed in the model when the action of LAX2

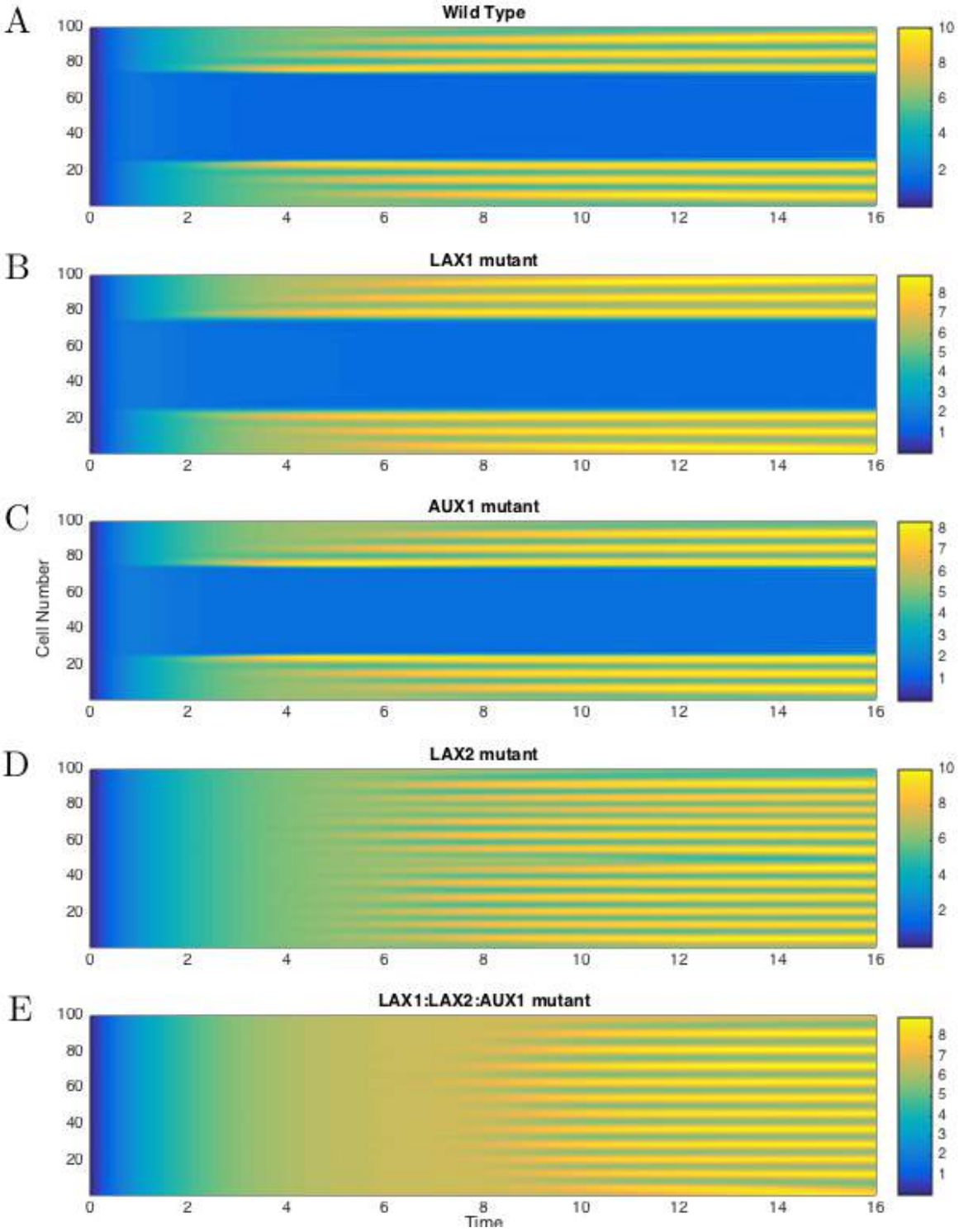

Figure 4.13: AUX/LAX model results for the auxin concentration ($[AUX](t)$). A, Wild type. B, LAX1 mutant. C, AUX1 mutant. D, LAX2 mutant. E, Triple mutant.

was removed (Figure 4.13 D), either on its own or in combination with AUX1/LAX1 (Figure 4.13 E). The most obvious difference is the fact that patterning is no longer limited to the periphery of the system and peaks form evenly across the boundary, including at the distal tip. This phenotype was not observed in reality in either LAX2 or LAX1/LAX2/AUX1 (triple) mutant leaves. Another less obvious phenotype is that the formation of peaks in both the LAX2 and the triple mutant is delayed, more significantly so in the triple. In the wild type (Figure 4.13 A) patterning occurs at roughly the 2 second time point. In the LAX2 mutant (Figure 4.13 D) patterning is delayed and starts later at around 4.5 seconds. In the triple mutant (Figure 4.13 E) patterning is delayed further and starts at around the 7 timepjoint.

To account for the difference between the model output and the observed phenotype we have to be aware of the fact that hormone signalling is a complex process. Plants generally have methods to turn off signals or to restrict the time in which a signal can affect development. There has been much dispute as to the importance of hormone sensitivity in developing systems, but the fact that signals have a sensitivity window, a specific timeframe in which these signals will have an effect, remains key to the understanding of development as a whole and in particular, morphogenesis [109]. There is very limited experimental data with respect to the formation of serrations on the leaf margin, but to investigate the discrepancy between the modelled and actual phenotypes of the LAX2/Triple mutants we looked at the effects of imposing an auxin sensitivity window on the model. Making the assumption that the relationship between cell age and auxin sensitivity is linear, we imposed a simple rule that cells over a certain age cannot respond to changes in auxin concentration. In the model we set cells at the distal tip to be insensitive early on, and then increased this range with time so that eventually the entire leaf margin was set to be insensitive to auxin. Figure 4.14 shows the effect that imposing this sensitivity window had on the model output. The dark shaded area represents cells that have reached a certain age and are assumed to have lost the ability to respond to changes in auxin concentration. In the

wild type and the LAX1/AUX1 single mutants (Figure 4.14 A, B and C) the inclusion of the sensitivity window has little effect on the overall patterning as the systems have reached steady state by the time the sensitivity window passes. However in the LAX2 and the triple mutants (Figure 4.14 D and E) auxin patterning in the centre of the pattern (equivalent to the distal tip of the leaf) occurs after the sensitivity window passes, indicating that the potential changes in auxin concentration that occur here may not be interpreted by the cells in this region as a signal to perform the tasks necessary for morphogenesis to occur. Thus in the case of LAX2, if we include this sensitivity window formalism, the model produces results in line with real leaves from the LAX2 mutant with serrations only occurring at the proximal end of the leaf. In the triple mutant, patterning is delayed to the point where very little patterning occurs before the sensitivity window passes. This matches the phenotype observed in the triple mutant (Figure 4.6) in which the formation of serrations is greatly delayed and they never reach the size of those in the wild type.

The choice of the form of the sensitivity window in figure 4.14 is completely and changes in the timing and form will influence the pattern output of the model. The model points to the potential importance of the sensitivity concept in interpreting experimental data and highlights the need for more research into its molecular nature.

The effect of naphthylphthalamic acid (NPA) on the system was also simulated. NPA is an auxin transport inhibitor. Leaves following this treatment showed similar phenotypes to the triple mutant in that the formation of serrations was delayed and they formed much smaller leaves than those for the wild type. To simulate the effect of NPA on the system the parameter controlling the strength of auxin transport by PIN1 proteins was adjusted to values shown in table 4.1. To simulate the effect of a low/medium/high concentration of NPA the transport parameter was lowered to 80%/60%/40% of its initial value (Figure 4.15 A, C and E). The effects of low and medium concentrations of NPA on the model output were to change the timing of the pattern formation, moving it to a later time point. When NPA concentration was in-

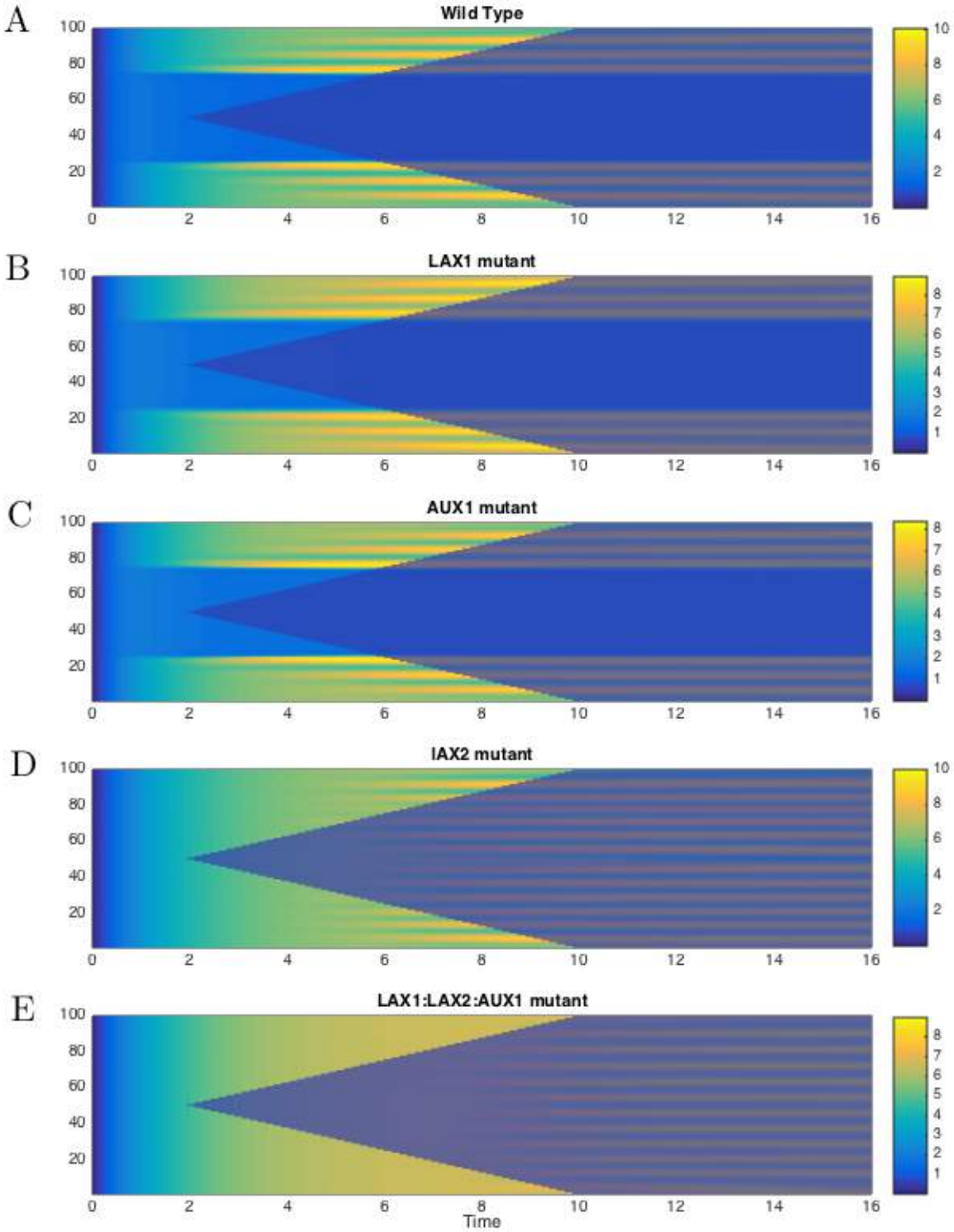

Figure 4.14: AUX/LAX model results with sensitivity overlay for the auxin concentration ($[AUX](t)$). A, Wild type. B, LAX1 mutant. C, AUX1 mutant. D, LAX2 mutant. E, Triple mutant.

creased over a certain point patterning failed to start at all. In this system patterning is a competitive process between active transport of auxin against the gradient and diffusion acting to smooth out the distribution. If the active transport is not strong enough to overcome the diffusion then no patterning occurs. Figure 4.15 B, D and F show the same results but with the sensitivity window described in the previous section overlaid. If patterning can happen soon enough, as in the proximal region of Figure 4.14 B then these signals may still lead to morphogenesis. If however the patterning is delayed, as in Figure 4.14 D or not present at all, as in Figure 4.14 F, then morphogenesis of the leaf margin will not occur at all. This influence of varying NPA concentration on margin serration is observed in real leaves, thus the model captures this part of the patterning system. This is a validation of the modelling techniques as we can match simulation outputs to experimentally observed results.

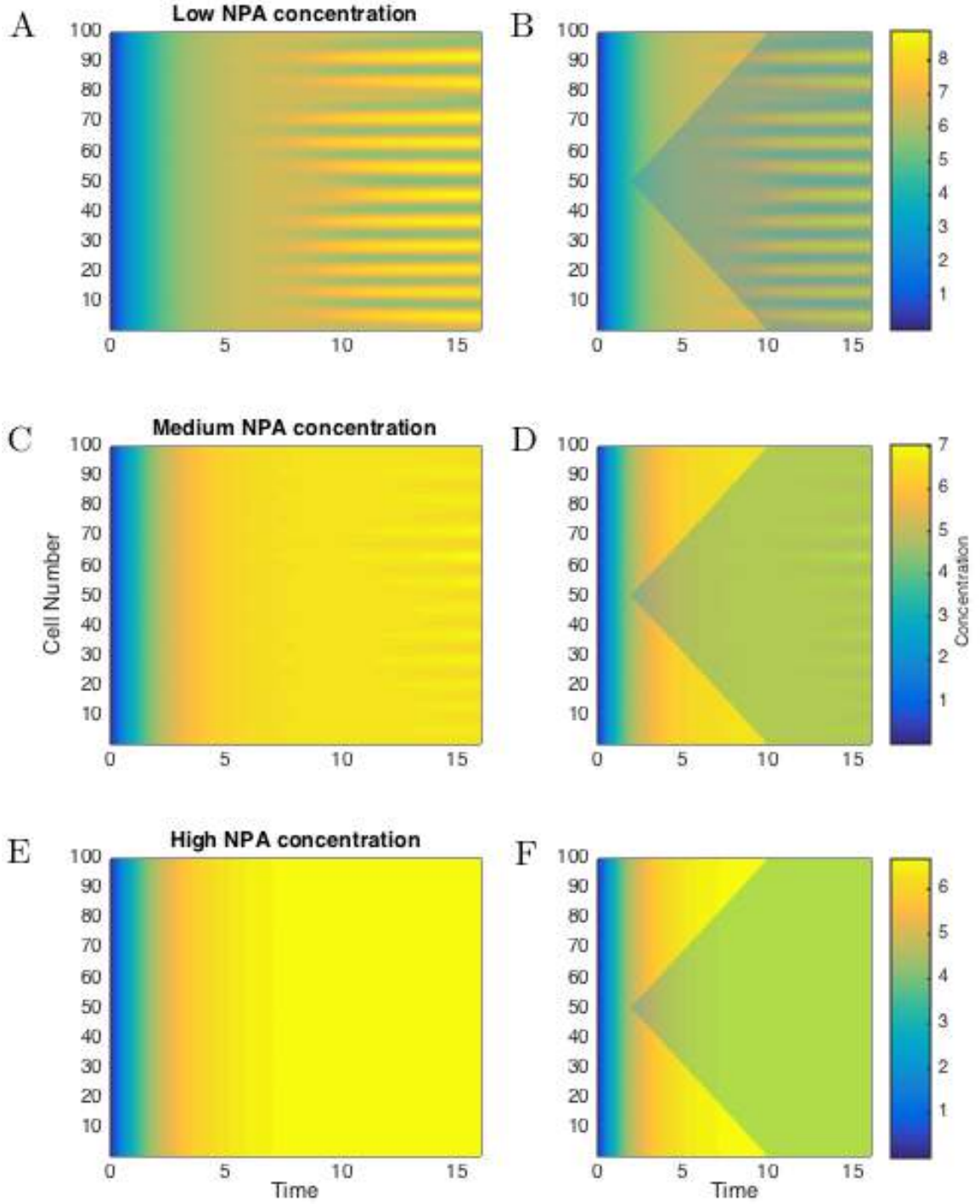

Figure 4.15: Model results for auxin concentration ($[AUX](t)$) for wild type with simulated application of NPA. A,B, Low NPA concentration with/without sensitivity overlay. C,D, Medium NPA concentration with/without sensitivity overlay. E,F, High NPA concentration with/without sensitivity overlay.

4.6 Parameter Sensitivity

To test how sensitivite the output of the model is to changes in the parameters, some kind of metric of the model output is required. A Fast Fourier Transform (FFT) of the auxin concentration solution in the space domain will return a list of coefficients of a combination of sinusoids that approximate that solution. The coefficient that is the largest represents the frequency of the sine wave with the frequency that best represents the model output. The frequency of the peaks is the main result of the model as the spacing is the only quantitative measure available from the gene expression data given in section 4.2.

By varying the input parameters of the model between 0.25 and 2.5 times their default values, and measuring the difference between the largest Fourier coefficient, a measure of how the parameter affects the model output can be obtained.

If D_{MAX} is the largest Fourier coefficient when the parameter is at its highest value and D_{MIN} is the largest Fourier coefficient when the parameter is at its lowest value then the sensitivity index (SI) [110] of that parameter is:

$$SI = \frac{D_{MAX} - D_{MIN}}{D_{MAX}} \tag{4.6.1}$$

The sensitivity index ranges from $0 < SI < 1$ and is a measure of how much effect the parameter change has on the output. A value of one is a complete change and a value of zero is no change.

Figure 4.16 shows the values of the sensitivity index obtained by varying the parameters between 0.25 and 2.5 times their default values. Even for the parameters with a high SI, varying the parameters by this amount leaves the important features of the model, the spacing of the auxin peaks, intact. This range of variation reflects the uncertainty in the experimentally derived values [105]. The parameters with the largest stability index were the maximum auxin level, the auxin turnover rate, auxin

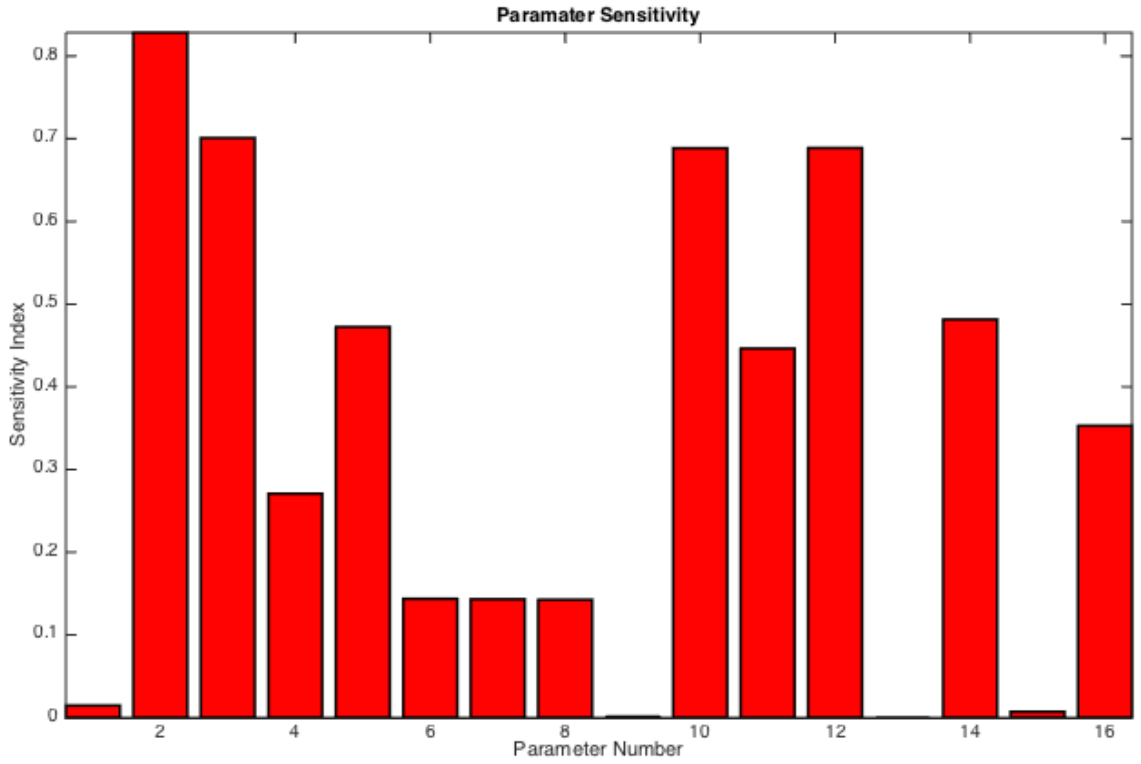

Figure 4.16: A graph of parameter sensitivity indicating the scale to which a change in parameters will have an affect on the output of the model. The parameters are varied by between 0.25 and 2.5 times their default values.

import due to LAX1 and the LAX1 production rate. All these parameters function in the production and accumulation of auxin so their effect on the spacing of final auxin concentrations is unsurprising.

4.7 Stability Analysis

To test the stability of the system we can employ mathematical techniques such as linear stability analysis, which shows whether time independent solutions to the system of differential equations are stable.

Each discrete cell within the model has its own set of equations describing the dynamics of the various concentrations:

$$
\begin{cases}
\frac{d}{dt}[AUX]_i = & p_1(p_2 - [AUX]_i) - p_3[AUX]_i \\
& +p_4(-1 + \frac{6^{[AUX]_i}}{6^{[AUX]_i}+6^{[AUX]_{i-2}}} + \frac{6^{[AUX]_i}}{6^{[AUX]_i}+6^{[AUX]_{i+2}}})[AUX]_i \\
& +(p_5 - p_{16} - p_{10}[LAX1]_i)([AUX]_{i-1} - 2[AUX]_i + [AUX]_{i+1}) \\
& -p_{11}[LAX2]_i[AUX]_i \\
\frac{d}{dt}[CUC2]_i = & \frac{p_6}{1+p_7[AUX]_i} - (p_8 + p_9[AUX]_i)[CUC2]_i \\
\frac{d}{dt}[LAX1]_i = & \frac{p_{12}[AUX]_i^2}{1+p_{13}[AUX]_i^2} - p_{14}[LAX1]_i \\
\frac{d}{dt}[LAX2]_i = & p_{15}(1 - [LAX2]_i)[AUX]_i
\end{cases}
$$

To perform a stability analysis we need to look at the steady state, homogenous solutions. Setting the time derivatives to zero gives the steady state behaviour:

$$
\begin{cases}
0 = & p_1(p_2 - [AUX]_i) - p_3[AUX]_i \\
& +p_4(-1 + \frac{6^{[AUX]_i}}{6^{[AUX]_i}+6^{[AUX]_{i-2}}} + \frac{6^{[AUX]_i}}{6^{[AUX]_i}+6^{[AUX]_{i+2}}})[AUX]_i \\
& +(p_5 - p_{16} - p_{10}[LAX1]_i)([AUX]_{i-1} - 2[AUX]_i + [AUX]_{i+1}) \\
& -p_{11}[LAX2]_i[AUX]_i \\
0 = & \frac{p_6}{1+p_7[AUX]_i} - (p_8 + p_9[AUX]_i)[CUC2]_i \\
0 = & \frac{p_{12}[AUX]_i^2}{1+p_{13}[AUX]_i^2} - p_{14}[LAX1]_i \\
0 = & p_{15}(1 - [LAX2]_i)[AUX]_i
\end{cases}
$$

This system can be written as the system of equations;

$$F(\mathbf{U}, \mathbf{p}) = 0, \tag{4.7.1}$$

where $F : \Re^{4n+m} \to \Re^{4n} : (\mathbf{U}, \mathbf{p}) \mapsto F(\mathbf{U}, \mathbf{p})$ where n is the number of cells and m is the number of parameters. $\mathbf{U}$ is a $4n$ sized solution vector of the problem that contains the 4 variables and $p \in \Re^m$ denotes the set of parameters.

For the homogenous case, where no patterning occurs, i.e. $[AUX]_i = A_0, [CUC2]_i = C_0, [LAX1]_i = L1_0, [LAX2]_i = L2_0$

The model reduces down to

$$
\begin{cases}
0 = p_1(p_2 - A_0) - p_3A_0 - p_{11}L2_0A_0 \\
0 = \frac{p_6}{1+p_7A_0} - (p_8 + p_9A_0)C_0 \\
0 = \frac{p_{12}A_0^2}{1+p_{13}A_0^2} - p_{14}L1_0 \\
0 = (1 - L2_0)A_0
\end{cases}
\tag{4.7.2}
$$

If we solve these equations simultaneously we can get values for the four variables in

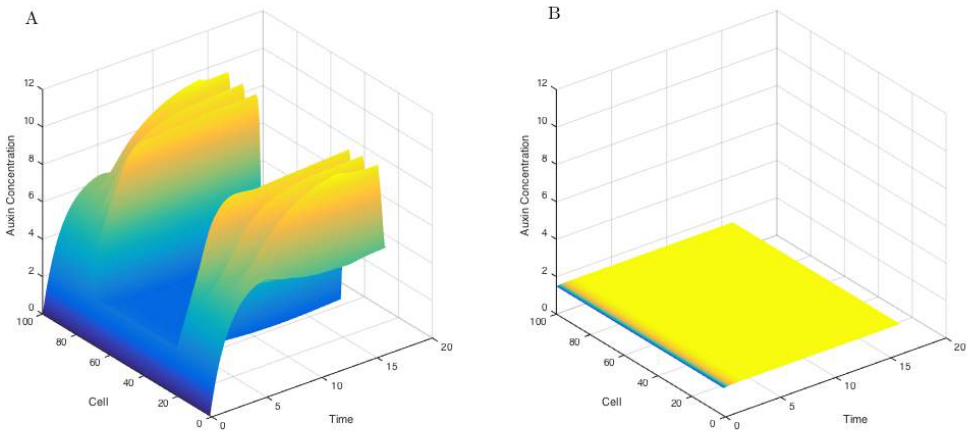

Figure 4.17: Time evolution of auxin concentrations over time. A. Concentration profile for the simulation with the default initial conditions showing the expected patterning B. Concentration profile for the simulation with the initial conditions stated in equation (4.7.4)

terms of the parameters that will give a solution that is homogenous and steady state in time.

$$\begin{cases} A_0 = \frac{p_1 p_2}{p_1+p_3+p_{11}} \\ C_0 = \frac{p_6(p_1+p_3+p_{11})^2}{(p_8 p_1+p_8 p_3+p_8 p_{11}+p_9 p_1 p_2)(p_1+p_3+p_{11}+p_7 p_1 p_2)} \\ L1_0 = \frac{p_{12} p_1^2 p_2^2}{p_{14}(p_1^2+2p_1 p_3+2p_1 p_{11}+p_3^2+2p_3 p_{11}+p_{11}^2+p_{13} p_1^2 p_2^2)} \\ L2_0 = 1 \end{cases} \tag{4.7.3}$$

With the default values of the parameters show in table 4.1, these variables will have values of approximately :

$$\begin{cases} A_0 = 1.48 \\ C_0 = 4.97 \\ L1_0 = 2.34 \\ L2_0 = 1.00 \end{cases} \tag{4.7.4}$$

Using these values for the initial conditions in the simulation leads to a steady state solution where no patterning occurs, as shown in figure 4.17.

The Jacobian of the steady state system of equations will allow us to analyse the stability of the system to small perturbations. For the case of spatially homogenous perturbations of the form $A_1 e^{\lambda t}$ (where $A_1 << 1$) the Jacobian for the system is:

$$J(\mathbf{U}, \mathbf{p}) = \begin{bmatrix} -p_1 - p_3 - p_{11}\, L2 & 0 & 0 & -p_{11} A \\ -\frac{p_6\, p_7}{(1+p_7\, A)^2} - p_9\, C & -p_8 - p_9\, A & 0 & 0 \\ 2\,\frac{p_{12}\, A}{1+p_{13}\, A^2} - 2\,\frac{p_{12}\, A^3 p_{13}}{(1+p_{13}\, A^2)^2} & 0 & -p_{14} & 0 \\ 1 - L2 & 0 & 0 & -A \end{bmatrix} \tag{4.7.5}$$

and the characteristic polynomial of J is $det(J - \lambda I)$ (where I is the identity matrix).

Solving the characteristic polynomial gives the following eigenvalues for the system;

$$\lambda = \begin{bmatrix} -p_{14} \\ -p_8 - p_9 A \\ -\frac{1}{2}A - \frac{1}{2}p_{11}L2 - \frac{1}{2}p_1 - \frac{1}{2}p_3 + \frac{1}{2}\sqrt{A^2 + 2p_{11}L2\,A - 2p_1 A - 2p_3 A + p_{11}^2 L2^2 + 2p_1 p_{11} L2 + 2p_3 p_{11} L2 + p_1^2 + 2p_1 p_3 + p_3^2 - 4p_{11} A} \\ -\frac{1}{2}A - \frac{1}{2}p_{11}L2 - \frac{1}{2}p_1 - \frac{1}{2}p_3 - \frac{1}{2}\sqrt{A^2 + 2p_{11}L2\,A - 2p_1 A - 2p_3 A + p_{11}^2 L2^2 + 2p_1 p_{11} L2 + 2p_3 p_{11} L2 + p_1^2 + 2p_1 p_3 + p_3^2 - 4p_{11} A} \end{bmatrix} \tag{4.7.6}$$

which, with the default values of the parameters and the homogenous steady-state solutions of A, C, $L1$, and $L2$, gives numerical values of

$$\begin{cases} \lambda_1 = -1 \\ \lambda_2 = -3.605 \\ \lambda_3 = -1.4 \\ \lambda_4 = -2.857 \end{cases} \tag{4.7.7}$$

All these eigenvalues are real and negative which shows that the system is stable to spatially homogenous perturbations. For patterning to occur some sort of spatial perturbation needs to be introduced and this is the purpose of the noise in the initial conditions mentioned in section 4.4.4.

In the future it might be possible to perform a full linear stability analysis, including heterogenous perturbations in space and time, to calculate the range of parameters for which the homogenous state is unstable. This unstable state could then lead to a solution where patterning occurs. Relating these parameter ranges to the experimental uncertainties in the measured parameters would give an idea as to how biologically plausible the formalism for pattern generation in the model is.

4.8 Conclusion

We have shown that a significant phenotype in the leaf margin is only visible when removal of the action of the three AUX1/LAX genes occurs. This phenotype includes a delay of serration formation and the production of smaller serrations compared to the wild type. The observations from the gene expression data of the wild type and various mutants and the phenotypes we see in these mutants have been incorporated into a mathematical model. This model provides a possible explanation as to how these expression patterns and phenotypes arise and highlights the often overlooked fact that speed of pattern formation is critical.

Of course every mathematical model of a system is a simplification, given enough time and computational power the model could have included more systems. This model was a static one dimensional system with a fixed number of cells. Having a growing system with rules of how auxin concentrations lead to cell growth and division could lead to more realistic results being achieved.

This model only included cells within the leaf margin, of course leaf development is a complex process involving many processes and cell types. This model ignores any non-perimeter effects, but a future, more complete, model would include effects from the rest of the leaf. These effects could include signalling and transport from the vasculature tissue, effects of margin growth on epidermal pavement cells, or even a model of auxin transport across the entire leaf surface taking into account differing

cell types and vasculature. Although it has been shown that many morphogenetic processes that regulate leaf shape take place on the leaf margin [98], sub epidermal cells could also have an effect on auxin patterning. Kwak *et al* [111] have shown that for the case of root hair patterning, a receptor in the epidermal cells is able to read positional cues from the underlying cell layer. These cues then go on to determine the developmental cell fate of the epidermal cell (reviewed in [112]).

A PIN/CUC model of serration formation in the leaf margin may be sufficient to produce serrations, but for these serrations to form in the correct place, a localised expression of the auxin importer LAX2 is required. LAX1 is required to control the timing of patterning in this system, as patterns of auxin concentration need to occur before cells lose their sensitivity to auxin signals. This sensitivity window is a key parameter in describing some of the observed phenotypes and the timing of pattern formation in morphogenesis is likely very important in the development of organs.

Further work in this area is needed to explore the mechanistic basis of auxin sensitivity, such as by looking at gene expression data and leaf shape phenotypes of certain auxin response mutants (such as mutants of genes in the axr, auxin response family [113]).

The AUX/LAX family of genes have been implicated in early cotyledon development [114] and in the organisation of embryonic cells in the root [115], but their role in patterning in leaf morphogenesis has, until now, been overlooked. Leaf shape is of utmost importance to the efficiency of photosynthesis and gas exchange; if we can get a grasp of the processes underpinning leaf shape development this will lead the way to manipulating shape and maybe optimising photosynthesis.

Chapter 5

General Conclusions

The main aim of this research has been the development of atomic force microscopy methods for the investigation of the mechanical properties of plant cells *in vivo*.

Early work focused on the hypocotyl of *Arabidopsis thaliana*. Measurements were made to attempt to identify mechanical phenotypes in certain expansin over expresser mutants. Expansin is a protein involved in cell wall loosening and the over expression of it was expected to reduce the measured stiffness of the hypocotyl cell wall. Results obtained had a large variance,which meant it was not possible to identify trends which backed up the hypotheses. This highlighted the care that needs to be taken when interpreting AFM force measurements and directed future work to concentrate on the relative differences within single force maps.

This early work led to the question of whether the variance seen in the hypocotyl measurements was due to natural variation in the sample or whether it was an artefact of the sample preparation technique or AFM measurements. Two experiments were performed to investigate potential sources of variation with the AFM measurements. The force measurements being made on the cell wall were not perpendicular to the surface. As force is vectorial it was decided to investigate the effect that angle of indentation had on the measurements being made. Force maps were acquired on a

homogenous material (dental silicone) so that any differences caused by the angle of indentation would be detected. These experiments indicated that this topographical effect was not significant, and correction for geometry was not required in further analyses.

An investigation into the effects that depth of indentation had on the AFM measurements was also performed. Flat areas of the abaxial side of the leaf were force mapped with varying trigger values (i.e., indentation depths) and the force curves were analysed. The dependence of the stiffness values on the indentation depth was determined and an optimal level of indentation (40 nm) was decided upon for future work.

Further research focussed on stomata, due to the fact that previous research has indicated that to function effectively there needs to be a some kind of difference between the mechanical properties of guard cells and their supporting cells. It was hoped that this research would back up that claim as, currently, there have been no published data on the direct measurement of the mechanical properties of guard cells. Early measurements showed a significant difference between the stiffness of the guard cells that make up the stomata and the surrounding cells that support them and it was decided to investigate this further. Although this stark difference was not noticed to such an extent in later experiments, the stiffness of the cells did correlate with other, geometrical measurements. The stiffness ratio (relative stiffness of guard cells compared to supporting cells) was found to correlate with stomatal size, and using size as a proxy for age, the conclusion was reached that stomata at an earlier developmental stage were less stiff when compared to their supporting cells. Another measurement that seemed to correlate with this stiffness ratio was relative pore width (pore width divided by stomate width). This may indicate that when a stomata is open, and the turgor pressure is high, this can be measured in the stiffness of the cell wall, maybe due to some kind of tension stiffening effect.

Experiments were performed to test the viability of mounted leaves and validate the method of plant sample preparation. These experiments used the viability stain fluo-

roscein diacetate to test the viability of stomatal cells. These experiments found the sample preparation technique keeps stomatal cells viable.

Data analysis methods bundled with the commercial AFM software were deemed unsuitable for the work carried out. Custom algorithms were developed to extract the measured stiffness from force indentation experiments. Methods for calculating average stiffness over the entire indentation, average stiffness over the initial 40 nm of indentation and instantaneous stiffness at 40nm of indention were developed but only the latter was used in analysis. As the indentation depth would vary depending on the stiffness of the sample, stiffnesses calculated by the first method in section 3.2.4 would be an average over different depths, and possibly over different layers of the cell wall. The second method in section 3.2.4 was better as this standardised measurements to a certain depth, but it was still reporting an average. The third method in section 3.2.4, calculating the instantaneous stiffness at a prescribed depth was deemed the best as this stiffness would be independent of interactions before the indentation depth was achieved.

During this work on the stomata, the dynamics of opening and closing were also investigated. A solution of the signalling molecule abscisic acid (ABA) and a solution of the osmolyte mannitol were used to control the opening and closing of stomata. Continuous AFM contact mode images were taken during the opening and the speeds at which this happened were calculated. This was only performed on a low number of samples so results may be considered preliminary but during the measurement of these dynamic effects it was noticed that the stomatal cell wall buckles in a characteristic fashion and position. Research carried out by Meckel *et al* [85] showed that the plasma membrane of stomatal cells changes surface area during opening and closing. As the cell wall cannot change surface area reversibly within the same time scales, this buckling could be to accommodate these plasma membrane changes. This offers a different explanation to the volume changes required in stomatal opening and closing which have so far presumed to be due to the stretching of the cell wall. Further work

is required to investigate this effect.

The original aim of this project was to combine AFM mechanical measurements of the leaf margin with predictive models of auxin dynamics to give an indication of the effect auxin has on the mechanics of morphogenesis. Unfortunately, due to technical challenges, the measurements on the leaf margin were not able to be performed.

The aim of the model was to incorporate knowledge of auxin importers into existing models of auxin transport. Existing models failed to account for the fact that separations on *Arabidopsis* leaves occur only in the proximal half of the leaf. We used data on the expression of the AUX/LAX family of auxin importers to construct a model that more realistically recreates what is seen during leaf development, and the phenotypes when AUX/LAX genes are knocked out.

This model correctly predicted the temporal and spatial emergence of auxin peaks in the leaf margin and recreated the phenotypes seen in most of the mutants. One of the phenotypes not recreated was the one for the LAX2 mutant, however with the addition of a putative auxin sensitivity window, this phenotype was recovered. This shows that the AUX/LAX family may have a larger role in leaf morphogenesis than previously thought, acting to stabilise peaks and influence the timing. The importance of a cells sensitivity to changes in auxin concentration during different developmental stages is a mechanism that is often overlooked.

5.1 Future Work

As mentioned in section 2.2.3, the topography of the sample greatly limits the maximum scan size that can be achieved during AFM scanning. With different AFM setups the maximum z-range can be increased up to 100 μm and combined with the x and y limits, also 100 μm, this would give a maximum scanning volume of a 100μm cube. Allowing large areas to be scanned simultaneously would allow the same kind

of comparisons of mechanical properties as outlined for stomata in Chapter 3. With automated sample stages combined, it is not beyond the realms of possibility that entire leaves (or at least primordia) could be scanned and measured, giving insight into the mechanical changes that occur during leaf morphogenesis.

By improving the methods of sample fixation (translucent fixing media) or by using an AFM mounted on an upright microscope it would be possible to obtain simultaneous AFM measurements with fluorescent micrographs. By using plants that have specific fluorescent markers on genes involved in cell wall maintenance it should be possible to correlate mechanical measurements with areas of gene expression, offering another method of mechanical phenotyping. Such research has been performed recently by Milani *et al* [116] where they looked at links between the expression of a gene involved in the regulation of the stem cell zone and changes in mechanical properties in the shoot apex.

With theses mechanical changes measured over the entire leaf, additions to predictive models of leaf morphogenesis could be made. By correlating the mechanical properties with levels of auxin in certain areas one could predict the effect of other genetic mutants and improve and inform future models of morphogenesis.

Appendix A

Data Analysis Code

Custom data analysis code written in IGOR Pro version 6.32A

Method one calculates the gradient of the contact section of the force curve, returning a value for the average stiffness over the entire indentation:

```
Function FMapCalcStiff(Data,DataB,ParmWave)
    Wave Data
    Wave/Z DataB
    Wave/Z ParmWave

    Variable Output = 1/SlopeCurveFunc(Data,DataB)
    return(output)

End //FMapCalcStiff
```

Method two calculates the gradient over the initial 40 nm of indentation, returning an average stiffness for this initial indentation:

```
Function FMapCalcInitialStiff(Data,DataB,ParmWave)
    Wave Data                    //Force (y)
    Wave/Z DataB              //Ind (x)
    Wave/Z ParmWave     //not used


    // Line Subtract
    Variable LineFitSlope, LineFitIntercept
    variable LSindex = FindSurfaceIndex(Data,DataB,10) - 100
    Poly1Fit(DataB,Data,1,LSindex,LineFitSlope,LineFitIntercept)
    Data = Data - LineFitSlope * DataB

    //Y Offset
    WaveStats  /Q /R = [0, 20 ]/Z Data
    Data = Data - V_avg

    //X Offset

        //AR Method
```

```
        variable surfindexAR = FindSurfaceIndex(Data,DataB,10)
        variable xoffsetAR = DataB[surfindexAR]

        //Back extrapolate method
        variable n = numpnts(DataB)
        Variable SlopeBE, InterceptBE
        Poly1Fit(DataB,Data, n -20 , n-10 ,SlopeBE, InterceptBE)
        variable xoffsetBE = -interceptBE/slopeBE

    variable diff = xoffsetAR - xoffsetBE

    DataB = DataB - xoffsetBE


    FindLevel/P/Q DataB,5e-9 //find 10 nm searching left to right
    if (V_Flag)
        return(0)
    endif
    Variable TENnmPt = round(V_LevelX)
    FindLevel/P/Q DataB,50e-9 //find 50 nm searching left to right
    if (V_Flag == 1)
         FindLevel/P/Q DataB,wavemax(DataB)
         Variable SIXTYnmPt = round(V_LevelX)
    else
          SIXTYnmPt =round(V_LevelX)
    endif

    //variable TENnmPt = rossx2pnt(dataB,lowInd)
    //variable SIXTYnmPt = rossx2pnt(dataB,highInd)

    Variable Slope, Intercept
    Poly1Fit(DataB,Data,TENnmPt,SIXTYnmPt,Slope,Intercept)

    return(Slope)

End //FMapCalcStiff
```

Method three fits a 3rd order polynomial to the contact section, differentiates this and returns the value of the gradient at 40 nm:

```
Function FMapCalcPolyStiff(Data,DataB,ParmWave)
    Wave Data                   //Force (y)
    Wave/Z DataB            //Ind (x)
    Wave/Z ParmWave     //not used


    // Line Subtract
    Variable LineFitSlope, LineFitIntercept
    variable LSindex = FindSurfaceIndex(Data,DataB,10) - 100
    Poly1Fit(DataB,Data,1,LSindex,LineFitSlope,LineFitIntercept)
    Data = Data - LineFitSlope * DataB

    //Y Offset
    WaveStats  /Q /R = [0, 20 ]/Z Data
    Data = Data - V_avg
```

```
    //X Offset

        //AR Method
        variable surfindexAR = FindSurfaceIndex(Data,DataB,10)
        variable xoffsetAR = DataB[surfindexAR]

        //Back extrapolate method
        variable n = numpnts(DataB)
        Variable SlopeBE, InterceptBE
        Poly1Fit(DataB,Data, n -20 , n-10 ,SlopeBE, InterceptBE)
        variable xoffsetBE = -interceptBE/slopeBE

    variable diff = xoffsetAR - xoffsetBE

    DataB = DataB - xoffsetBE


    FindLevel/P/Q DataB,5e-9 //find 10 nm searching left to right
    if (V_Flag)
        return(0)
    endif
    Variable TENnmPt = round(V_LevelX)
    FindLevel/P/Q DataB,60e-9 //find 50 nm searching left to right
    if (V_Flag == 1)
         FindLevel/P/Q DataB,wavemax(DataB)
         Variable SIXTYnmPt = round(V_LevelX)
    else
          SIXTYnmPt =round(V_LevelX)
    endif

    Wave W_coef

    CurveFit/NTHR=0 /Q /N=1 poly_XOffset 4, kwCWave=W_coef, Data[TENnmPt,numpnts(Data)-

    variable ind = 30e-9
    variable Slope = W_coef[1] + 2*W_coef[2]*ind + 3*W_coef[3]*ind^2

    if (slope < 0 )
        slope = 0
    endif

    return(Slope)

End //FMapCalcStiff
```

Appendix B

Stomata Data

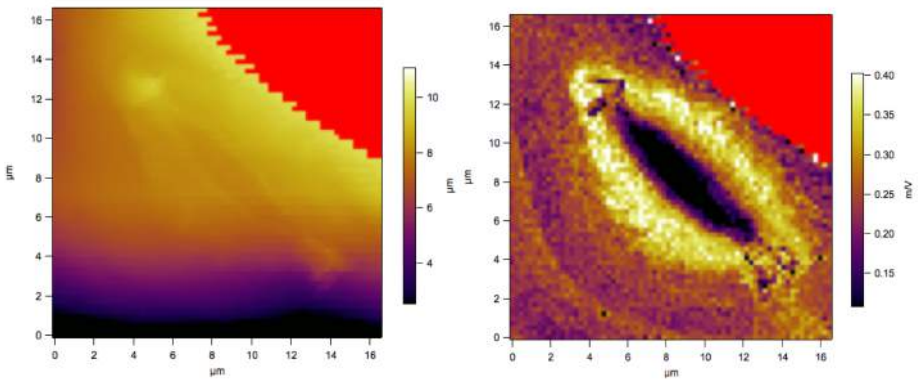

Figure B.1: Stomata 3 force map. A. Height map showing the topography. B. Stiffness map showing the spatial distribution of the mechanical properties.

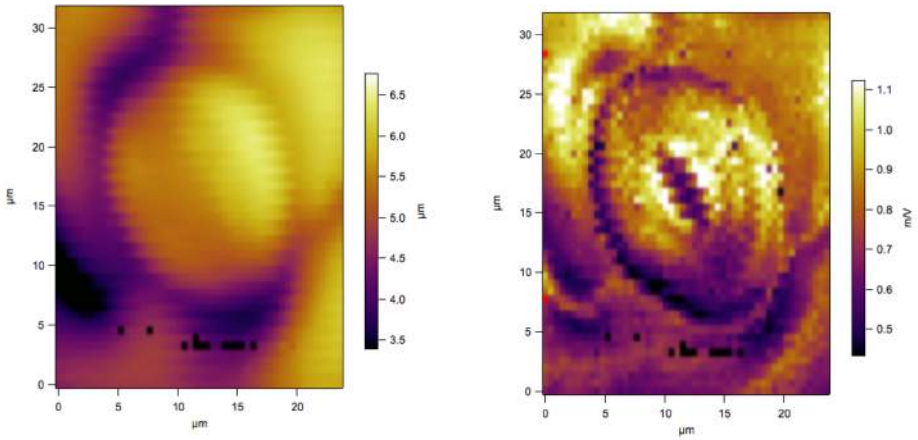

Figure B.2: Stomata 4 force map. A. Height map showing the topography. B. Stiffness map showing the spatial distribution of the mechanical properties.

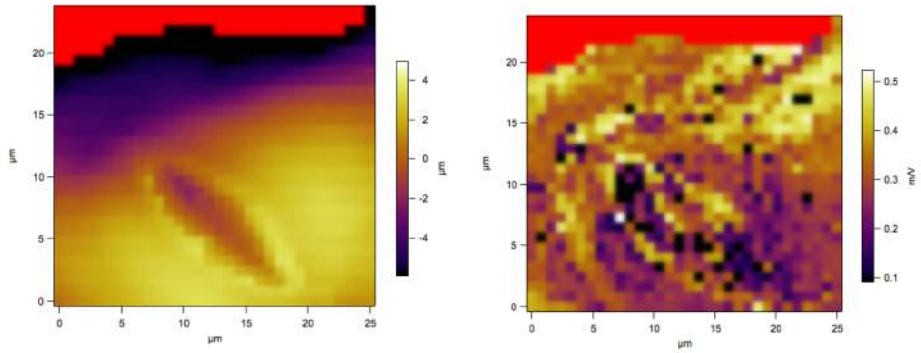

Figure B.3: Stomata 5 force map. A. Height map showing the topography. B. Stiffness map showing the spatial distribution of the mechanical properties.

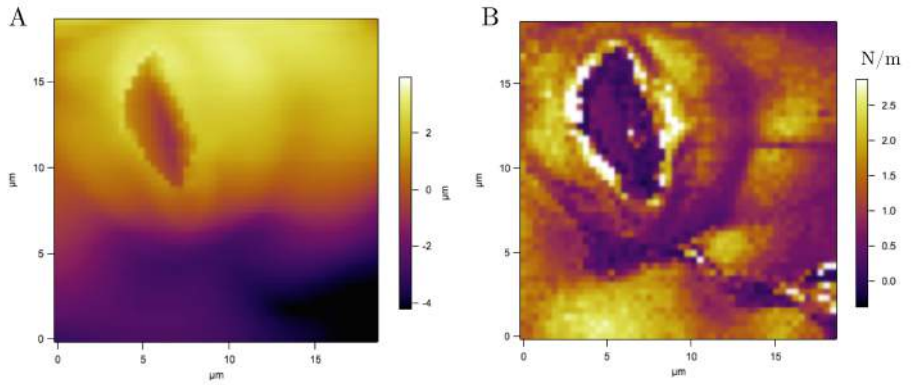

Figure B.4: Stomata 6 force map. A. Height map showing the topography. B. Stiffness map showing the spatial distribution of the mechanical properties.

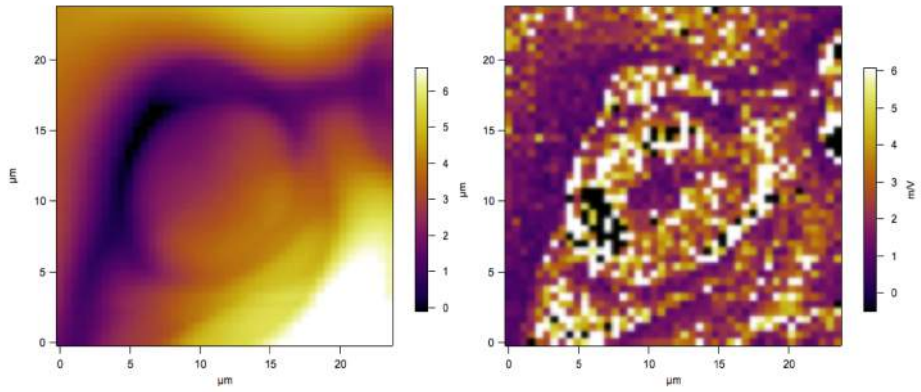

Figure B.5: Stomata 7 force map. A. Height map showing the topography. B. Stiffness map showing the spatial distribution of the mechanical properties.

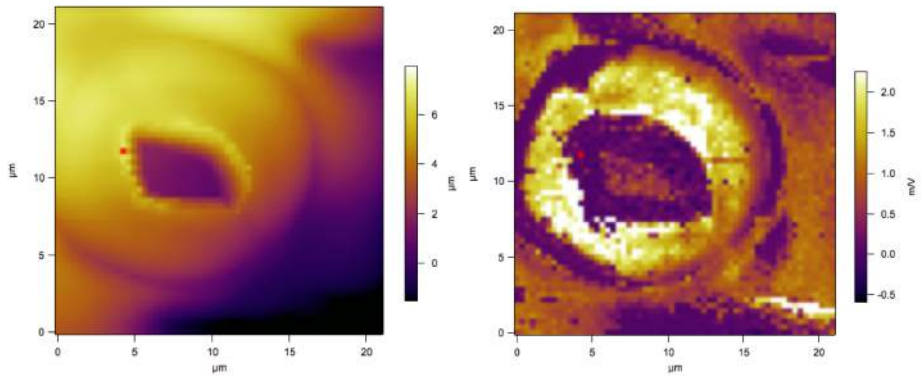

Figure B.6: Stomata 8 force map. A. Height map showing the topography. B. Stiffness map showing the spatial distribution of the mechanical properties.

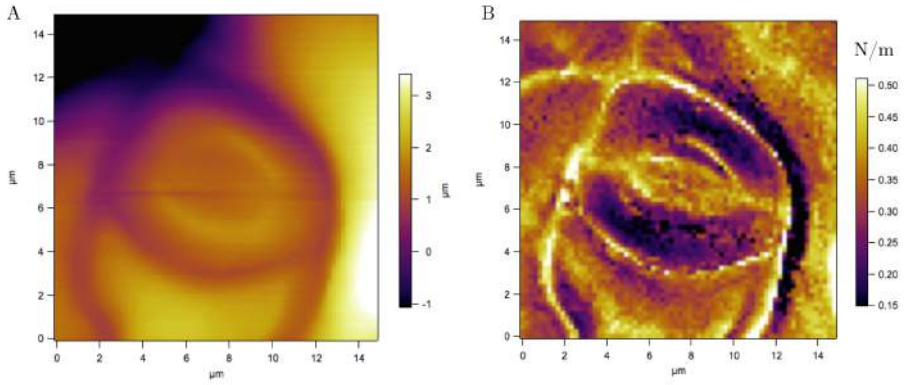

Figure B.7: Stomata 9 force map. A. Height map showing the topography. B. Stiffness map showing the spatial distribution of the mechanical properties.

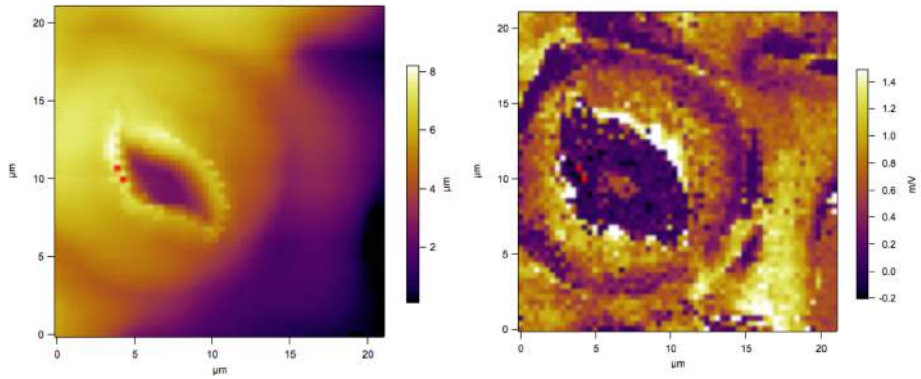

Figure B.8: Stomata 10 force map. A. Height map showing the topography. B. Stiffness map showing the spatial distribution of the mechanical properties.

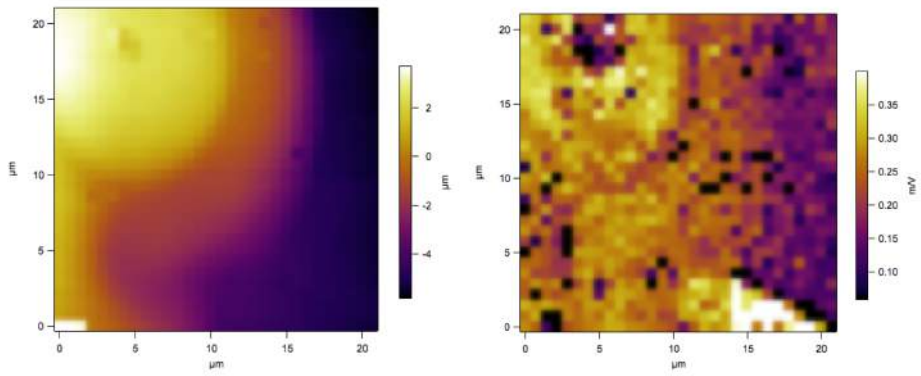

Figure B.9: Stomata 12 force map. A. Height map showing the topography. B. Stiffness map showing the spatial distribution of the mechanical properties.

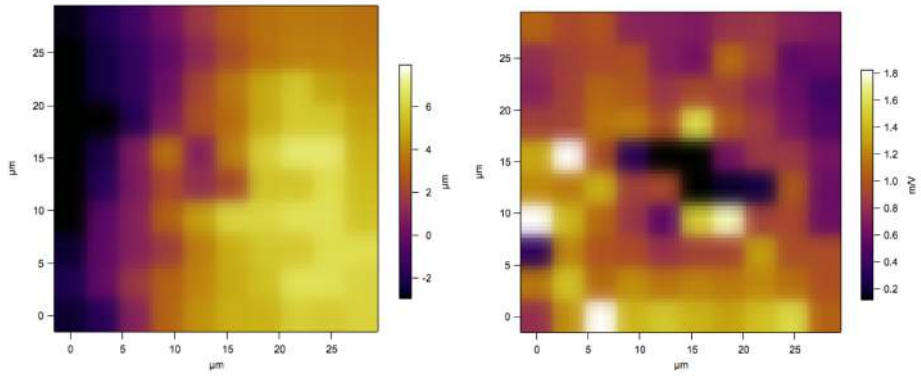

Figure B.10: Stomata 13 force map. A. Height map showing the topography. B. Stiffness map showing the spatial distribution of the mechanical properties.

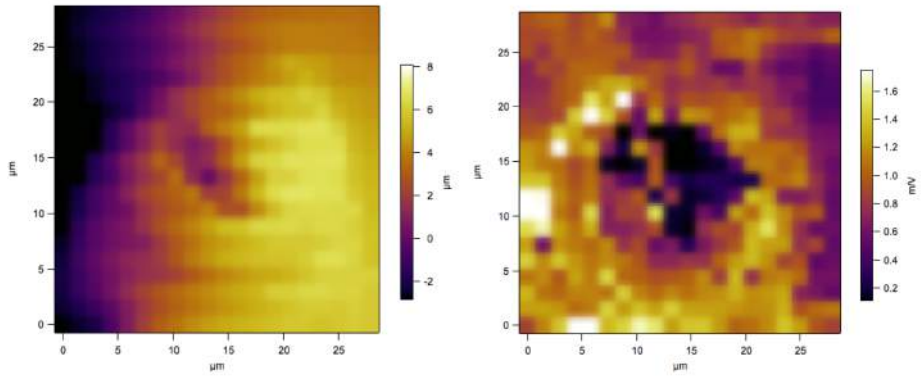

Figure B.11: Stomata 14 force map. A. Height map showing the topography. B. Stiffness map showing the spatial distribution of the mechanical properties.

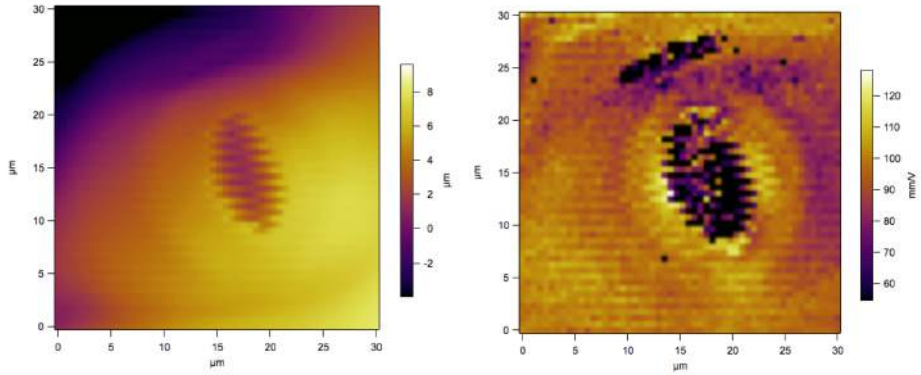

Figure B.12: Stomata 15 force map. A. Height map showing the topography. B. Stiffness map showing the spatial distribution of the mechanical properties.

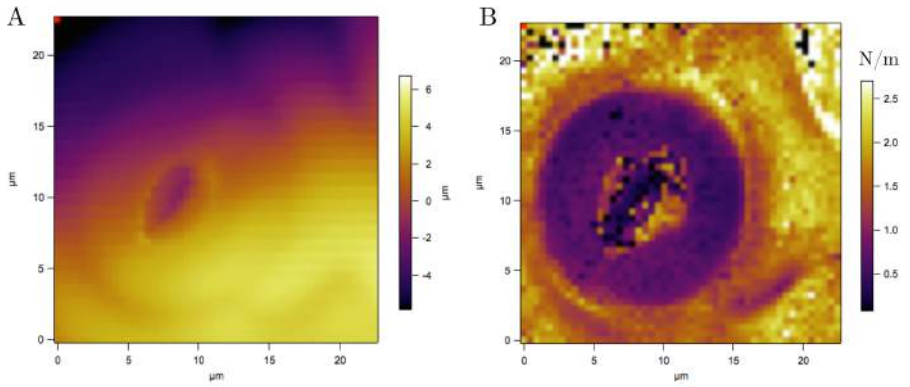

Figure B.13: Stomata 16 force map. A. Height map showing the topography. B. Stiffness map showing the spatial distribution of the mechanical properties.

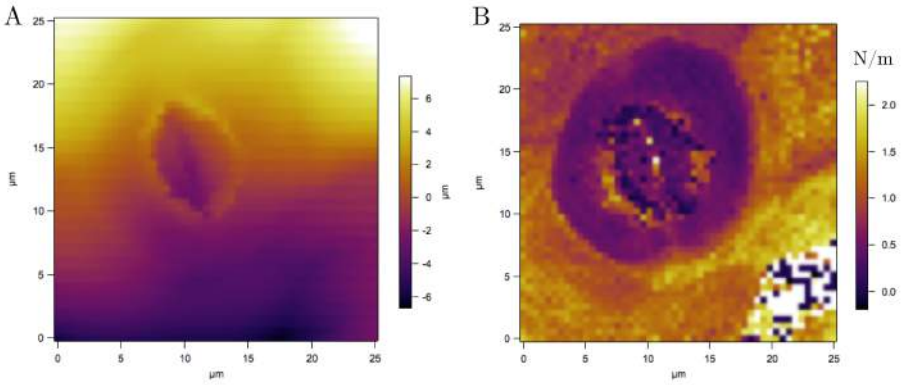

Figure B.14: Stomata 17 force map. A. Height map showing the topography. B. Stiffness map showing the spatial distribution of the mechanical properties.

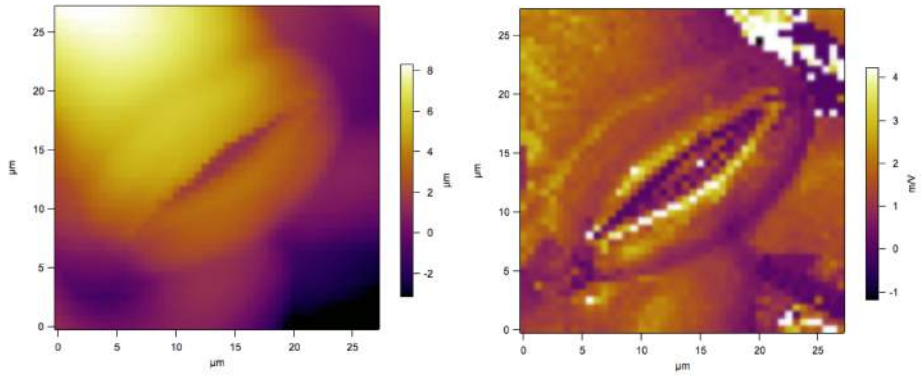

Figure B.15: Stomata 18 force map. A. Height map showing the topography. B. Stiffness map showing the spatial distribution of the mechanical properties.

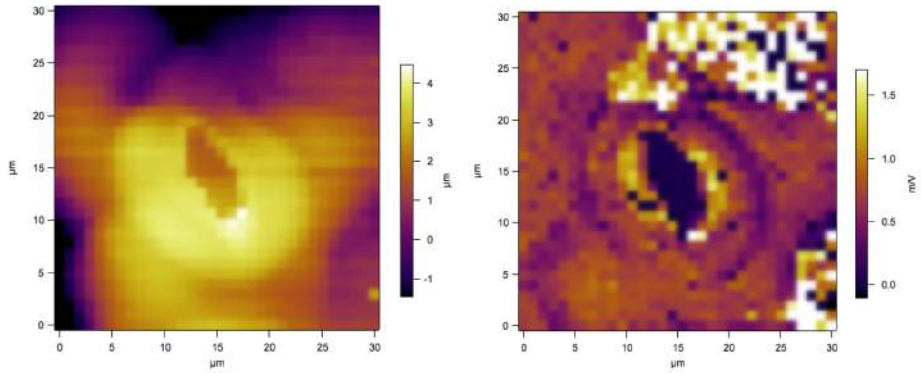

Figure B.16: Stomata 19 force map. A. Height map showing the topography. B. Stiffness map showing the spatial distribution of the mechanical properties.

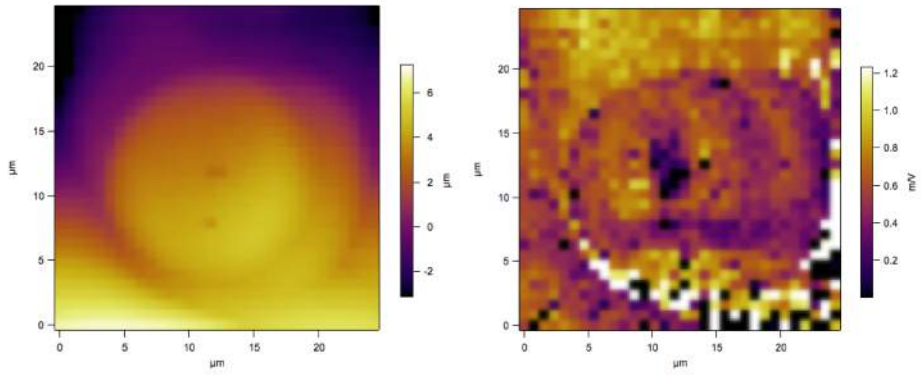

Figure B.17: Stomata 20 force map. A. Height map showing the topography. B. Stiffness map showing the spatial distribution of the mechanical properties.

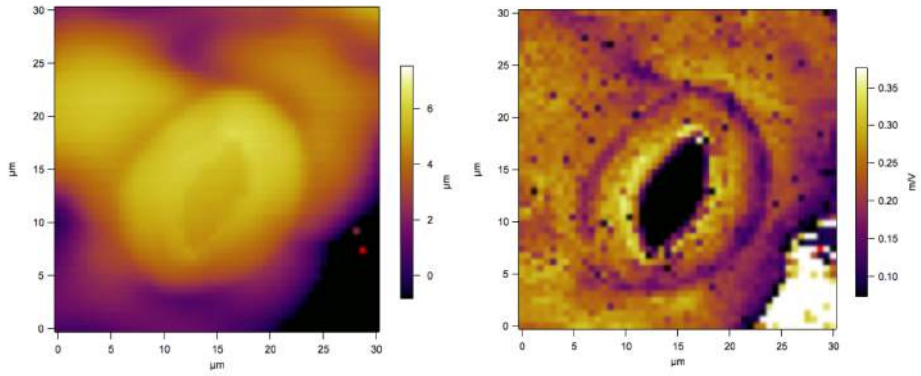

Figure B.18: Stomata 21 force map. A. Height map showing the topography. B. Stiffness map showing the spatial distribution of the mechanical properties.

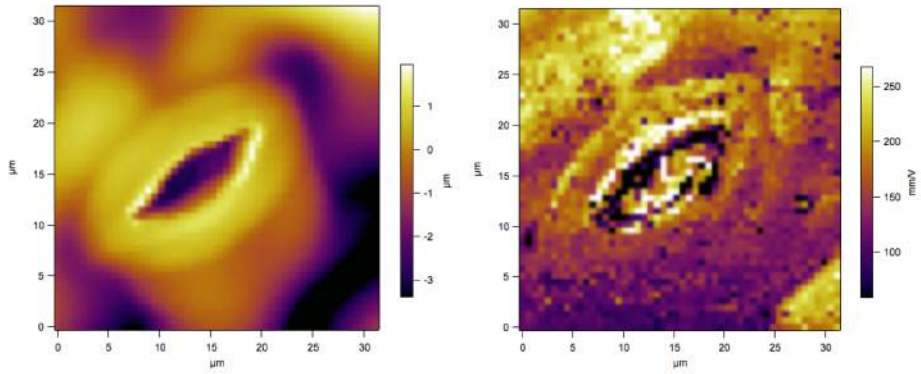

Figure B.19: Stomata 22 force map. A. Height map showing the topography. B. Stiffness map showing the spatial distribution of the mechanical properties.

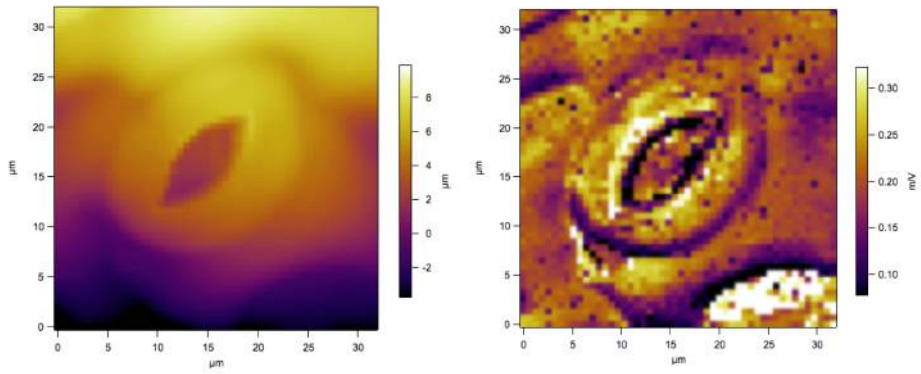

Figure B.20: Stomata 23 force map. A. Height map showing the topography. B. Stiffness map showing the spatial distribution of the mechanical properties.

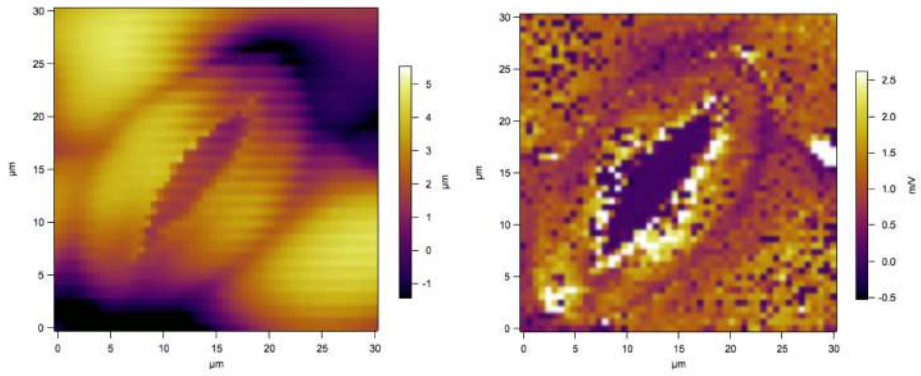

Figure B.21: Stomata 24 force map. A. Height map showing the topography. B. Stiffness map showing the spatial distribution of the mechanical properties.

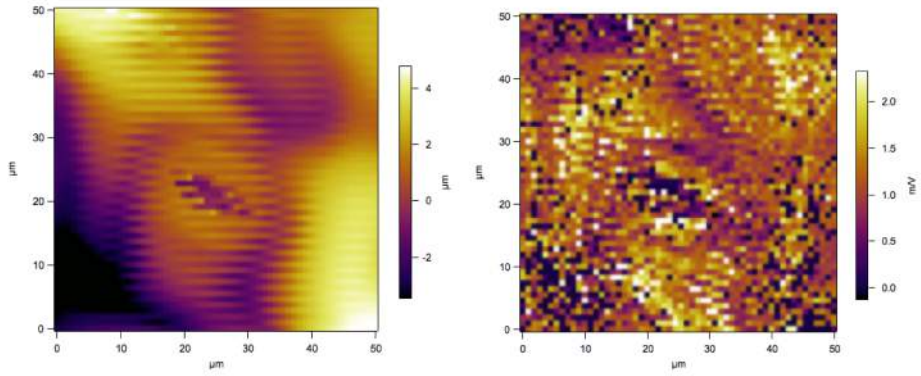

Figure B.22: Stomata 25 force map. A. Height map showing the topography. B. Stiffness map showing the spatial distribution of the mechanical properties.

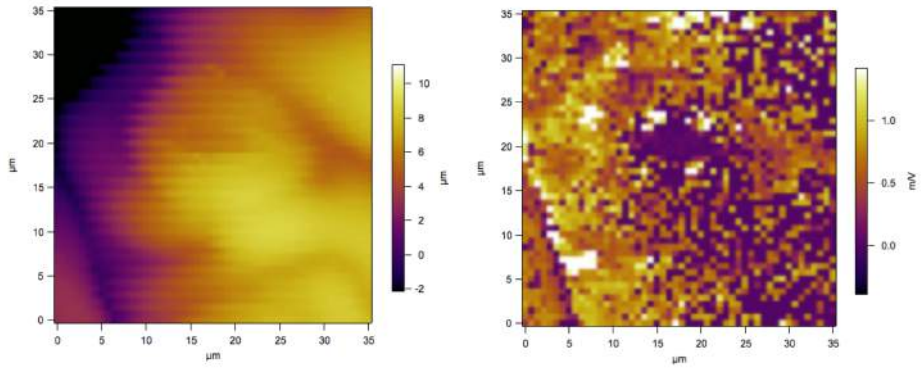

Figure B.23: Stomata 26 force map. A. Height map showing the topography. B. Stiffness map showing the spatial distribution of the mechanical properties.

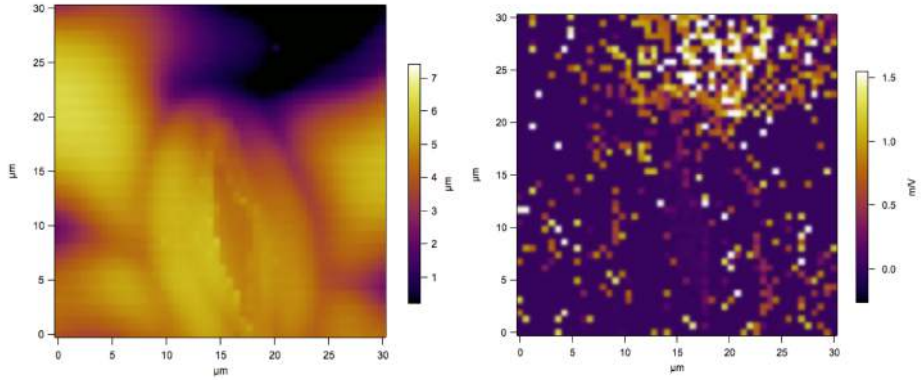

Figure B.24: Stomata 27 force map. A. Height map showing the topography. B. Stiffness map showing the spatial distribution of the mechanical properties.

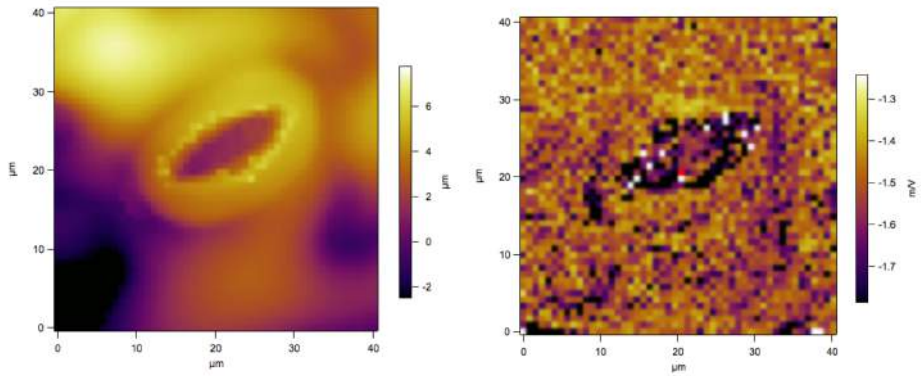

Figure B.25: Stomata 28 force map. A. Height map showing the topography. B. Stiffness map showing the spatial distribution of the mechanical properties.

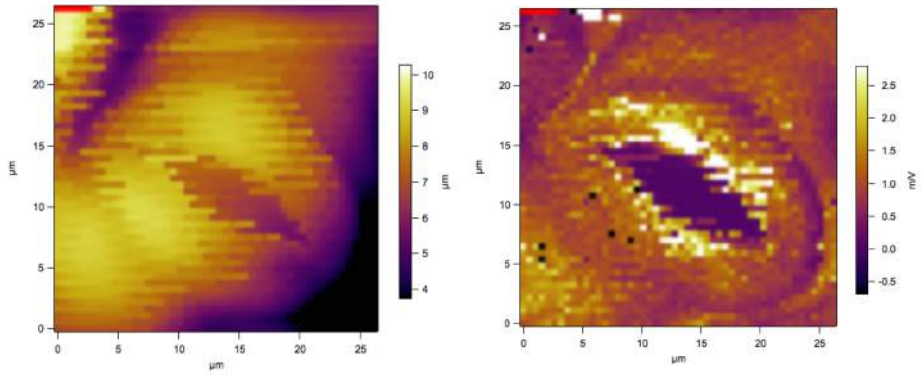

Figure B.26: Stomata 29 force map. A. Height map showing the topography. B. Stiffness map showing the spatial distribution of the mechanical properties.

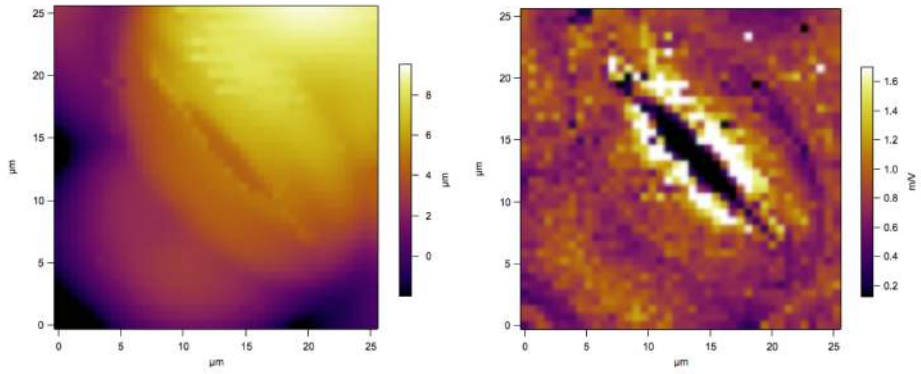

Figure B.27: Stomata 30 force map. A. Height map showing the topography. B. Stiffness map showing the spatial distribution of the mechanical properties.

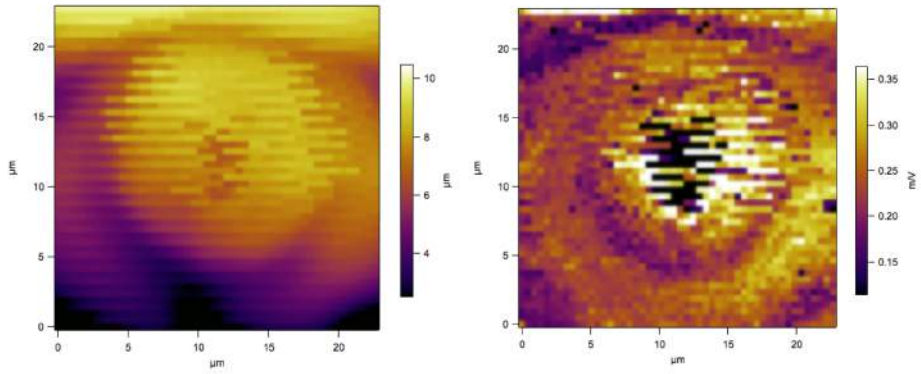

Figure B.28: Stomata 31 force map. A. Height map showing the topography. B. Stiffness map showing the spatial distribution of the mechanical properties.

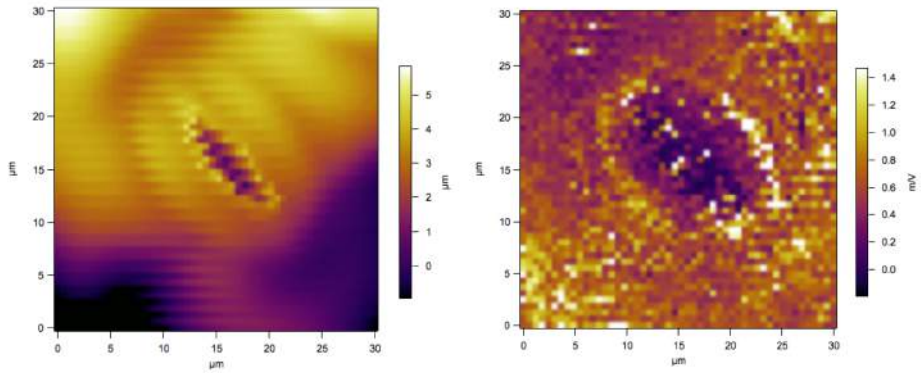

Figure B.29: Stomata 32 force map. A. Height map showing the topography. B. Stiffness map showing the spatial distribution of the mechanical properties.

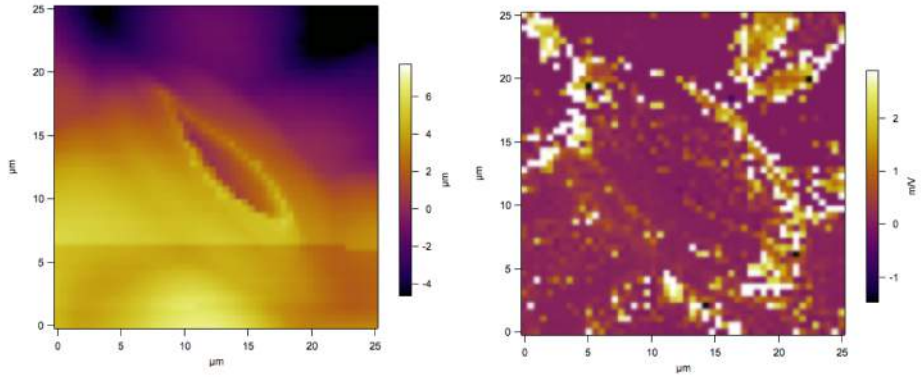

Figure B.30: Stomata 33 force map. A. Height map showing the topography. B. Stiffness map showing the spatial distribution of the mechanical properties.

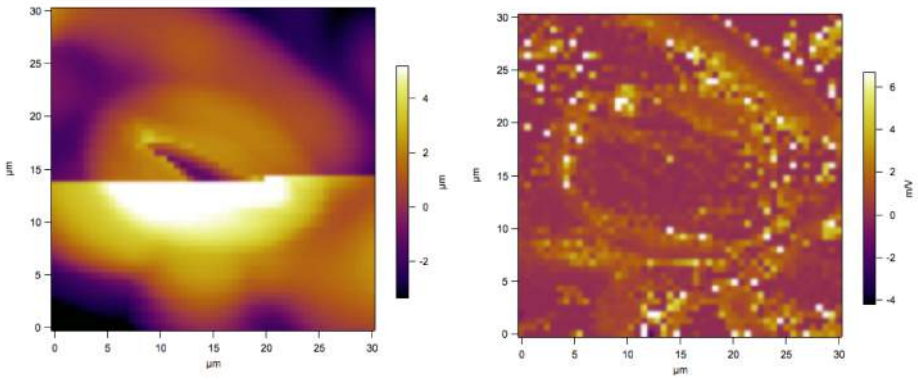

Figure B.31: Stomata 34 force map. A. Height map showing the topography. B. Stiffness map showing the spatial distribution of the mechanical properties.

Appendix C

Leaf Margin Model Code

```
function [AUXSolution, CUCSolution, LAX1Solution, LAX2Solution,...
    TOut, cellOut] = odesolver(p,sensi,centrepeak)
%This function takes a matrix of paramters and returns the time evolution
%of auxin, cuc2, LAX1 and LAX2

global  ndiff

rng(101)                %random number seed

Nint = 100;             %initial number of cells
ndiff = 4;              %number of differential equations

tstart = 0;             %timespace
tend = 16;

dl = 0.01;              %noise in initial auxin conditions
c_0 = zeros(1,Nint) + dl * rand(1,Nint);    %initial auxin

if centrepeak == 1      %optional persistant aixin peak
    c_0(50:51) = 7;
end

%c_0(Nint/2) = dl*rand(1);
CUC_0 = 5*ones(1,Nint);         %initial CUC
lax1_0 = zeros(1,Nint);         %initial lax1
lax2_0 = 0*ones(1,Nint);        %initial lax2

cnumber = (1:Nint);

y_0 = [c_0 CUC_0 lax1_0 lax2_0];            %initial conditions for ode

function [dydt] = odes(time,y)
%This function generates the ordianry differential equations describing the
%time evolution of the system


        n = length(y) / ndiff;
```

```
        c = y(1:n);

        if centrepeak == 1
            c(50:51) = 7;
        end

        CUC = y(n+1:2*n);
        LAX1 = y(2*n+1:3*n);
        LAX2 = y(3*n+1:4*n);

        % Construction of active transport matrix--------------------
        alpha = circshift(diag(circshift(PINL(c,CUC),1)),[1 0]);
        alpha(1,length(c)) = 0;
        alpha(length(c),1) = 0;
        beta = circshift(diag(circshift(PINR(c,CUC),-1)),[-1 0]);
        beta(1,length(c)) = 0;
        beta(length(c),1) = 0;
        gamma = zeros(length(c),length(c)) - diag(ones(length(c),1));
        PHI = alpha+beta+gamma;
        PHI(1,2) = 1;
        PHI(end,end-1 ) = 1;
        %-----------------------------------------------------------


        %separate odes for each
        dcdt = p(1) .* (p(2) - c) - p(3) .* c - (p(4) .* PHI*c)...
            +(p(5).* Dmatrix(c)*c)...
            -(p(10).* (Dmatrix(c)*LAX1).*c) - p(11).*LAX2.*c +p(16).*c;

        dcucdt = p(6) ./(1+p(7) .*(c)) - (p(8) + p(9).*c).*CUC;

        dlax1dt = p(12).*c.^2 ./(1 + p(13).*c.^2) -p(14).*LAX1;


        dlax2dt = vertcat(zeros(25,1),(p(15).*(ones(50,1) -...
            LAX2(26:75)).*c(26:75)), zeros(25,1)) ;

        %BCs matching cells 1,2,n-1,n
        dcdt(1) = dcdt(2) ;
        dcdt(end) = dcdt(end-1);

        if centrepeak ==1
            dcdt(50:51) = 0;
        end

        dydt = [dcdt' dcucdt' dlax1dt' dlax2dt']';      %master ode to be solved
    end

sol = ode45(@odes, [tstart, tend] , y_0);           %ode is solved

y = deval(sol,linspace(tstart,tend))';

%various outputs
AUXSolution = y(:,1:Nint)';
CUCSolution = y(:,Nint+1:2*Nint)';
LAX1Solution = y(:,2*Nint+1:3*Nint)';
LAX2Solution = y(:,3*Nint+1:4*Nint)';
```

```
TOut = repmat(linspace(tstart,tend),100,1);
cellOut = repmat((1:Nint)',1,Nint);


end

function [PIN] = PINR(aux,cuc) %vector of PIN values on RHS of cell

TH_CUC = 1;

PIN =  6.^circshift(aux,-1) ./ (6.^circshift(aux,-1) + 6.^circshift(aux,1));

PIN(cuc < TH_CUC) = 0.5;

PIN(1) = PIN(2);
PIN(length(aux)) = PIN(length(aux)-1);

end

function [PIN] = PINL(aux,cuc) %vector of PIN values on LHS of cell

PIN = 1 - PINR(aux,cuc);

end

function [matrix] = Dmatrix(in) %diffusion matrix

n = length(in);

matrix = -2*eye(n) + circshift(eye(n),1) + circshift(eye(n),-1);

matrix(1,1) =  -1;
matrix(n,n) =  -1;

matrix(1,n) = 0;
matrix(n,1) = 0;
end
```

Bibliography

[1] J. L. Hall, T. J. Flowers, and R. M. Roberts. *Plant cell structure and metabolism.* ELBS low-priced editions. Longman, 1982.

[2] D. J. Cosgrove. Growth of the plant cell wall. *Nat Rev Mol Cell Biol*, 6(11):850–61, Nov 2005.

[3] N. A. Campbell and J. B. Reece. *Biology.* Alternative eText Formats Series. Pearson Benjamin Cummings, 2008.

[4] G. Griffiths. Cell evolution and the problem of membrane topology. *Nat Rev Mol Cell Biol*, 8(12):1018–1024, 12 2007.

[5] Simon R Turner and Chris R Somerville. Collapsed xylem phenotype of arabidopsis identifies mutants deficient in cellulose deposition in the secondary cell wall. *The Plant Cell Online*, 9(5):689–701, 1997.

[6] C. Somerville, S. Bauer, G. Brininstool, M. Facette, T. Hamann, J. Milne, E. Osborne, A. Paredez, S. Persson, T. Raab, S. Vorwerk, and H. Youngs. Toward a systems approach to understanding plant cell walls. *Science*, 306(5705):2206–11, Dec 2004.

[7] V. Mirabet, P. Das, A. Boudaoud, and O. Hamant. The role of mechanical forces in plant morphogenesis. *Annu Rev Plant Biol*, 62:365–85, Jun 2011.

[8] Lacey Samuels, Ljerka Kunst, and Reinhard Jetter. Sealing plant surfaces: Cuticular wax formation by epidermal cells. *Annual Review of Plant Biology*, 59(1):683–707, 2008. PMID: 18251711.

[9] A. Boudaoud. Growth of walled cells: From shells to vesicles. *Phys. Rev. Lett.*, 91:018104, Jul 2003.

[10] O. Hamant and J. Traas. The mechanics behind plant development. *New Phytol*, 185(2):369–85, Jan 2010.

[11] G. G. Polikarpov. Sunflower's blooming floscule is a compass. *Nature*, 272(5649):122–122, 03 1978.

[12] J. A. Lockhart. An analysis of irreversible plant cell elongation. *Journal of Theoretical Biology*, 8(2):264 – 275, 1965.

[13] Daniel J Cosgrove. Cell wall yield properties of growing tissue : Evaluation by in vivo stress relaxation. *Plant Physiology*, 78(2):347–356, 06 1985.

[14] Y. Zhao. Auxin biosynthesis and its role in plant development. *Annu Rev Plant Biol*, 61:49–64, 2010.

[15] R. E. Williamson. Alignment of cortical microtubules by anisotropic wall stresses. *Functional Plant Biology*, 17(6):601–613, 01 1990.

[16] M. G. Heisler, O. Hamant, P. Krupinski, M. Uyttewaal, C. Ohno, H. Jönsson, J. Traas, and E. M. Meyerowitz. Alignment between pin1 polarity and microtubule orientation in the shoot apical meristem reveals a tight coupling between morphogenesis and auxin transport. *PLoS Biol*, 8(10):e1000516, 10 2010.

[17] F. Corson, O. Hamant, S. Bohn, J. Traas, A. Boudaoud, and Y. Couder. Turning a plant tissue into a living cell froth through isotropic growth. *Proceedings of the National Academy of Sciences*, 106(21):8453–8458, 2009.

[18] A. J. Fleming, S. McQueen-Mason, T. Mandel, and C. Kuhlemeier. Induction of leaf primordia by the cell wall protein expansin. *Science*, 276(5317):1415–1418, 1997.

[19] Jeanette A Nadeau and Fred D Sack. Stomatal development in arabidopsis. *The Arabidopsis Book / American Society of Plant Biologists*, 1:e0066, 2002.

[20] C.M. Willmer and M. Fricker. *Stomata*. Topics in plant functional biology. Chapman and Hall, 1996.

[21] A. Geitmann. Experimental approaches used to quantify physical parameters at cellular and subcellular levels. *American Journal of Botany*, 93(10):1380–1390, 2006.

[22] A. Geitmann, W. McConnaughey, I. Lang-Pauluzzi, V. E. Franklin-Tong, and A. M. C. Emons. Cytomechanical properties of papaver pollen tubes are altered after self-incompatibility challenge. *Biophysical Journal*, 86(5):3314 – 3323, 2004.

[23] K. L. Johnson. *Contact Mechanics*. Cambridge University Press, 1987.

[24] Jenny Blewett, Kathleen Burrows, and Colin Thomas. A micromanipulation method to measure the mechanical properties of single tomato suspension cells. 22(23):1877–1883, 2000.

[25] J.D. Ferry. *Viscoelastic Properties of Polymers*. Wiley, 3rd edition, 1980.

[26] Steen Laugesen Hansen, Peter Martin Ray, Anders Ola Karlsson, Bodil Jørgensen, Bernhard Borkhardt, Bent Larsen Petersen, and Peter Ulvskov. Mechanical properties of plant cell walls probed by relaxation spectra. *Plant Physiology*, 155(1):246–258, 2011.

[27] Yves Verhertbruggen, Susan E. Marcus, Jianshe Chen, and J. Paul Knox. Cell wall pectic arabinans influence the mechanical properties of arabidopsis thaliana inflorescence stems and their response to mechanical stress. *Plant and Cell Physiology*, 54(8):1278–1288, 2013.

[28] Joost J. Vlassak and W.D. Nix. Measuring the elastic properties of anisotropic materials by means of indentation experiments. *Journal of the Mechanics and Physics of Solids*, 42(8):1223 – 1245, 1994.

[29] Elisabeth Chanliaud, KathleenM. Burrows, George Jeronimidis, and MichaelJ. Gidley. Mechanical properties of primary plant cell wall analogues. *Planta*, 215(6):989–996, 2002.

[30] R. J. Howard and B. Valent. Breaking and entering: Host penetration by the fungal rice blast pathogen magnaporthe grisea. *Annual Review of Microbiology*, 50(1):491–512, 1996.

[31] P. M. Lintilhac, C. Wei, J. J. Tanguay, and J. O. Outwater. Ball tonometry: A rapid, nondestructive method for measuring cell turgor pressure in thin-walled plant cells. *Journal of Plant Growth Regulation*, 19:90–97, 2000. 10.1007/s003440000009.

[32] A. Deri Tomos and Roger A. Leigh. The pressure probe: A versatile tool in plant cell physiology. *Annual Review of Plant Physiology and Plant Molecular Biology*, 50(1):447–472, 1999. PMID: 15012216.

[33] P. B. Green. Growth physics in nitella: A method for continuous in vivo analysis of extensibility based on a micro-manometer technique for turgor pressure. *Plant Physiology*, 43(8):pp. 1169–1184, 1968.

[34] Dieter Hüsken, Ernst Steudle, and Ulrich Zimmermann. Pressure probe technique for measuring water relations of cells in higher plants. *Plant Physiology*, 61(2):158–163, 1978.

[35] Timothy E Proseus, Joseph KE Ortega, and John S Boyer. Separating growth from elastic deformation during cell enlargement. *Plant Physiology*, 119(2):775–784, 02 1999.

[36] G. Binnig and C. F. Quate. Atomic force microscope. *Phys Rev Lett*, 56(9):930–933, March 1986.

[37] D. Rugar and P. Hansma. Atomic force microscopy. *Physics Today*, pages 23–30, October 1990.

[38] O. M. El-Rifai and K. Youcef-Toumi. On factors affecting the performance of atomic force microscopes in contact-mode. In *1999 IEEE/ASME International Conference on Advanced Intelligent Mechatronics*, 1999.

[39] R. Garca and R. Pérez. Dynamic atomic force microscopy methods. *Surface Science Reports*, 47:197–301, 2002.

[40] S.N. Magonov, V. Elings, and M.-H. Whangbo. Phase imaging and stiffness in tapping-mode atomic force microscopy. *Surface Science*, 375(2â“3):L385 – L391, 1997.

[41] H. J. Butt. Measuring electrostatic, van der waals, and hydration forces in electrolyte solutions with an atomic force microscope. *Biophysical Journal*, 60(6):1438 – 1444, 1991.

[42] J. L. Hutter and J. Bechhoefer. Calibration of atomic-force microscope tips. *Review of Scientific Instruments*, 64(7):1868–1873, 1993.

[43] J. J. Waterson. On the physics of media that are composed of free and elastic molecules in a state of motion. *Royal Society Proceedings*, 5(0):604, 1846.

[44] C.V. Heer. *Statistical mechanics, kinetic theory, and stochastic processes*. Academic Press, 1972.

[45] H-J. Butt, B. Cappella, and M. Kappl. Force measurements with the atomic force microscope: Technique, interpretation and applications. *Surface Science Reports*, 59(16):1 – 152, 2005.

[46] H. R. Hertz. *Ueber die Beruehrung elastischer Koerper (On Contact Between Elastic Bodies)*, volume 1. Leipzig, Germany, 1895.

[47] R. E. Mahaffy, C. K. Shih, F. C. MacKintosh, and J. Käs. Scanning probe-based frequency-dependent microrheology of polymer gels and biological cells. *Phys. Rev. Lett.*, 85:880–883, Jul 2000.

[48] B. Drake, C. B. Prater, A. L. Weisenhorn, S. A. Gould, T. R. Albrecht, C. F. Quate, D. S. Cannell, H. G. Hansma, and P. K. Hansma. Imaging crystals, polymers, and processes in water with the atomic force microscope. *Science*, 243(4898):1586–1589, 1989.

[49] Y. L. Lyubchenko, L. S. Shlyakhtenko, and A. A. Gall. Atomic force microscopy imaging and probing of dna, proteins, and protein-dna complexes: Silatrane surface chemistry. *DNA-Protein Interactions*, 543, December 2008.

[50] W. Häberle, J. K. H. Hörber, F. Ohnesorge, D. P. E. Smith, and G. Binnig. In situ investigations of single living cells infected by viruses. *Ultramicroscopy*, 42–44, Part 2(0):1161–1167, 7 1992.

[51] M. Radmacher, R. W. Tillamnn, M. Fritz, and H. E. Gaub. From molecules to cells: imaging soft samples with the atomic force microscope. *Science*, 257(5078):1900–1905, 1992.

[52] A.R. Kirby, A.P. Gunning, K.W. Waldron, V.J. Morris, and A. Ng. Visualization of plant cell walls by atomic force microscopy. *Biophysical Journal*, 70(3):1138 – 1143, 1996.

[53] M. C. McCann, B. Wells, and K. Roberts. Direct visualization of cross-links in the primary plant cell wall. *Journal of Cell Science*, 96(2):323–334, 1990.

[54] P. Milani, M. Gholamirad, J. Traas, A. Arnéodo, A. Boudaoud, F. Argoul, and O. Hamant. In vivo analysis of local wall stiffness at the shoot apical meristem in arabidopsis using atomic force microscopy. *Plant J*, 67(6):1116–23, Sep 2011.

[55] D. Kwiatkowska. Surface growth at the reproductive shoot apex of arabidopsis thaliana pinformed 1 and wild type. *Journal of Experimental Botany*, 55(399):1021–1032, 2004.

[56] S. A. Braybrook and A. Peaucelle. Mechano-chemical aspects of organ formation in arabidopsis thaliana: The relationship between auxin and pectin. *PLoS ONE*, 8(3):e57813, 03 2013.

[57] A. Peaucelle, S. Braybrook, L. Le Guillou, E. Bron, C. Kuhlemeier, and H. Höfte. Pectin-induced changes in cell wall mechanics underlie organ initiation in arabidopsis. *Curr Biol*, 21(20):1720–6, Oct 2011.

[58] H. Jönsson, J. Gruel, P. Krupinski, and C. Troein. On evaluating models in computational morphodynamics. *Curr Opin Plant Biol*, 15(1):103–10, Feb 2012.

[59] V. Chickarmane, A. H. K. Roeder, P. T. Tarr, A. Cunha, C. Tobin, and E. M. Meyerowitz. Computational morphodynamics: A modeling framework to understand plant growth. *Annual Review of Plant Biology*, 61(1):65–87, 2010.

[60] O. Hamant, J. Traas, and A. Boudaoud. Regulation of shape and patterning in plant development. *Curr Opin Genet Dev*, 20(4):454–9, Aug 2010.

[61] D. Kwiatkowska. Structural integration at the shoot apical meristem: Models, measurements, and experiments. *American Journal of Botany*, 91(9):pp. 1277–1293, 2004.

[62] R. M.H. Merks, M. Guravage, D. Inzé, and G. T.S. Beemster. Virtualleaf: An open-source framework for cell-based modeling of plant tissue growth and development. *Plant Physiology*, 155(2):656–666, 2011.

[63] P. Prusinkiewicz and A. Lindenmayer. *The algorithmic beauty of plants*. Virtual laboratory. Springer, 1996.

[64] P. Prusinkiewicz, Y. Erasmus, B. Lane, L. D. Harder, and E. Coen. Evolution and development of inflorescence architectures. *Science*, 316(5830):1452–1456, 2007.

[65] H. Meinhardt. *Models of Biological Pattern Formation: From Elementary Steps to the Organization of Embryonic Axes*, volume 81 of *Current Topics in Developmental Biology*. Academic Press, 2008.

[66] A. M. Turing. The chemical basis of morphogenesis. *Philosophical Transactions of the Royal Society of London. Series B, Biological Sciences*, 237(641):33–72, August 1952.

[67] N. S. Savage, T. Walker, Y. Wieckowski, J. Schiefelbein, L. Dolan, and N. A. M. Monk. A mutual support mechanism through intercellular movement of caprice and glabra3 can pattern the arabidopsis root epidermis. *PLoS Biol*, 6(9):e235, 09 2008.

[68] V. Grieneisen and B. Scheres. Back to the future: evolution of computational models in plant morphogenesis. *Current Opinion in Plant Biology*, 12(5):606 – 614, 2009.

[69] S. A. Braybrook, H. Hofte, and A. Peaucelle. Probing the mechanical contributions of the pectin matrix: Insights for cell growth. *Plant Signaling & Behavior*, 7(8):1037–1041, 08 2012.

[70] A.-L. Routier-Kierzkowska, A. Weber, P. Kochova, D. Felekis, B. J. Nelson, C. Kuhlemeier, and R. S. S Smith. Cellular force microscopy for in vivo measurements of plant tissue mechanics. *Plant physiology*, 158(4):1514–1522, 2012.

[71] E. Gendreau, J. Traas, T. Desnos, O. Grandjean, M. Caboche, and H. Hofte. Cellular basis of hypocotyl growth in arabidopsis thaliana. *Plant Physiology*, 114(1):295–305, 1997.

[72] D. J. Cosgrove. Wall extensibility: its nature, measurement and relationship to plant cell growth. *New Phytologist*, 124(1):1–23, 1993.

[73] D. J. Cosgrove. Loosening of plant cell walls by expansins. *Nature*, 407(6802):321–326, 09 2000.

[74] L. Borghi. Inducible gene expression systems for plants. In Lars Hennig and Claudia Köhler, editors, *Plant Developmental Biology*, volume 655 of *Methods in Molecular Biology*, pages 65–75. Humana Press, 2010.

[75] A. Kuwabara, A. Backhaus, R. Malinowski, M. Bauch, L. Hunt, T. Nagata, N. Monk, G. Sanguinetti, and A. J. Fleming. A shift toward smaller cell size via manipulation of cell cycle gene expression acts to smoothen arabidopsis leaf shape. *Plant Physiology*, 156(4):2196–2206, 2011.

[76] T. Murashige and F. Skoog. A revised medium for rapid growth and bio assays with tobacco tissue cultures. *Physiologia Plantarum*, 15(3):473–497, 1962.

[77] J.G. Swadener, E.P. George, and G.M. Pharr. The correlation of the indentation size effect measured with indenters of various shapes. *Journal of the Mechanics and Physics of Solids*, 50(4):681 – 694, 2002.

[78] Matthew A Jenks, Sanford D Eigenbrode, and Bertrand Lemieux. Cuticular waxes of arabidopsis. *The Arabidopsis Book / American Society of Plant Biologists*, 1:e0016, 2002.

[79] L. Wang, D. Hukin, J. Pritchard, and C. Thomas. Comparison of plant cell turgor pressure measurement by pressure probe and micromanipulation. *Biotechnology Letters*, 28(15):1147–1150, 2006.

[80] J.-F. Bolduc, L. Lewis, C.-É. Aubin, and A. Geitmann. Finite-element analysis of geometrical factors in micro-indentation of pollen tubes. *Biomechanics and Modeling in Mechanobiology*, 5(4):227–236, 2006.

[81] P. J. Franks and G. D.r Farquhar. The mechanical diversity of stomata and its significance in gas-exchange control. *Plant Physiology*, 143(1):78–87, 2007.

[82] J. Zhang, U. Schurr, and W. J. Davies. Control of stomatal behaviour by abscisic acid which apparently originates in the roots. *Journal of Experimental Botany*, 38(7):1174–1181, 1987.

[83] A. Daszkowska-Golec and I. Szarejko. Open or close the gate – stomata action under the control of phytohormones in drought stress conditions. *Frontiers in Plant Science*, 4(138), 2013.

[84] J. R. Cooke, J.G. DeBaerdemaeker, R.H. Rand, and H.A. Mang. A finite element shell analysis of guard cell deformations. *Transactions of the ASAE*, 19(6):1107–1121, 1976.

[85] T. Meckel, L. Gall, S. Semrau, U. Homann, and G. Thiel. Guard cells elongate: Relationship of volume and surface area during stomatal movement. *Biophysical Journal*, 92(3):1072 – 1080, 2007.

[86] J. M. Widholm. The use of fluorescein diacetate and phenosafranine for determining viability of cultured plant cells. *Biotechnic and Histochemistry*, 47(4):189–194, 1972.

[87] L. J. Pillitteri and K. U. Torii. Mechanisms of stomatal development. *Annu Rev Plant Biol*, 63:591–614, 2012.

[88] P. J. P. Espitia, W.-X. Du, R. d. J. Avena-Bustillos, N. d. F. F. Soares, and T. H. McHugh. Edible films from pectin: Physical-mechanical and antimicrobial properties - a review. *Food Hydrocolloids*, 35(0):287 – 296, 2014.

[89] G. Chinga-Carrasco. Cellulose fibres, nanofibrils and microfibrils: the morphological sequence of mfc components from a plant physiology and fibre technology point of view. *Nanoscale research letters*, 6(1):1–7, 2011.

[90] I. Zelitch. Biochemical control of stomatal opening in leaves. *Proceedings of the National Academy of Sciences of the United States of America*, 47(9):1423, 1961.

[91] Y. Wang, K. Noguchi, N. Ono, S. Inoue, I. Terashima, and T. Kinoshita. Overexpression of plasma membrane h+-atpase in guard cells promotes light-induced stomatal opening and enhances plant growth. *Proceedings of the National Academy of Sciences*, 111(1):533–538, 2014.

[92] R. Matzke, K. Jacobson, and M. Radmacher. Direct, high-resolution measurement of furrow stiffening during division of adherent cells. *Nature cell biology*, 3(6):607–610, 2001.

[93] Peter Schopfer. Biomechanics of plant growth. *American journal of botany*, 93(10):1415–1425, 2006.

[94] E. Kawamura, G. Horiguchi, and H. Tsukaya. Mechanisms of leaf tooth formation in arabidopsis. *The Plant Journal*, 62(3):429–441, 2010.

[95] K. Nikovics, T. Blein, A. Peaucelle, T. Ishida, H. Morin, M. Aida, and P. Laufs. The balance between the mir164a and cuc2 genes controls leaf margin serration in arabidopsis. *The Plant Cell Online*, 18(11):2929–2945, 2006.

[96] J. Kleine-Vehn, P. Dhonukshe, R. Swarup, M. Bennett, and J. Friml. Subcellular trafficking of the arabidopsis auxin influx carrier aux1 uses a novel pathway distinct from pin1. *The Plant Cell Online*, 18(11):3171–3181, 2006.

[97] R. S. Smith, S. Guyomarc'h, T. Mandel, D. Reinhardt, C. Kuhlemeier, and P. Prusinkiewicz. A plausible model of phyllotaxis. *Proceedings of the National Academy of Sciences of the United States of America*, 103(5):1301–1306, 2006.

[98] G. D Bilsborough, A. Runions, M. Barkoulas, H. W. Jenkins, A. Hasson, C. Galinha, P. Laufs, A. Hay, P. Prusinkiewicz, and M. Tsiantis. Model for the regulation of arabidopsis thaliana leaf margin development. *Proc Natl Acad Sci USA*, 108(8):3424–9, Feb 2011.

[99] A. Kasprewska, R. Carter, M. Bauch, M. Bennett, R. Swarup, N. Monk, J. K. Hobbs, and A. J. Fleming. Auxin influx importers modulate the timing of morphogenesis along the leaf margin (unpublished). 2014.

[100] R. A. Jefferson, T. A. Kavanagh, and M. W. Bevan. Gus fusions: beta-glucuronidase as a sensitive and versatile gene fusion marker in higher plants. *EMBO J.*, 6(13):3901–7, Dec 1987.

[101] K. Bainbridge, S. Guyomarc'h, E. Bayer, R. Swarup, M. Bennett, T. Mandel, and C. Kuhlemeier. Auxin influx carriers stabilize phyllotactic patterning. *Genes and Development*, 22(6):810–823, 2008.

[102] T. Ulmasov, J. Murfett, G. Hagen, and T. J. Guilfoyle. Aux/iaa proteins repress expression of reporter genes containing natural and highly active synthetic auxin response elements. *The Plant Cell Online*, 9(11):1963–71, 1997.

[103] J. Mattsson, W. Ckurshumova, and T. Berleth. Auxin signaling in arabidopsis leaf vascular development. *Plant Physiology*, 131(3):1327–1339, 2003.

[104] Gloria K Muday and Alison DeLong. Polar auxin transport: controlling where and how much. *Trends in Plant Science*, 6(11):535 – 542, 2001.

[105] E. M. Kramer. Computer models of auxin transport: a review and commentary. *Journal of Experimental Botany*, 59(1):45–53, 2008.

[106] V. Grieneisen, J. Xu, A. F. M. Marée, P. Hogeweg, and B. Scheres. Auxin transport is sufficient to generate a maximum and gradient guiding root growth. *Nature*, 449(7165):1008–1013, 2007.

[107] R. Swarup, E. M. Kramer, P. Perry, K. Knox, H. M. O. Leyser, J. Haseloff, G. T. S. Beemster, R. Bhalerao, and M. J. Bennett. Root gravitropism requires lateral root cap and epidermal cells for transport and response to a mobile auxin signal. *Nat Cell Biol*, 7(11):1057–1065, 11 2005.

[108] J. R. Dormand and P. J. Prince. A family of embedded runge-kutta formulae. *Journal of Computational and Applied Mathematics*, 6(1):19 – 26, 1980.

[109] A. J. Trewavas and R. E. Cleland. Is plant development regulated by changes in the concentration of growth substances or by changes in the sensitivity to growth substances? *Trends in Biochemical Sciences*, 8(10):354–357, 1983.

[110] D. M. Hamby. A review of techniques for parameter sensitivity analysis of environmental models. *Environmental Monitoring and Assessment*, 32(2):135–154, 1994.

[111] Su-Hwan Kwak and John Schiefelbein. A feedback mechanism controlling {SCRAMBLED} receptor accumulation and cell-type pattern in arabidopsis. *Current Biology*, 18(24):1949 – 1954, 2008.

[112] Markus Grebe. The patterning of epidermal hairs in arabidopsis - updated. *Current Opinion in Plant Biology*, 15(1):31 – 37, 2012. Growth and development.

[113] H. M. O. Leyser, F. B. Pickett, S. Dharmasiri, and M. Estelle. Mutations in the axr3 gene of arabidopsis result in altered auxin response including ectopic expression from the saur-ac1 promoter. *The Plant Journal*, 10(3):403–413, 1996.

[114] B. Péret, K. Swarup, A. Ferguson, M. Seth, Y. Yang, S. Dhondt, N. James, I. Casimiro, P. Perry, A. Syed, H. Yang, J. Reemmer, E. Venison, C. Howells, M. A. Perez-Amador, J. Yun, J. Alonso, G. T. S. Beemster, L. Laplaze, A. Murphy, M. J. Bennett, E. Nielsen, and R. Swarup. Aux/lax genes encode a family of auxin influx transporters that perform distinct functions during arabidopsis development. *The Plant Cell Online*, 24(7):2874–2885, 07 2012.

[115] Y. Ugartechea-Chirino, R. Swarup, K. Swarup, B. Péret, M. Whitworth, M. Bennett, and S. Bougourd. The aux1 lax family of auxin influx carriers is required for the establishment of embryonic root cell organization in arabidopsis thaliana. *Annals of Botany*, 105(2):277–289, 02 2010.

[116] P. Milani, V. Mirabet, C. Cellier, F. Rozier, O. Hamant, P. Das, and A. Boudaoud. Matching patterns of gene expression to mechanical stiffness at cell resolution through quantitative tandem epifluorescence and nanoindentation. *Plant Physiology*, 165(4):1399–1408, 2014.